technische universität
dortmund

Dissertation zur Erlangung des Doktorgrades der Naturwissenschaften der Fakultät Physik der Technischen Universität Dortmund

The electronic structure of iron-bearing compounds in the deep Earth

Christian Albers
geboren in Warstein

2023

Erstgutachter: Prof. Dr. Metin Tolan
Zweitgutachter: Prof. Dr. Max Wilke

Contents

Kurzfassung

Eisen ist das am häufigsten vorkommende Übergangsmetall in der tiefen Erde. Aufgrund seiner komplexen elektronischen Struktur kann es in zwei verschiedenen Oxidationszuständen (Fe^{2+} und Fe^{3+}) auftreten und außerdem seinen Spinzustand ändern. Daher spielt es eine wichtige Rolle für die physikalischen und chemischen Eigenschaften der tiefen Erdschichten. Im Rahmen dieser Arbeit wurden drei geologisch relevante Probensysteme auf ihre elektronische Struktur bei Druck- und Temperaturbedingungen untersucht, die für den unteren Erdmantel relevanten sind. Dazu wurden die (nichtresonante) $K\beta_{1,3}$- und Valenz-zu-Kern-Röntgenemissionsspektroskopie sowie die resonante 1s2p-Röntgenemissionsspektroskopie eingesetzt. Zunächst führte die Untersuchung von lasergeheiztem $FeCO_3$ bei etwa 80 GPa zur Synthese von $Fe_4C_3O_{12}$ und $Fe_4C_4O_{13}$. Es konnte nachgewiesen werden, dass sich das Eisen in diesen beiden Phasen in einem Hoch-Spin-Zustand befindet. Außerdem konnte das Auftreten von Raman-Banden mit niedriger Wellenzahl in einem Wellenzahlbereich zwischen $100\,cm^{-1}$ und $350\,cm^{-1}$ $Fe_4C_4O_{13}$ zugeordnet werden. Zweitens belegt die Studie an kalt komprimiertem Fe_2O_3 einen zweistufigen Spinübergang von α- über ζ- zu Θ-Fe_2O_3. Darüber hinaus unterstützen resonante 1s2p-Röntgenemissionsspektroskopiemessungen eine mögliche Delokalisierung der elektronischen Zustände in den Hochdruckphasen. Drittens zeigt der Einfluss des Drucks auf die elektronische Struktur von FeO einen signifikanten Einfluss auf die Linienform der $K\beta_{1,3}$-Emission, obwohl kein Spinübergang stattfindet. Die Änderungen der Linienform können mit einer Verzerrung der Kristallstruktur in Zusammenhang gesetzt werden. Dies wird in Zukunft einen wesentlichen Einfluss auf die Interpretation von $K\beta_{1,3}$-Spektren haben. Zusätzlich dazu wurde der Aufbau für spektroskopische Messungen erheblich verbessert, indem die Datenerfassungszeiten für die $K\beta_{1,3}$-Röntgenemissionsspektroskopie innerhalb von Sekunden, für hochwertige Valenz-Kern-Emissionsspektroskopie innerhalb von Minuten und für resonante Röntgenemissionsspektroskopie-Messungen in weniger als einer Stunde verkürzt wurden, was einzigartige spektroskopische Möglichkeiten unter extremen Bedingungen bietet.

Abstract

Iron is the most abundant transition metal in the deep Earth. Due to its complex electronic structure, it can appear in two different oxidation states (Fe^{2+} and Fe^{3+}) and can also undergo a spin transition. Hence, it plays an important role in the physical and chemical properties of the deep Earth assemblage. Within this thesis, three geologically relevant sample systems were investigated regarding their electronic structure at pressure and temperature conditions that are relevant to the Earth's lower mantle. Therefore, (non-resonant) $K\beta_{1,3}$ and valence-to-core X-ray emission spectroscopy as well as resonant 1s2p X-ray emission spectroscopy were utilized. First, the study of laser-heated $FeCO_3$ at about 80 GPa results in the synthesis of $Fe_4C_3O_{12}$ and $Fe_4C_4O_{13}$. The iron in both of these phases was verified to be in high-spin state. Furthermore, the emergence of low-wavenumber Raman bands in a wavenumber range between 100 cm^{-1} and 350 cm^{-1} could be assigned to $Fe_4C_4O_{13}$. Second, the study on cold compressed Fe_2O_3 verifies a two-step spin transition from α- via ζ- to Θ-Fe_2O_3. Moreover, resonant X-ray emission spectroscopy measurements support a possible delocalization of the electronic states in the high pressure phases. Third, the influence of pressure on the electronic structure of FeO shows significant influence on the line shape of the $K\beta_{1,3}$ emission, although no spin transition occurred. The line-shape changes could be connected to a distortion of the crystal structure. This will have a substantial influence on the interpretation of $K\beta_{1,3}$-spectra in the future. Additionally, the setup for spectroscopic measurements was significantly improved with reduced data acquisition times of $K\beta_{1,3}$ X-ray emission spectroscopy within seconds, high-quality valence-to-core emission spectroscopy within minutes and resonant X-ray emission spectroscopy measurements in less than one hour, offering unique spectroscopic opportunities at extreme conditions.

1 Introduction

The Earth has a radius of $\sim 6370\,\mathrm{km}$ and its interior is divided into three main parts, the core (thickness $\sim 3480\,\mathrm{km}$), the mantle (thickness $\sim 2870\,\mathrm{km}$) and the crust (thickness $\sim 20\,\mathrm{km}$).[1] These main parts can be further divided into subparts such as the solid inner and liquid outer core.[2] The largest subpart in terms of volume is the lower mantle that starts at 670 km below the Earth's surface and reaches up to 2890 km in depth, with thermodynamic conditions of 24 GPa - 136 GPa[1] in pressure and 2000 K - 4400 K[3–8] in temperature, depending on the depth below the surface. Its bulk consists mainly of silicate perovskite (SP) and oxides (mainly ferropericlase (FP)),[9] but in the vicinity of subducting slabs also carbonates are present.[10] Within these phases, iron plays a key role, as it is the most abundant transition metal in the lower mantle. Due to its complex electronic structure, it can be present in its ferrous (Fe^{2+}) and ferric (Fe^{3+}) oxidation state, allowing for a transition between numerous different phases, which may buffer the element partitioning for different oxidizing or reducing conditions. In context of the lower mantle, especially ferric iron is interesting as with increasing pressure the $Fe^{3+}/\sum Fe$ is rising.[9] Furthermore, iron, in Fe^{2+} and Fe^{3+} state, can undergo a spin transition, which changes its physical and chemical properties, influencing for example the phase's sound velocity, density or compressibility. Additionally, the element partitioning is depending on the iron's spin state, as phases with iron in the low-spin (LS) state have the tendency to incorporate more iron into the phase on loss of, e.g., magnesium in case of Fe^{2+} or aluminum in case of Fe^{3+}.[11–16]

Despite extensive studies, the complex chemistry of the deep Earth is still not fully understood and further theoretical and experimental studies are necessary. As direct measurements are not feasible due to the inaccessibility of these regions, the conditions in the lower mantle have to be reproduced in a laboratory environment. Therefore, diamond anvil cells (DACs) are commonly used and can generate pressures starting from below one gigapascal (GPa) up into the terapascal (TPa) range.[17] The combination of a DAC with a laser-heating system or with X-ray heating using short X-ray free electron laser (XFEL) pulses then allows to probe materials in the full thermodynamic range of the lower mantle.[18,19]

A variety of possible techniques is available to analyze structural and electronic properties of the samples inside a DAC. However, the full range of techniques is limited by the complex sample environment to optical and (hard) X-ray measurements. Methods such as electron energy loss spectroscopy (EELS) are not feasible, as the electrons are not able to penetrate the diamonds of the DAC. The same applies for soft X-rays due to the high absorbance of diamond of more than 99% for photons with an energy below 4500 eV and a diamond penetration length of 500 µm.[20] Nevertheless, there are still numerous methods available within the optical and hard X-ray regime to determine the properties of the sample.
Optical Raman and infrared spectroscopy provide structural information and are comparably easy to perform with the downside of a challenging data analysis. Both methods provide complementary information on vibrational modes of the sample that depend on a variety of structural properties such as bonding distances, angles and type of elements.

Contrary, X-ray diffraction (XRD) is easy to analyze (compared to the previously mentioned methods), but the experimental requirements are extensively more complex, especially when performed on a sample inside a DAC environment. It provides information on atomic distances and bond angles of the sample and can derive its crystalline structure. However, XRD is not limited to crystalline samples but can also be applied to solid amorphous samples or liquids. Despite its experimental challenges, it is a commonly used standard technique in the DAC community (see for example[19,21–23]). For information on the electronic structure, several spectroscopic approaches can be taken, depending on the type of information required and the type of element studied. These approaches are all sensitive to only one specific type of element within the sample. X-ray absorption spectroscopy (XAS) can be divided into two different methods. Extended X-ray absorption fine structure (EXAFS) provides information on the coordination around the absorbing atom and is thus, again a method that determines the structural properties of a sample, whereas X-ray absorption near-edge structure (XANES) spectroscopy directly probes empty electronic states of the sample in the vicinity of the elements absorption edge, providing information on the atoms coordination, symmetry and oxidation state.[24–27] Complementary, X-ray emission spectroscopy (XES) probes occupied states of a sample. In particular, $K\beta_{1,3}$ XES provides information on the spin state and XES in the valence-to-core (VTC) region gives information on the coordination chemistry around the absorbing atom.[28–30] If the incident energy in an XES experiment is varied around the elements absorption edge, it can be seen as a combined measurement of XAS and XES and is called resonant X-ray emission spectroscopy (RXES). This method probes both, occupied and unoccupied states in a sample. Furthermore, this is a technique that provides information similar to L- and M- absorption edges of heavy elements, e.g., transition metals, that are otherwise inaccessible in a DAC environment due to the low energy of those transitions.[31] As an example: In case of 1s2p RXES on iron, the incident energy is varied around the K-edge of the absorbing iron atom and the signal of its $K\alpha$ emission is detected. This provides on the one hand information about the atoms K-edge, if analyzed with respect to the incident energy, and on the other hand of its L-edge, if analyzed with respect to the emission energy. Information on the L-edge would be otherwise not accessible due to the low energy of around 700 eV. Furthermore, the energy resolution of its K-edge measurement is significantly higher than for conventional XAS measurements. Thus, this is also referred to as high-energy-resolution fluorescence-detected XANES (HERFD-XANES). Another possibility to obtain information on these transitions is X-ray Raman scattering (XRS), which can also be used to get information on absorption edges of light elements such as oxygen or silicon.[30,32,33] However, the data acquisition time of such a measurement is comparably long. In this thesis, XES and RXES measurements are utilized to obtain information on the electronic structure of iron in all samples. Furthermore, the laser-heated samples are characterized after temperature quenching via optical Raman spectroscopy and XRD imaging.

In the framework of this thesis, three geologically relevant sample systems are investigated regarding their iron's electronic structure and are split into three separate studies that are introduced in the following. Furthermore, improvements on the experimental setup for the spectroscopic measurements are elaborated.

First, reaction products of the iron-bearing carbonate siderite ($FeCO_3$) that are relevant to the Earth's lower mantle chemistry are analyzed. Siderite itself has been investigated several times for a wide range of pressure and temperature conditions within the last decades.[26,30,33–39] Recently, it has been shown that $FeCO_3$ undergoes a complex chemical

transition when laser heated at pressure $> 50\,\mathrm{GPa}$ and new phases are emerging with highly complex structures, namely tetrairon(III) orthocarbonate ($Fe_4^{3+}C_3O_{12}$) and diiron(II) diiron(III) tetracarbonate ($Fe_2^{2+}Fe_2^{3+}C_4O_{13}$).[22,40,41] In contrast to the starting material siderite, the carbon in these phases is tetrahedrally coordinated, hence, they are referred to as sp^3-carbonates in the following. These phases are well understood on a structural level, but information on their electronic structure is scarce. Although the iron in both sp^3-carbonates is expected in high-spin (HS) state due to their Fe-O distance, an experimental confirmation was missing. Here, K$\beta_{1,3}$ XES is utilized to determine the spin state of iron in both sp^3-carbonates for *in situ* laser-heated and temperature quenched samples at pressures between 80 GPa and 85 GPa. Confirmation of the decomposition process of $FeCO_3$ and the emergence as well as spatial distribution of the sp^3-carbonates is probed via XRD and optical Raman spectroscopy imaging. Furthermore, newly found Raman bands are discussed in context of the sp^3-carbonates synthesis. This study is part of the research within the research unit "FOR 2125" that investigates **Carbo**nates at high **P**ressures **a**nd **T**emperatures (**CarboPaT**).

Second, the (ferric) iron-bearing oxide hematite (α-Fe_2O_3) is studied under cold compression. Recently, Bykova et al.[21] published a complex phase diagram of Fe_2O_3 with various different phases for pressure and temperature conditions that cover almost the complete lower mantle. Here, the focus is on the phases appearing under cold compression, i.e., the transition from α- via ζ- into Θ-Fe_2O_3, as there is a discrepancy in the literature about the spin states of iron in the respective phases. While Bykova et al.[21] and Greenberg et al.[42] report a two-step spin transition, Sanson et al.[25] report only one spin transition up to 79 GPa. Here, a detailed, pressure dependent study via K$\beta_{1,3}$-XES analyzes the spin states of all three phases along with high-quality VTC spectra for each phase. Furthermore, 1s2p RXES spectra of all three phases at high pressure are presented that support the findings of Greenberg et al.[42] of a delocalization of the electrons in the ζ- and Θ-phase.

Third, a pressure dependent study of the (ferrous) iron-bearing oxide wustite (FeO) is presented up to a pressure of 75 GPa. Although the studies in the literature report no spin transition in the investigated pressure range, a structural phase transition occurs between 16 GPa and 23 GPa,[43,44] probably depending on the used pressure transmitting medium and its hydrostatic properties. This transitions is accompanied by a distortion of the crystal structure from a cubic to rhombohedral symmetry. The effect of this distortion on the K$\beta_{1,3}$-line shape is discussed in comparison with the spectra of α-Fe_2O_3 that also show a slight distortion with pressure. Furthermore, the effect of a line-shape change with pressure without a dedicated spin transition on the **I**ntegral of **A**bsolute **D**ifference (IAD)[45] analysis is discussed with respect to its information value and influence on the interpretation of K$\beta_{1,3}$-XES data. Moreover, high-quality VTC spectra in the complete pressure range are presented and analyzed in the context of the distortion. Additionally, 1s2p RXES maps are presented in the cubic and rhombohedral phase.

Furthermore, spectroscopic measurements at high pressure conditions are challenging, due to the high absorbing sample environment of a DAC and require comparably long data acquisition times. During these studies, the experimental setup using a von Hámos spectrometer in combination with an area detector was significantly improved and the extent of improvement is elaborated in this thesis. In this context, the signal-to-noise ratio (SNR) is introduced as a quantification of the data quality and a lower limit is defined to obtain meaningful results for spin-state determination via K$\beta_{1,3}$-XES. Moreover, new spectroscopic opportunities are discussed.

This thesis is structured as follows:
In **Chapter 2**, the theoretical background of (resonant) X-ray emission spectroscopy will be elaborated along with the electronic characteristics of transition metals, in particular of iron, based on the ligand field theory and the electronic property of the spin state will be introduced.
In **Chapter 3**, the concept of DACs to achieve the extreme pressures of the lower mantle is explained, along with possibilities to determine the pressure inside the sample chamber. Additionally, the technical approach for the spectroscopic measurements at the synchrotron radiation beamline P01 is showcased.
In **Chapter 4**, the data extraction and analysis process is presented along with a discussion of the expected accuracy of the methods and possible sources of error.
In **Chapter 5**, the challenges of spectroscopic measurements inside DACs are elaborated and the improvements of the setup during the course of this thesis are reviewed with a focus on the change from forward scattering to a geometry in 70° horizontal scattering angle. In addition, the possibilities and requirements for further improvements, such as two-color RXES measurements, are considered. Parts of this chapter are published in Albers et al.[46]
In **Chapter 6**, the results of the study of the spin state determination of the sp^3-carbonates ($Fe_4C_3O_{12}$ and $Fe_4C_4O_{13}$) at about 80 GPa are presented and the requirements of the high-temperature measurements, *in situ* and *ex situ*, as well as the characterization methods, XRD and optical Raman imaging, of laser-heated samples are presented. Parts of this chapter are published in Albers et al.[23]
In **Chapter 7**, the results of the electronic structure measurements of Fe_2O_3 under cold compression are presented with focus on the α-, ζ- and Θ-phase. Additionally, the possibility of a delocalization process of the electronic states is considered. Parts of this chapter are published in Albers et al.[46]
In **Chapter 8**, FeO is analyzed up to a pressure of 75 GPa with focus on the cubic to rhombohedral distortion of the unit cell. The influence of a deviation from a regular octahedra on the XES signal will be discussed with regards to the significance of the IAD analysis. Parts of this chapter are published in Albers et al.[47]
In **Chapter 9**, the results of this thesis will be summed up with an outlook to future studies that will further extend the understanding of the influence of iron on the Earth's mantle and core chemistry and composition.

2 Theory

2.1 X-ray emission spectroscopy

In the following the principles of XES will be discussed, while following de Groot and Kotani.[48]
In an inelastic X-ray scattering process, an incident photon with the energy $\hbar\omega_1$, wavevector $\mathbf{k}_1$ and polarization λ_1 is annihilated by matter and a second photon with the energy $\hbar\omega_2$, wavevector $\mathbf{k}_2$ and polarization λ_2 is emitted. The measurable instance in such an X-ray experiment is the double differential scattering cross section (DDSCS), which describes the probability that a photon with the energy $[\hbar\omega_2, \hbar\omega_2 + \delta\hbar\omega_2]$ is detected at the solid angle $[\Omega, \Omega + \delta\Omega]$. The DDSCS can be written as

$$\frac{\mathrm{d}^2\sigma}{\mathrm{d}\Omega\mathrm{d}(\hbar\omega_2)} = \frac{\omega_2^2 V_s}{\hbar c^4}\left(\frac{1}{2\pi}\right)^2 W_{12} \tag{2.1}$$

with the transition rate as a sum over all intermediate and final states

$$\begin{aligned} W_{12} =& \frac{2\pi}{\hbar}\sum_f \frac{4\pi^2}{\omega_1\omega_2}\left(\frac{e^2\hbar}{mV_s}\right)^2 \delta(E_g + \hbar\omega_1 - E_f - \hbar\omega_2) \\ & \times \Big|\Big[\langle f|\rho_{\mathbf{k}_1-\mathbf{k}_2}|g\rangle\,(\mathbf{e}_1\cdot\mathbf{e}_2) \\ & + \frac{1}{m}\sum_i\left(\frac{\langle f|\mathbf{p}(\mathbf{k}_2)\cdot\mathbf{e}_2|i\rangle\,\langle i|\mathbf{p}(-\mathbf{k}_1)\cdot\mathbf{e}_1|g\rangle}{E_i - E_g - \hbar\omega_1}\right. \\ & \left. + \frac{\langle f|\mathbf{p}(\mathbf{k}_1)\cdot\mathbf{e}_1|i\rangle\,\langle i|\mathbf{p}(-\mathbf{k}_2)\cdot\mathbf{e}_2|g\rangle}{E_i - E_g + \hbar\omega_2}\right)\Big]\Big|^2 . \end{aligned} \tag{2.2}$$

This considers resonant and non-resonant electron-photon interaction in the form of $[e^2/(2mc^2)\sum_n \mathbf{A}(\mathbf{r}_n)^2]$, using first-order perturbation and $[e/(mc)\sum_n \mathbf{p}_n\mathbf{A}(\mathbf{r}_n)]$, using second-order perturbation theory in which $\mathbf{A}(\mathbf{r})$ is the vector potential of the photon. Purely magnetic terms are neglected in equation 2.2. $|g\rangle$, $|i\rangle$ and $|f\rangle$ are the initial (ground), intermediate and final states of the atom with energies of E_g, E_i and E_f, respectively. The polarization vectors $\mathbf{e}_1$ and $\mathbf{e}_2$ belong to the incident and emitted photon, respectively. The constants are the Planck's constant $\hbar$, the electron mass m, the speed of light c and the systems Volume V_s in which the photon is normalized. $\mathbf{p}(\mathbf{k})$ and $\rho_\mathbf{k}$ are defined as

$$\mathbf{p}(\mathbf{k}) = \sum_n \mathbf{p}_n \exp(-i\mathbf{k}\cdot\mathbf{r}_n), \tag{2.3}$$

$$\rho_\mathbf{k} = \sum_n \exp(-i\mathbf{k}\cdot\mathbf{r}_n), \tag{2.4}$$

with the sum over all electrons. Equation 2.2 consists of three terms, that are depicted Fig. 2.1 a). The first term occurs from the first-order perturbation of the $\mathbf{A}^2$ term and describes the so-called Thomson scattering, which will not be further elaborated here. Terms two and three describe the annihilation and creation of the incident and emitted photon, respectively. The difference between two terms is the order of annihilation and creation of the photon. From considerations of the energies, it follows that only the second term is resonant. Thus, equation 2.2 can be further simplified to

$$F(\hbar\omega_1, \hbar\omega_2) = \sum_f \left| \sum_i \frac{\langle f|\mathbf{T}_2|i\rangle \langle i|\mathbf{T}_1|g\rangle}{E_g - E_i + \hbar\omega_1 + i\Gamma_i} \right|^2 \cdot \delta(E_g - E_f + \hbar\omega_1 - \hbar\omega_2), \tag{2.5}$$

neglecting the non-resonant term and combining constant factors to the annihilation and creation operators $\mathbf{T}_1$ and $\mathbf{T}_2$, respectively. The finite core-hole lifetime in the intermediate state is taken into account by replacing its energy by the complex number $E_i \Rightarrow E_i - i\Gamma_i$. $\mathbf{T}_1$ and $\mathbf{T}_2$ represent the transition operators of the incident and emitted photons. For RXES experiments, equation 2.5 can be used directly. However, in case of non-resonant XES, further simplifications can be applied and will be discussed in the following.
As for XES applies $\hbar\omega_1 \gg E_B$, the photoelectron is excited into the high-energy continuum. Thus, the influence on the intermediate and final state is very weak, and they can be treated as independent of each other, which allows for some more simplifications. Intermediate and final state along with their energies can be written as

$$|i\rangle = |\Phi_\epsilon\rangle \, |i'\rangle \, , E_i = E_{i'} + \epsilon \tag{2.6}$$

$$|f\rangle = |\Phi_\epsilon\rangle \, |f'\rangle \, , E_f = E_{f'} + \epsilon \tag{2.7}$$

with the wavefunction of the photoelectron $|\Phi_\epsilon\rangle$ and its energy ϵ. This modifies equation 2.5 to

$$\begin{aligned} F(\hbar\omega_1, \hbar\omega_2) = \sum_{f'} \int \mathrm{d}\epsilon \rho(\epsilon) a^2 \left| \sum_{i'} \frac{\langle f'|\mathbf{T}_2|i'\rangle \langle i'|\alpha_c|g\rangle}{E_g + \hbar\omega_1 - E_{i'} - \epsilon + i\Gamma_{i'}} \right|^2 \\ \cdot \delta(E_g - E_{f'} + \hbar\omega_1 - \epsilon - \hbar\omega_2) \end{aligned} \tag{2.8}$$

with the almost constant dipole transition amplitude from a core state to the continuum a. α_c is the annihilation operator of the core electron and $\rho(\epsilon)$ its unoccupied density of states (uDOS). Assuming that the uDOS is approximately constant, the equation ultimately simplifies to

$$F(\hbar\omega_1, \hbar\omega_2) = \rho a^2 \sum_{f'} \left| \sum_{i'} \frac{\langle f'|\mathbf{T}_2|i'\rangle \langle i'|\alpha_c|g\rangle}{E_{f'} - E_{i'} + \hbar\omega_2 + i\Gamma_{i'}} \right|^2 , \tag{2.9}$$

which is independent from the incident energy $\hbar\omega_1$. In fact, ρ might depend on $\hbar\omega_1$, which would tune the intensity of the experiment, but the spectral shape of the emission is independent of the incident energy.

Within the framework of this thesis iron-bearing compounds are studied by different types of X-ray emission spectroscopy. All emission lines result from the creation of a core hole in the 1s orbital of iron. The orbital that fills the core hole then differs between the emission lines and example spectra are shown in Fig. 2.2. For Kα emission the core hole is filled by an electron of the 2p level. The Kα emission is split into the $K\alpha_1$ and $K\alpha_2$ line, depending

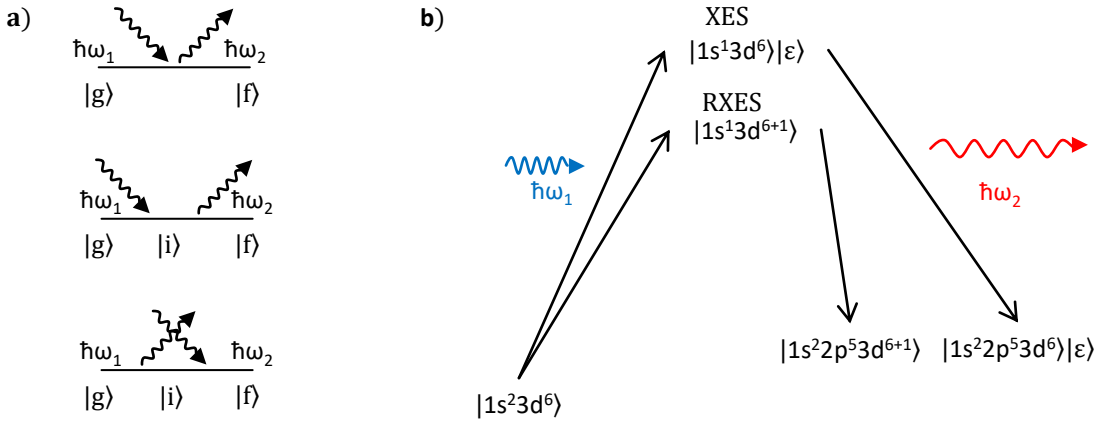

Figure 2.1: a) Schematic representation of the three scattering processes discussed in equation 2.2 in the same order (modified after[49] with permission by APS). **b)** Difference between XES and RXES scattering processes shown for Kα emission of Fe^{2+}. In case of RXES using Kα emission the core electron is excited into an empty 3d state and the core hole is subsequently filled by an electron of the 2p states (3p for Kβ emission). For XES the core electron is excited high above the partially filled 3d states and the core hole is again filled by a 2p or 3p electron for Kα or Kβ emission, respectively.

on whether the electron is decaying from the $2p_{3/2}$ or $2p_{1/2}$ level, respectively. Kα emission is the most intense emission measured here and is thus used for RXES measurements. For $K\beta_{1,3}$ emission, the core hole is filled by an electron of the 3p level. Due to the vicinity of 3p and 3d electrons, the Kβ emission is highly sensitive of changes in the occupation of the 3d levels. Depending on the spin state, i.e., the occupation of the 3d levels, a satellite peak (Kβ') emerges, around 15 eV lower in emission energy than the $K\beta_{1,3}$ peak. In the HS state the number of occupied 3d levels is maximized whereas in the LS state it is

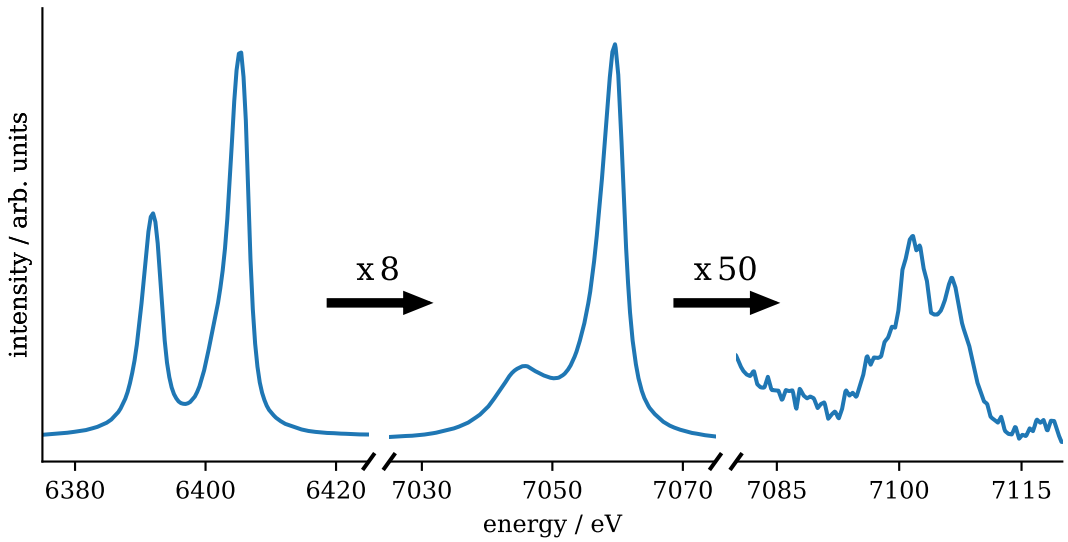

Figure 2.2: Comparison of iron Kα (**left**), $K\beta_{1,3}$ (**middle**) and VTC (**right**) emission, scaled in intensity for visibility.

minimized. The Kβ' feature is so prominent that a differentiation between HS and LS state could be performed qualitatively. However, techniques for a quantitative analysis are presented in Chapter 4, which is important if the sample contains several different phases or differently coordinated iron sites. Thus, $K\beta_{1,3}$ emission spectroscopy is the preferred choice for spin-state analysis. In contrast, RXES measurements are more challenging, as on the one hand its intensity is lower than for Kα emission and on the other hand the emission energy is close to the incident energy, which results in a strong background signal due to inelastic scattering. More details on this are elaborated in Chapter 5.
The third type of spectrum shown here is the valence-to-core (VTC) emission, which contains the iron $K\beta_{2,5}$ and Kβ" peaks. The $K\beta_{2,5}$ emission emerges from 3d orbitals of the central atom overlapping with 2p states of the ligand, whereas the Kβ" peak originates from the 2s orbital of the ligand. It has been shown, that the Kβ" intensity is strongly depending on changes in the bonding distance and its position is defined by the type of ligand.[50] Hence, VTC spectroscopy is highly sensitive to the coordination chemistry surrounding the central atom.

2.2 Ligand field theory

The electron configuration of isolated iron is $[Ar]3d^6 4s^2$, but in a covalently bond crystal its oxidation state and thus its electronic configuration changes, as electrons are hybridized with the ligand. Depending on the amount and type of binding partners, iron commonly occurs in two distinct oxidation states, as ferrous (Fe^{2+}) and ferric (Fe^{3+}) iron with the electron configurations $[Ar]3d^6$ and $[Ar]3d^5$, respectively. In an isolated iron atom all 3d orbitals are degenerated, but due to electron-electron repulsion with the negatively charged ligand, the 3d orbitals' energies split. In an octahedral coordination the neighboring atoms are located on the three main axes of the crystal. Hence, the presence of the ligands influences the orbitals differently and splits their energy levels. The e_g orbitals ($3d_{z^2}$ and $3d_{x^2-y^2}$) are occupying the main axes and are thus energetically unfavorable compared

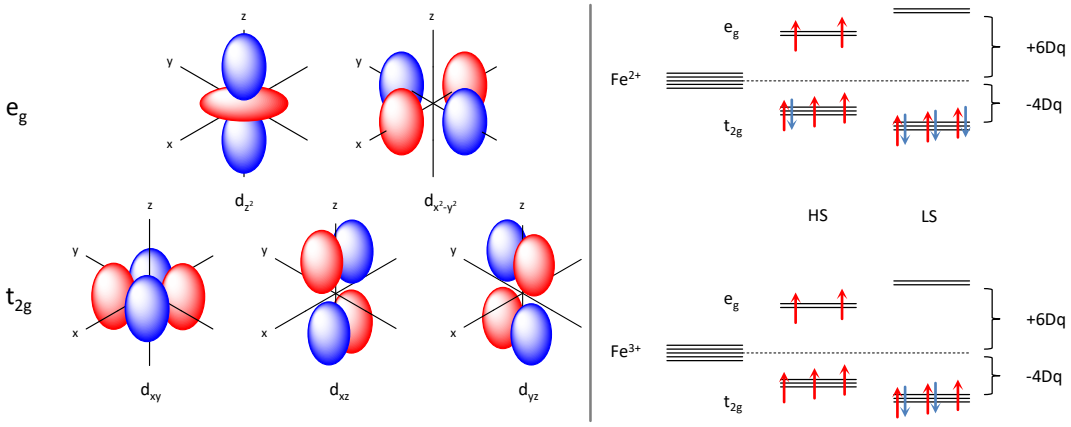

Figure 2.3: (**left**) Orientation of the 3d orbitals. (**right**) Splitting of the degenerate energy levels for an octahedral crystal field. A low crystal field causes a small splitting of the e_g and t_{2g} states and results in a HS state. By further increasing of the crystal field (e.g. by pressure), the splitting energy passes the spin paring energy and the electrons reconfigure into an LS state (modified after Lin et al.[51])

to the t_{2g} orbitals ($3d_{xy}$, $3d_{xz}$ and $3d_{yz}$), which are located in between the main axes. A sketch of the orbital orientations is shown in Fig. 2.3 a). Such a configuration can be occupied by the electrons in two ways, resulting in two spin states: Is the energy difference of the crystal field splitting (10 Dq) between e_g and t_{2g} states lower than the spin pairing energy, the orbitals are filled following Hund's rule and maximize the total spin of the system (high-spin (HS) state). Is the energy difference higher than the spin pairing energy, all electrons occupy the t_{2g} states and the total spin is minimized (low-spin (LS) state). This mechanism is illustrated in Fig 2.3 b). For ferrous (ferric) iron the total spin state then results in $S = 2.0$ (2.5) in the HS state and $S = 0.0$ (0.5) in the LS state. All systems in this thesis are in octahedral coordination and HS state at ambient conditions. Nevertheless, external factors such as pressure or temperature can change the sample's geometric structure and thus its electronic structure. A deviation from an ideal octahedron may split the energy levels further as shown by Westre et al.[52] Another important structure in geologically relevant materials is the tetrahedral coordination, in which the energy splitting in the e_g and t_{2g} is opposite to the octahedral coordination.
Furthermore, coordinations with an even lower symmetry might be present at conditions relevant in the geological context, leading to a further splitting of the e_g and t_{2g} levels and thus may result in an intermediate spin (IS) state with a total spin of 1.0 (1.5) for ferrous (ferric) iron. However, the existence of such a configuration is debated in the literature.[53–56] In this thesis, intermediate spin values are always a result of a mixture of either different iron sites with different spin configurations within one phase are a mixture of different phases with different spin states, e.g., as a result of laser heating.

3 Experimental setup

As explained in Chapter 1, the Earth's lower mantle ranges from 670 km to 2890 km in depth, which translates to pressure conditions of 24 GPa - 136 GPa,[1] while the temperature at the top of the lower mantle is estimated to ~2000 K. In contrast, the temperature estimations at the core-mantle boundary (CMB) range between 2600 K and 4400 K, depending on the used model.[3–8] Experiments at such conditions are difficult to perform and come in hand with certain challenges that have to be addressed. This chapter describes possibilities to achieve these high pressures and temperatures in a way that also allows for *in situ* X-ray spectroscopy experiments, which are further explained at the end of the chapter.

3.1 Diamond anvil cells

In the framework of this thesis, experiments were conducted at pressures up to 85 GPa. In order to achieve such high static pressures, the use of diamond anvil cells (DACs) is a commonly used technique. In this process, the sample is positioned between two diamonds with small culets, pressed against each other. The sample is held in position by a metal gasket such as rhenium, beryllium or steel. To guarantee a fixed position of the diamonds, they are glued to diamond seats made of either tungsten-carbide or polycrystalline diamond. A movement of the diamonds would lead to their destruction and the failure of the experiment. The diamond seats are mounted inside a steel body, called cell, that is equipped with screws to apply force to the diamonds and thereby pressurize the sample. The exact structure of the steel body varies between the different cell types. In this study, a Boehler-Almax type[57] and a special BX90 type[58] cell with enlarged radial opening (BX90-RO) were used. The radial opening allows for data acquisition in ~70° scattering angle, which has great advantages for X-ray emission spectroscopy and will be elaborated in Chapter 4.
Within this study, various kinds of diamonds were used due to requirements of the cell types and distinct advantages of each diamond type. The Boehler-Almax type cell functions

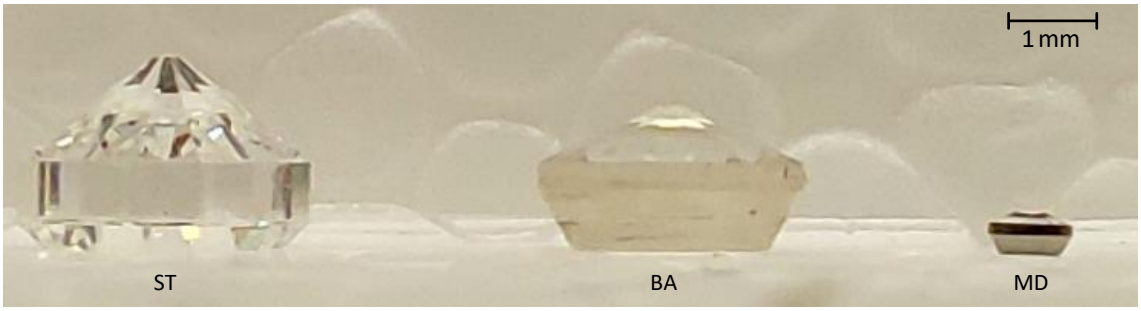

Figure 3.1: Photography of all three diamond types used in this thesis to illustrate shape and size differences.

exclusively with Boehler-Almax diamonds (BA), which have the highest aperture and are therefore most suitable for X-ray diffraction studies, but have disadvantages in X-ray spectroscopic studies, due to their limitations to forward and backward scattering geometry. The BX90-RO cell on the other hand works with a setup containing two different diamond types. Both possible setups require a standard diamond (ST) on the side where the emission signal is measured. The ST is shaped differently compared to the BA and has an increased height of 2.3 mm instead of 1.72 mm. On the opposite side, the ST can either be combined with a BA or a mini diamond (MD).[59] The MD has the same shape as the BA but its size is much smaller, i.e., a height of 0.5 mm instead of 1.72 mm. Thus, the absorption of the incident X-ray beam, penetrating through the upstream diamond, is reduced, which is of utmost importance for the RXES measurements but also provides significant advantages for the XES measurements. Fig. 3.1 shows a photography of all three diamond types for comparison. In the ideal case, XES will be measured on the downstream side due to the lower height of the BA compared to the ST, but both orientations are possible for XES if the beamline requires a specific geometry. In case of RXES, the use of a MD on the upstream side is essential and the emission can only be measured on the downstream side. The maximum pressure achievable by a DAC is determined by the culet size.[17] Furthermore,

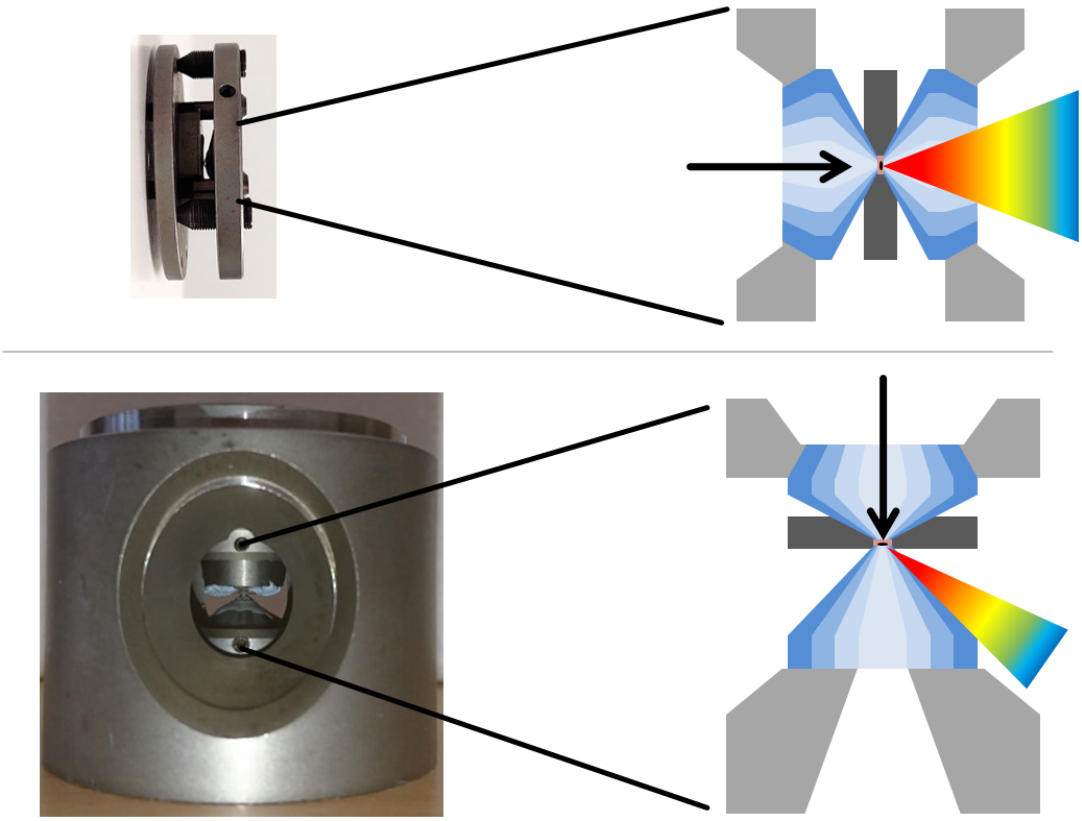

Figure 3.2: (top) Photo of a Boehler-Almax type cell (left) and an enlarged schematic of the scattering geometry in forward scattering geometry (right). **(bottom)** Photo of a BX90-RO cell with a view on the radial opening (left) and an enlarged schematic of the scattering geometry with 70° scattering angle (right). The incoming X-rays (black arrow) penetrate the BA/MD and hit the sample in between both diamonds. Subsequently, the polychromatic emission signal is scattered sideways out of the cell (rainbow-colored cone).

the use of an additional bevel to soften the crossover between culet and pavilion is optional and further stabilizes the diamonds at high pressure.[60] For a pressure of 80 GPa, different diamond setups were utilized with culet sizes ranging between 120 µm and 200 µm. To set this into context: Modern DACs are able to reach several hundred GPa and even pressures in the terapascal range.[61–65] These DACs are equipped with special double-stage diamonds with a second stage of diamonds with very small culets on top of the first stage of diamonds. More details on this can be found in O'Bannon et al.[17]
At such high pressures as in this thesis, it is important to guarantee quasi-hydrostatic conditions, which is achieved by a pressure transmitting medium surrounding the sample. There are several possibilities of a pressure medium like alcohols and salts but the best hydrostatic conditions provide noble gases such as helium, neon or argon,[66–68] especially at higher pressures. Although helium provides the best hydrostatic conditions,[68] it has turned out to be more destructive to the diamonds than other pressure media. A possible explanation is that the helium is small enough to infiltrate micro-cracks in the diamond while pressurizing the sample, which then leads to their destruction during pressure release. Consequently, in this thesis only argon and neon were used as pressure transmitting media. To seal the sample volume between the diamonds and hold the pressure medium as well as the sample in place, a rhenium plate of about 200 µm thickness is used as gasket material.

3.1.1 Diamond anvil cell preparation

In the following, a detailed description of the DAC preparation for BX90-RO cells will be given and the new approach to ensure a radial opening will be discussed. The preparation process will be described for a setup containing ST and BA diamonds but BA and MD are interchangeable in this context.
To begin the preparation process, first the ST diamond has to be glued on top of the flat tungsten-carbide seat. As a BX90 cell has no degree of freedom to adjust the culet angles parallel to one another, the culet of the ST is taken as default. In the next step, the BA is positioned into its seat and both diamond culets are brought closely together. Both seats can be shifted horizontally by four screws each, to position the culets exactly above each other. Simultaneously, the culets have to be aligned as parallel to each other as possible, which is achieved by slight rotations of the BA inside its seat. Thus, the BA is aligned by alternating translation and rotation. To check the degree of parallelism, both culets are brought closely together, until interference pattern appear. The less orders of interference can be detected, the more parallel the culets are. It has been shown that one order of interference comply to a good alignment for 200 µm culets. This corresponds to a misalignment of less than 0.1°. When both diamonds are positioned

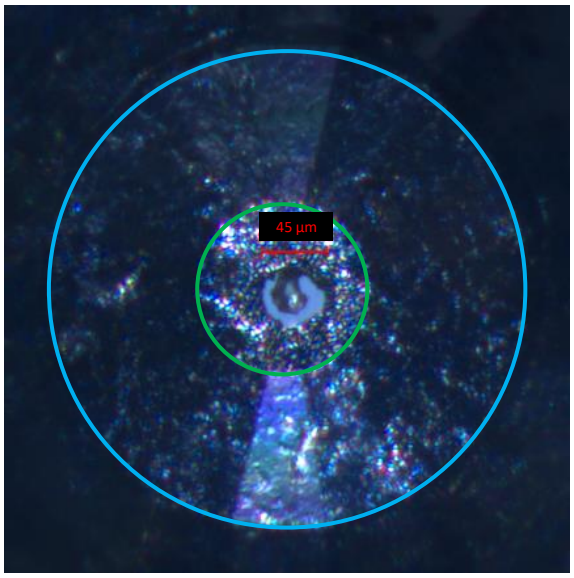

Figure 3.3: View on the sample chamber through the backside of a diamond with a culet size of 120 µm and a bevel size of 300 µm. The sample chamber is around 45 µm in diameter with the sample in its center. Green and blue circles highlight culet and bevel rim, respectively.

correctly, they are carefully pressed against each other to avoid a movement while applying glue to the BA. This step is very critical as too much force on touching diamonds can result in their destruction.
In the next step, the rhenium plate has to be prepared to function as a gasket. For high-pressure experiments in the vicinity of megabar pressures, the usual approach is to preindent the rhenium gasket of about 200 µm to a thickness of 20 µm - 30 µm to prevent the sample chamber from closing or moving while increasing the pressure due to movement of the rhenium. In the framework of this thesis, a new gasket preparation technique for BX90-RO cells was applied to ensure an (R)XES scattering angle of 70° with respect to the incoming X-rays. A schematic of the geometry is visualized in Fig. 3.2. To achieve this, the indentation process is split into two parts. First, the gasket is preindented to a thickness of about 50 µm. Second, the gasket is flipped by 180° and indented to the final thickness of 20 µm - 30 µm. As both diamond types have different pavilion angles, the ST penetrates further into the gasket than the BA. By flipping the gasket, this effect is reversed which leads to a shallower indentation depth on the ST side. Also, the horizontal distance between the center of the culet and the rim is increased due to the pavilion angle of the BA in the first indentation step. Thus, a smaller angle between culet surface and gasket rim is achieved which enables (R)XES measurements in 70° scattering geometry. Moreover, the use of an asymmetric seat setup, i.e., a higher ST seat and a lower BA seat, enhances the opening angle even further as the sample is no longer in the center of the DAC but shifted along the incident beam which enlarges the opening of the cell towards the ST side.
To create a sample chamber, a hole is drilled into the central part of the gasket's indented part. Its size typically ranges between 30% and 50% of the culet size, which leads to holes between 40 µm and 100 µm in diameter for the samples presented here. Such small holes can be drilled either by an electrical discharging machine or a laser. In the next step the sample can be placed on top of the ST culet and is ideally positioned in the center of culet and hole. However, slight inaccuracies during drilling the sample chamber might result in a small offset with respect to the culet's center. Samples with a size of 10 µm - 40 µm were used in the framework of this thesis. Optionally, a marker can be placed next to the sample to allow for pressure measurements by ruby fluorescence or XRD as explained in the next section. Depending on the sample chamber's size, it is possible to place several samples in one DAC, which increases the amount of information for a given set of diamonds and cells. If such an approach is applied, it is of utmost importance to ensure a sufficiently large distance between the samples to avoid crosstalk of different signals. The distance should be at least a full beamsize. It was verified for each cell in this thesis that no crosstalk was happening by measuring the XES signal while moving from one sample to another. If no signal could be detected in between the sample, the distance was large enough.
As mentioned previously, noble gases in the sample chamber ensure quasi-hydrostatic conditions. The gas-loading process was suggested by Mills et al.[69] Therefore, the cell is opened for a few µm to create a gap between diamond and gasket. Afterwards, the cell is floated by noble gas and the pressure of the gas is increased up to 2000 bar. When the maximum pressure is reached, the cell can be closed and the sample is surrounded solely by the pressure medium. The Boehler-Almax cell was gas loaded in the University of Frankfurt whereas all BX90-cells were loaded at Deutsches GeoForschungsZentrum (GFZ) in Potsdam.[†]

[†]The gas-loading process was supported by Lélia Libon, Hans Josef Reichmann, Georg Spiekermann and Max Wilke in Potsdam and Lkhamsuren Bayarjargal in Frankfurt.

3.1.2 Pressure determination

An exact pressure determination during an experiment is from utmost importance and can be achieved by different approaches. For XRD, a pressure marker is added to the sample chamber with a well known equation of state (EOS). Typically used markers are metal standards such as Au, Pt, Ta, W, Cu, and Al.[70] However, XRD measurements for samples in DACs require highly focused synchrotron radiation and time slots at suitable beamlines dedicated for XRD are usually scarce. Furthermore, XRD cannot be added to every synchrotron radiation experiment due to limitations of the beamline. As it was not practical to perform it at most experiments in this thesis, this method was not used. Another method of pressure determination is the shift of the ruby fluorescence line. This method also requires a pressure marker in the sample chamber, a ruby (Al_2O_3:Cr^{3+}). Although this method is easier to establish, as the ruby can be excited by a laser, it is more difficult at higher pressures because the ruby fluorescence line is significantly loosing intensity at high pressures. Furthermore, the ruby may limit the available space in the sample chamber and is thus suboptimal, especially for DACs containing more than one sample.
The third option is the pressure determination by the shift of the high-frequency Raman band of the diamond's culet, which was applied in the framework of this thesis. This method was proposed by Handfland and Syassen in 1985,[71] as they discovered a dependency between the first-order Raman band position and the nominal stress onto the diamond culet. Thus, for this method a Raman spectrometer is required. The process of optical Raman spectroscopy is described in Chapter 6. The pressure calibration used in this thesis was published by Akahama et al.[72] and describes the correlation between pressure in the center of the sample chamber and the diamond's Raman band shift. The pressure follows the equation

$$P[\mathrm{GPa}] = K_0 \frac{\Delta\nu}{\nu_0}\left[\frac{1}{2}(K_0' - 1)\frac{\Delta\nu}{\nu_0}\right] \tag{3.1}$$

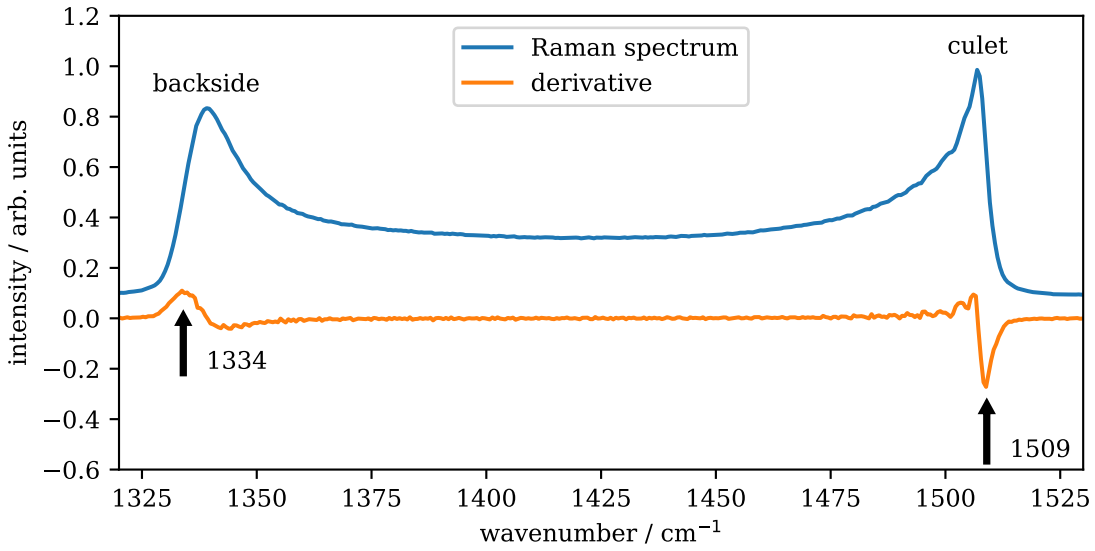

Figure 3.4: Example of a Raman spectrum of diamond in a DAC with the sample at high pressure (blue) and its derivative (orange) to determine the high-wavenumber edge position. The given values result in a pressure of 84.7 GPa.

with the diamond's Raman band frequency at ambient pressure ν_0 and its shift during pressure increase $\Delta\nu$. K_0 and K_0' are the linear and nonlinear coefficients of the diamond's EOS with the values 547 GPa and 3.75, respectively. Fig. 3.4 shows a Raman measurement of a BA diamond in a DAC at high pressure. If the Raman spectrometer is calibrated correctly, the Raman band position of the unpressurized diamond is at 1334 cm^{-1}. This can be checked by focusing the laser onto the backside of the diamond. To determine the pressure in the sample chamber, the laser has to be focused to the culet of the diamond. This way, the laser is probing the band shift, i.e., the pressure, through the whole diamond with the pressure of the sample chamber at the high-frequency edge, which is determined by calculating the derivative of the Raman spectrum and identifying the position of the minimum. The values in Fig. 3.4 result in a pressure of 84.7 GPa. Although Akahama et al.[72] report an accuracy of 3 % for their calibration, the pressures in this thesis are estimated with an uncertainty of 5 % of the determined pressure to account for inaccuracies during the measurement process.

3.2 X-ray emission spectroscopy

In this thesis, all (R)XES measurements were performed at beamline P01 of PETRA III (DESY).[73] The incident energy was monochromatized by a double crystal monochromator using the Si(111) or Si(311) reflection, depending on the required energy resolution, and varied between 7000 eV and 7300 eV for RXES or fixed to around 10400 eV for XES measurements. Latter provides a good compromise between transmission through the upstream diamond and absorption by the sample. The beamline can be focused down by a Kirkpatrick-Baez mirror system to a minimal beamsize of $4 \times 7\,\mu\mathrm{m}^2$ while providing a high photon flux of $\sim 8 \times 10^{13}$ ph/s at 10400 eV and $\sim 6 \times 10^{13}$ ph/s at 7100 eV using Si(111) monochromator. The Si(311) monochromator provides 20% of the intensity, i.e., $\sim 1.2 \times 10^{13}$ ph/s at 7100 eV. These are ideal conditions for spectroscopycal analyses inside DACs. The beamsize during the experiments in this thesis was typically between $7 \times 7\,\mu\mathrm{m}^2$ and $8 \times 8\,\mu\mathrm{m}^2$ full width at half maximum (FWHM).[†]
In order to perform (R)XES, a von Hámos spectrometer[74] was utilized in combination with a Pilatus 100K area detector. The principle of the von Hámos geometry is a cylindrically bent analyzer crystal system, which on the one hand focuses the signal to the center of the geometrically assumed cylinder and on the other hand projects the radiation wavelength dispersively on the cylinder axis. The combination with an area detector allows for data acquisition of Fe-Kα and Fe-Kβ, including VTC, in a single shot fashion. This setup was successfully utilized numerous times in the past.[23,29,30,33,46,47] The von Hámos spectrometer used here is equipped with four analyzer crystals. For Fe-Kβ emission spectroscopy, Si(110) crystals were used and the emission was measured by the Si(440) reflection, whereas Si(111) crystals were used for Fe-Kα detection utilizing the Si(333) reflection. The height of the analyzer crystals in vertical scattering geometry for a given energy E and lattice pattern distance d can be calculated by

$$s_H = \cot\left(\arcsin\left(\frac{hc}{2 \cdot Ed}\right)\right) \cdot R \tag{3.2}$$

with the Planck constant h, the speed of light c and the bending radius of the analyzers R. The detector is positioned twice as high.

[†]The (R)XES experiments were supported by Hlynur Gretarsson, Conrad Hagemeister, Johannes Kaa, Lélia Libon, Robin Sakrowski, Georg Spiekermann, Martin Sundermann, Christian Sternemann, Nicola Thiering and Max Wilke.

With a crystal height of $l = 3.2\,\text{mm}$ the energy window can be calculated by

$$E_{-}^{+} = \frac{hc}{2d \cdot \sin\left(\arctan\left(\frac{R}{s_H \pm 0.5 \cdot l}\right)\right)} \tag{3.3}$$

with the highest and lowest energy E^+ and E_-, respectively. A representation of the energy windows for Si(440) and Si(333) reflections is shown in Fig. 3.5. Consequently, the total energy window is the difference between both energies.

As the scattering geometries for Kα and Kβ emission are similar and the ideal detector heights only differ by around 4 mm, a simultaneous measurement of both emission lines is possible, allowing for two-color experiments such as simultaneous 1s2p and 1s3p RXES. More details on this can be found in Chapter 5.
Due to its portability, the whole setup might be used at any beamline with the required beamsize and photon flux. At P01 the von Hámos spectrometer was positioned on a concentric rail with the DAC in its center, covering a horizontal scattering angle range of 90° (see Fig. 3.6). This way the scattering angle can be changed quickly and different cell types can be used efficiently during a single beamtime. However, the most efficient combination is the use of a BX90-RO cell with the spectrometer positioned at ~70° horizontal scattering angle, measuring the emission in between gasket and diamond seat. This way, the emitted photons penetrate only ~0.5 mm of diamond instead of 1.72 mm in case of a horizontal scattering angle of 0° and a BA on the downstream side, which increases the intensity of the sample by a factor ~16 and ~43 for Kβ and Kα emission detection, respectively. If a ST is positioned on the downstream side, the factor increases to ~56 and ~237, respectively.[20] To further improve the efficiency of this setup, a helium bag is positioned between sample, analyzer crystals and detector, preventing absorption of the emission signal by air and thereby increase the detected emission signal by a factor of ~5.[20]
It is important to minimize detection of photons on the detector that did not interact with the probed sample, especially in case of VTC emission due to its weak intensity. Ideally, the sample has to be measured in a vacuum chamber. Another option is shielding the primary beam from both, analyzer crystals and detector. This approach was chosen for the measurements presented in this thesis, as a vacuum chamber was not available.

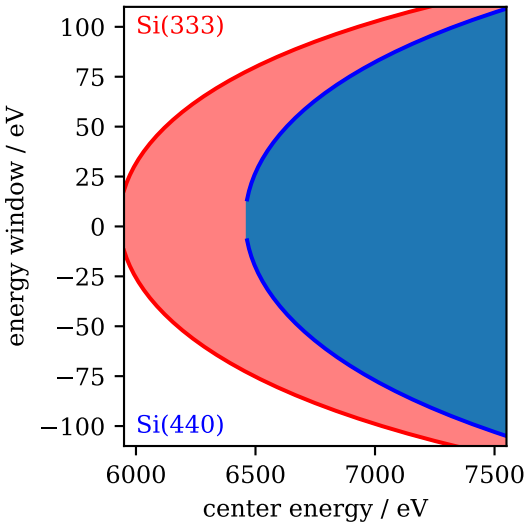

Figure 3.5: Energy windows for Si(333) (red) and Si(440) (blue) analyzer crystal reflections. The x-axis represents the energy at the center of the analyzer crystal and the colored lines represent the energy difference at the upper and lower end of the crystal with respect to the center energy. The shaded area is the total energy window of the crystal.

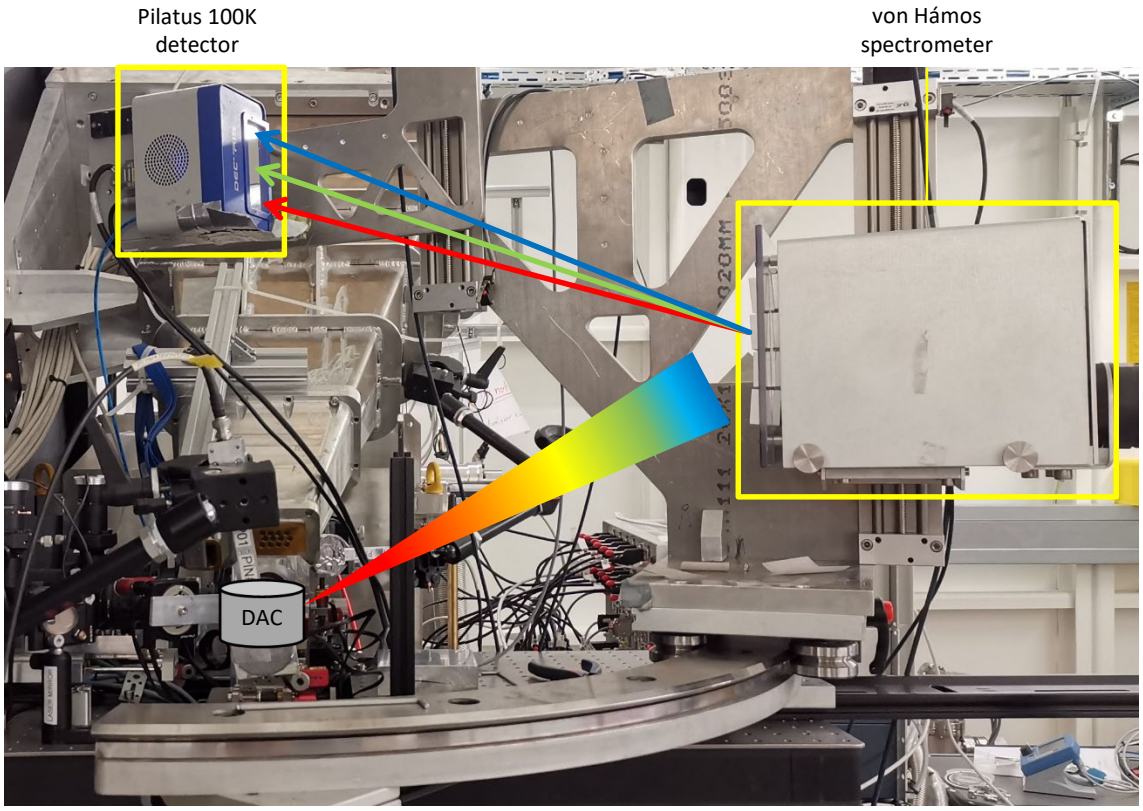

Figure 3.6: XES setup at beamline P01. The incident X-rays (direction out of the image) penetrate the upstream diamond and hit the sample inside the DAC. The polycromatic emission (rainbow-colored cone) is projected wavelength dispersively via the von Hámos' analyzer crystals onto the Pilatus 100K detector (red-green-blue). This setup shows the geometry for 70° scattering angle. For 0° scattering angle the von Hámos spectrometer has to be shifted to the downstream side (point of view).

Set up procedure of the spectrometer

Setting up the von Hámos spectrometer and the detector follows several steps that will be elaborated in the following.
First, the detector is positioned in the correct height with its X-ray sensitive area exactly above the sample and the von Hámos spectrometer is positioned on half the height of the detector in a horizontal distance of 500 mm to the sample and detector. The distance is measured from the front side of the analyzer crystals and the height of the spectrometer is measured in between all 4 crystals, leading to a slightly inaccurate height of all crystals. Moreover, fabrication inaccuracies may cause slightly different bending radii between all the crystals. Thus, the von Hámos spectrometer is equipped with a set of 3 motors for each crystal, resulting in a total of 12 motors. A representation of the effect of each motor on the signal on the detector is visualized in Fig. 3.7. In the next step, a small light bulb is placed at the sample's position to optically adjust all crystals and focus the photons from the sample's position onto the detector. After replacing the light bulb by the sample and exciting it by the X-rays, detection of emission signal on the detector should be possible. An example image of such a detector image is shown in Fig. 3.7 **A**. By a combined movement of motors #1 and #3 or complementary movement of motor #2 in the opposite direction

(red arrows), the crystals are adjusted in a way the detector detects photons, reflected by all crystals (**B**). Afterwards, all motors are moved in the same direction to achieve a better focusing of the crystals (green arrows, **C**). In the last step, the Bragg angle of the crystals is adjusted to the correct energy window on the detector by a combined movement of motors #1 and #2 or complementary movement of motor #3 (blue arrow, **D**).
Although the von Hámos is reflecting the emission signal wavelength dispersively, the Pilatus area detector does not have an energy calibration. Hence, the setup has to be calibrated for every experiment. Therefore, the incident X-rays are monochromatized to specific energies, that geometrically fit onto the detector window and the elastically scattered radiation is measured and thereby the energy of specific pixels is known. A linear fit through all energy and pixel pairs extends the information onto all pixel for each crystal on the detector. Although a fit using equation 3.2 would be more accurate, a linear fit is an adequate approximation and has shown to be more robust. The elastically scattered energy can either be measured directly at the same energy as the emission, or at a higher energy, utilizing a higher order of allowed Bragg reflections. In this thesis Si(555) and Si(660) reflections were used to calibrate the energy scale of Fe-Kα and Fe-Kβ (including VTC) detection.

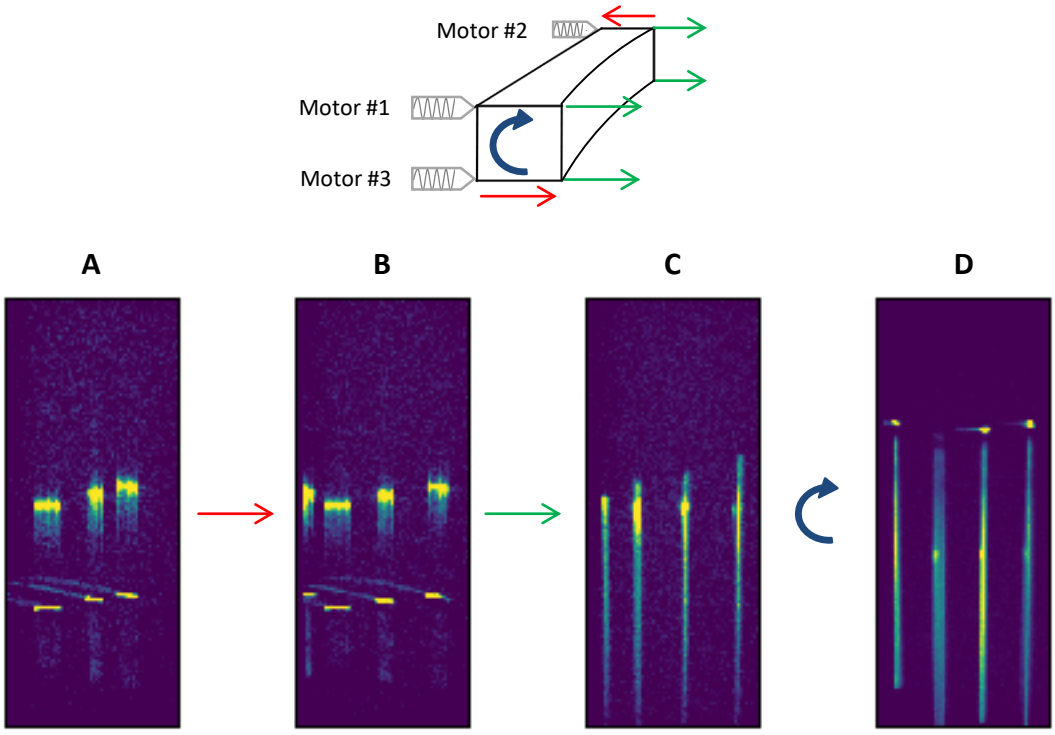

Figure 3.7: (**top**) Representation of a von Hámos crystal with its three adjusting motors. The colored arrows represent the possible movements of the crystal. The impact of each movement on the emission signal on the detector is shown underneath for several steps during the setup procedure (see text for details).

4 Data analysis

4.1 Data extraction

For a detailed analysis of the iron's electronic structure with consistent results in between samples, DACs and beamtimes, a consistent data processing of all experiments is of utmost importance. First, for each crystal a region of interest (ROI) is defined, which completely covers the signal from the sample. This ROI will then be summed up in the direction orthogonal to the energy axis and contains signal from the sample as well as background signal. To differentiate between signal from sample and background, the ROI is shifted in both directions next to the sample's ROI and also summed up. These ROIs only contain background signal, which can be subtracted from the original data. If the amount of pixels in the data and background ROIs is not identical, they have to be scaled by the difference factor. The data quality might be improved by approximating the background with a polynomial of higher order to suppress the noise. An example cut-out from the detector with all crystals and data as well as background ROIs is shown in Fig. 4.1 on the left. The corresponding raw spectrum and background are shown on the right along with a background subtracted spectrum. In case of spin-state analysis by the XES $K\beta_{1,3}$ measurements, all samples are normalized to their area between 7020 eV and 7120 eV to ensure comparable data from all samples. Furthermore, all spectra are interpolated to a grid of 0.1 eV steps, which was not applied to the RXES data. If all 4 crystals provide a spectrum of the same shape, they might be summed up to improve the data quality. However, they have to be energy calibrated first, which will be discussed in the following.

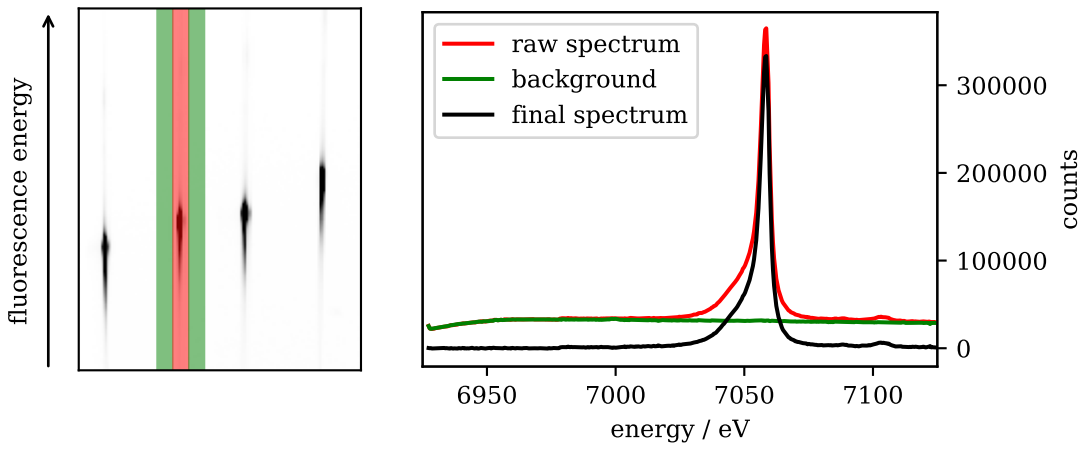

Figure 4.1: (Left) Cut-out out from a detector image with the signal of four Si(110) analyzer crystals. The red shaded area marks the ROI containing signal from the sample whereas the green areas solely contain signal from the background. As the background was calculated on twice as many pixels as the signal of the sample, its intensity was divided by a factor of two. (Right) Corresponding raw spectrum, background and background subtracted signal.

4.2 Energy calibration

The combination of a von Hámos type spectrometer with an area detector is a great way to perform spectroscopic measurements, as this approach provides a complete spectrum in a single-shot fashion and furthermore allows for measurements with multiple analyzer crystals. However, the detector has to be calibrated beforehand to assign its pixel scale to the correct energies. Therefore, the energy of the incident X-ray beam is set to different energies within the detector window and the elastically scattered X-rays are detected. The positions of these peaks were then determined by a Gaussian fit to the data and a linear fit through the different energies and positions then provides a pixel-to-energy assignment for the whole detector. The elastic lines might be measured using a different order of allowed Bragg reflections as the actual measurement. As stated in the previous section, the $K\beta_{1,3}$ emission was measured utilizing the Si(440) reflection, whereas for the elastic lines the Si(660) reflection was used with incident energies between 10500 eV and 10680 eV. This can be applied analogously to measurements of the $K\alpha$ emission using the Si(333) and Si(555) reflections. When using a higher order of reflection, the energies have to be scaled down by the factor

$$E_1 \cdot d_1 = E_2 \cdot d_2 => E_1 = E_2 \cdot \frac{\sqrt{h_1^2 + k_1^2 + l_1^2}}{\sqrt{h_2^2 + k_2^2 + l_2^2}} \tag{4.1}$$

using

$$d_x = \frac{a}{\sqrt{h_x^2 + k_x^2 + l_x^2}} \tag{4.2}$$

with the Miller indices h, k, l and the lattice parameter of the crystal a. An illustration of the calibration is shown in Fig. 4.2 for a detector image of elastic lines with 6 different incident energies. As the energy and thus the reflection angle is varied only by a small amount, a linear correlation between energy and signal position can be used for simplicity reasons, as it provides more robust results in the fitting procedure. It has been shown that this setup is very sensitive to slight alignment changes of the sample. Thus, a new calibration for each measurement is indispensable.

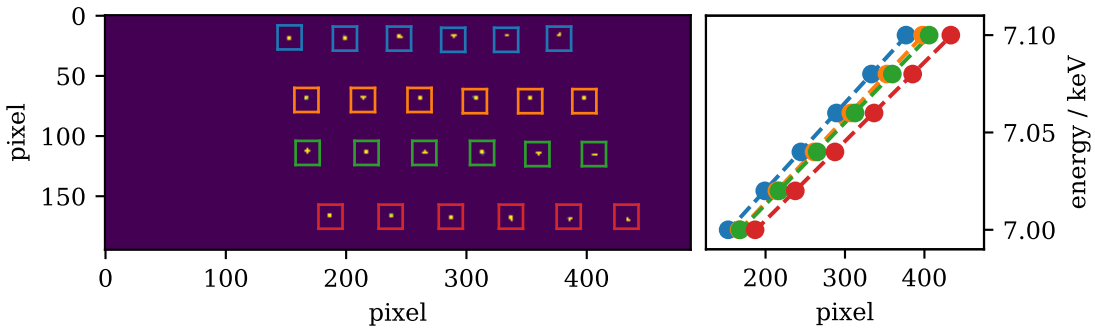

Figure 4.2: Detector image with elastically scattered X-rays (left) and corresponding energy positions (right). Thereby, the detector image is a summation of 6 measurements with different incident energies. The dashed lines are the fit through the data points represented by the colored squares on the detector image. Extrapolation of the dashed lines results in a calibration of the complete detector for each crystal.

4.3 Spin-state analysis

Different analysis techniques can be applied to evaluate the spin state of an iron-bearing sample. In this thesis, mainly the IAD[45] analysis is used. However, first momentum ΔM_1 shift[75] is also applied if possible and will be described in the following.
In the IAD analysis, all spectra have to be shifted so that their center of gravity (COG) is at the same energy position. Here, the COG was arbitrarily shifted to 7055 eV for all samples, as it is close to the actual COG before shifting it. The IAD value of each spectrum is then calculated by subtracting a reference spectrum with a known spin state from the analyzed spectrum. The resulting difference curve is then integrated using their absolute values. Fig. 4.3 a) shows this concept for a HS and LS spectrum with the LS spectrum as reference. The absolute value of the shaded area is the IAD value. With HS and LS references of known spin values, the IAD value of the analyzed sample can then be converted into a spin value. This method provides robust results for most of the spectra in this thesis. However, spectra with the same spin value as the reference spectrum might get systematically overrated, as the IAD value is the integration of the absolute values and the difference curve might solely consist of noise, which then leads to a positive IAD value.
The second method is the shift of the determination of the first momentum ΔM_1.[75] For this analysis, the spectra are analyzed on an absolute energy scale and its K$\beta_{1,3}$-COG is calculated using the main peak down to 50 % of its maximum intensity, as shown in Fig. 4.3 b). The ΔM_1 compared to a reference then provides information about the spin state in the sample. An exact energy calibration is of utmost important for this analysis technique. Thus, the spectra in Fig. 4.3 b) were measured during spin state imaging, i.e., the same energy calibration for both spectra. The error is estimated with 0.2 eV for each spectrum within one spin state map.

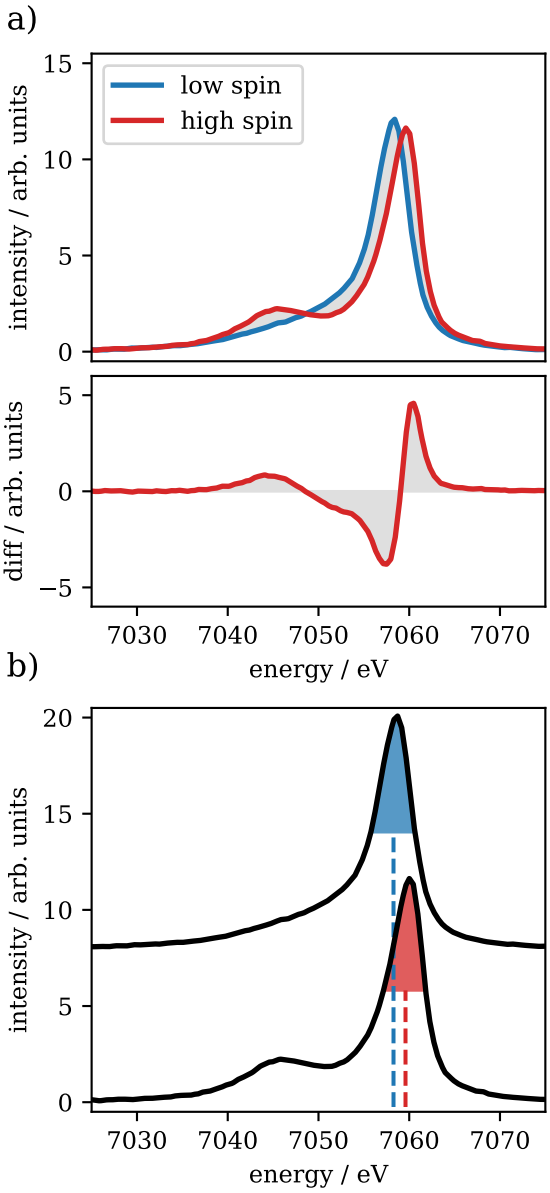

Figure 4.3: a) Fe-K$\beta_{1,3}$ emission for a HS and LS reference, shifted to the same COG. Underneath the spectra, the difference between both is visualized. The gray area highlights the difference. Integration of the absolute value of the gray area provides the IAD value. **b)** ΔM_1 analysis of the same HS and LS reference, shifted in intensity but unshifted in energy. The shaded areas highlight the energy range with more than 50% of the maximum intensity for the COG calculation. The dashed lines represent the COG positions.

A major source of error for the IAD analysis is the shift to the same COG, as low-quality spectra might be shifted to a slightly wrong energy. Fig. 4.4 shows the influence on the IAD value for five different spectra when the spectrum is shifted for 0.5 eV in both directions. Spectra with a high amount of HS iron show a linear response in IAD value to the shift in emission energy. The gradient for all three spectra is ~1.9/ eV as IAD value, which is close to 50 % of a complete HS - LS transition for 1 eV shift. Both spectra with a high amount of LS show a different behavior with a minimum in IAD value close to the unshifted spectra, as the spectra are close to the reference and the IAD value cannot be negative. However, starting from the minimum, the IAD value also increases linearly to both sides with around the same gradient. It has to be noted that an error in the COG of 0.5 eV would be unusually high for spectra with a reasonable data quality and does more likely not exceed 0.2 eV, resulting in an error of around 10 % of a complete HS to LS transition, which was assumed as error for the IAD analysis. Additionally, spectra with a spin state close to the reference spectrum might get systematically overrated and interpretation of these spin values has to be performed carefully.

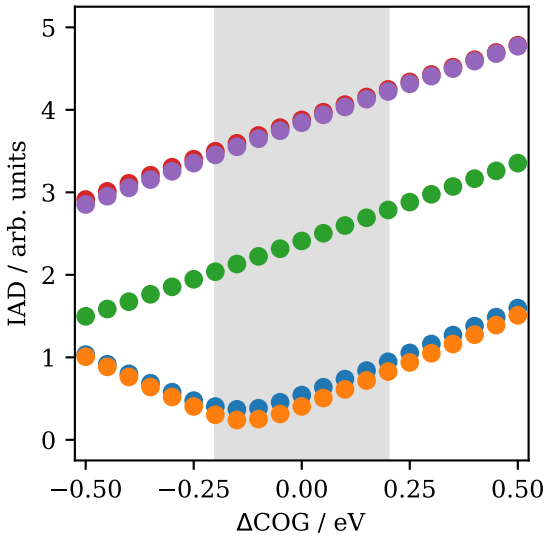

Figure 4.4: IAD values in dependence of a misalignment in the COG for the spectra shown in Fig. 5.4 a). The color code is consistent between both figures.

The energy shift of the complete HS - LS transition for the ΔM_1 analysis in this thesis is around 1.4 eV (compare Fig. 5.4 d)), which is in reasonable agreement with data from the literature.[75] As shown in section 5.1, a misalignment of only one pixel results in an energy shift of 0.42 eV and thus around 30% of a complete spin transition. Hence, this method is very susceptible to misalignment or inaccuracies in the energy calibration, which makes it difficult to compare spectra measured at different experiments. Even within one experiment, datasets from different measurements may vary. Thus, this technique can only applied to measurements with the exact same setup, e.g., during (*in situ*) spin-state imaging.

4.4 Resonant X-ray emission spectroscopy

RXES measurements are typically illustrated by a 2D intensity map, in which the x-axis represents the incident energy and the y-axis is shown on a energy transfer grid, i.e., incident energy subtracted by emission energy. Analysis of such a measurement is usually performed at constant emission energy (CEE) or at constant incident energy (CIE). An overview of the different methods is shown in Fig. 4.5 for 1s2p RXES of Fe_2O_3 at 11 GPa. CEE-cuts are diagonal lines within the RXES map and are probing the intermediate states during the two-photon process. Thus, they correspond to the final states of classical K-edge XANES measurement, but with a substantially improved energy resolution. Hence, this method is also known as HERFD-XANES. The integration range of a CEE-cut is always

a compromise between energy resolution and data quality, but in all cases the CEE-cut should include all observable transitions. The blue shaded area in Fig. 4.5 a) visualizes the integrated CEE range for a width of 3 pixels, i.e., ~1.1 eV, with the result in the plot underneath, compared to higher integration widths.

Another type of analysis are the CIE-cuts, which probe all final states for a constant intermediate state. Thus, this is analogue to the final states in probed L- and M-edge absorption for 1s2p and 1s3p RXES, respectively. For a complete picture of the analysis all

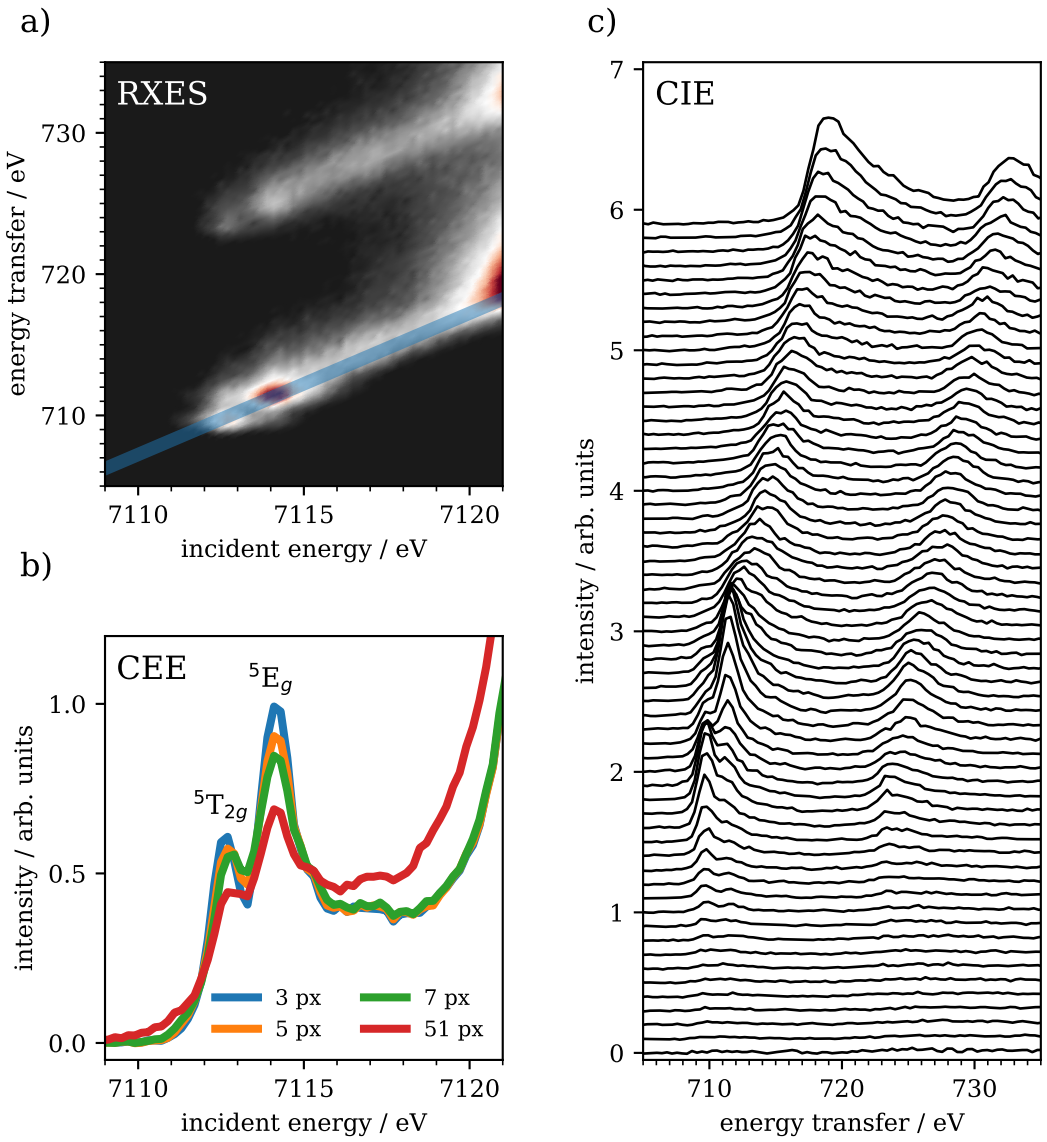

Figure 4.5: a) Complete RXES map of Fe_2O_3 at 11 GPa. The blue shaded area marks the CEE-cut with a width of 3 pixels, shown in **b)** along with higher integration widths for comparison. **c)** CIE-cut for every 0.2 eV step in incident energy between 7110 eV and 7120 eV, set off in intensity for clarity. Both localized $^5T_{2g}$ and ^5E_g states appear constant on the energy transfer grid due to their discrete character.

CIE-cuts have to be analyzed as shown in c). The dispersion characteristics of an electronic transition may provide further information about its localization. A discrete localized transition is constant on an energy transfer grid, whereas delocalized transitions show a linear dispersion with the incident energy.[76–80] However, overlapping discrete transitions may also appear as dispersing with the incident energy. In Fig. 4.5 the $^5T_{2g}$ and ^5E_g states are showing discrete characteristics whereas states at higher incident energies are dispersing with the incident energy.

5 Discussion of the scattering geometry

The scattering geometry in ~70° horizontal scattering angle was a key improvement for several aspects of (R)XES experiments, which will be elaborated in the following.

5.1 Energy calibration

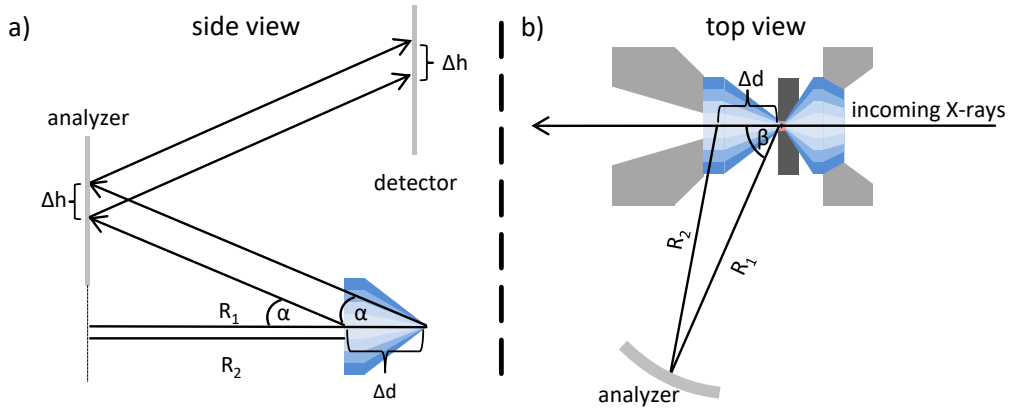

Figure 5.1: a) Sketch of the deviation in signal height (Δh) of an elastic line scattered by the bottom end of the diamond in forward scattering. The scattering angle α is defined by the X-ray's energy and the analyzer crystal. b) Schematic of the change in radius for a scattering angle of β between scattering close to the sample and at a point inside the diamond. The difference between R_1 and R_2 then defines Δh.

For the calibration method by elastic scattering at a known energy, all photons are scattered ideally from the sample's position. However, for some sample environments, such as DACs, this is hard to achieve, as the incoming X-rays are scattered from every point in the diamond, which then results in a systematic error within the energy calibration. A sketch of the geometries is visualized in Fig. 5.1. The offset Δh of the detector position for a given energy between photons scattered from the sample position (R_1) and at another point of the diamond (R_2) is defined by

$$\Delta h = \tan(\alpha) \cdot (R_1 - R_2). \tag{5.1}$$

R_2 is thereby defined by

$$R_2 = \sqrt{R_1^2 - 2R_1 \cos(\beta)\Delta d + \Delta d^2} \tag{5.2}$$

with the horizontal scattering angle β and the deviation from the sample position along the incident X-ray axis Δd. In case of forward scattering, i.e., β =0, the deviation simplifies to $\Delta h = \tan(\alpha) \cdot \Delta d$. For an incident energy of 10500 eV and a downstream diamond of 1.72 mm (BA) thickness this results in a deviation of Δh = 0.72 mm. In case of 70°

horizontal scattering angle, i.e., $\beta = 70°$, and a diamond thickness of 2.28 mm (ST) the deviation is $\Delta h = 0.32$ mm. With a detector's pixel size of 172 µm this results in a deviation of around 4.2 px and 1.9 px for both geometries, respectively. Furthermore, in 70° scattering angle the analyzer will not detect signal of the whole diamond due to limitations of the cell. Thus, 1.9 px is likely the upper limit.

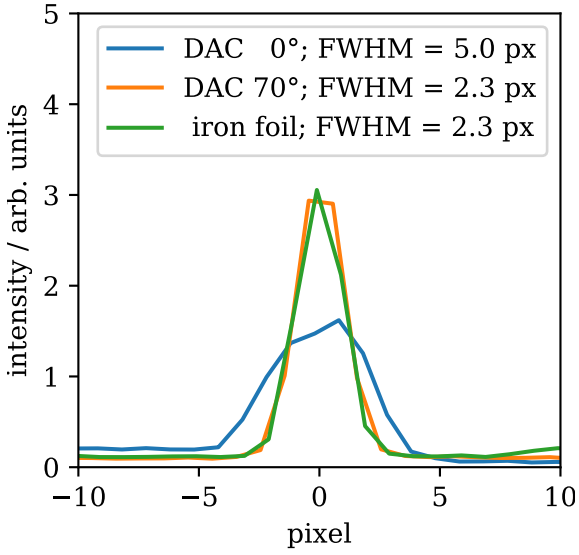

Figure 5.2: Comparison of two elastic lines at 10500 eV in 0° and 70° horizontal scattering geometry along with an elastic line scattered from an iron foil.

In Fig. 5.2 a comparison between both geometries with a sample inside a DAC are shown along with an elastic line scattered by a thin iron foil outside of a DAC. The thickness of the iron foil was only around 5 µm and can thus be neglected. All lines are measured with an incident energy of 10500 eV. The plot shows the expected result, as the FWHM of the elastic line in forward scattering is more than doubled compared to 70° scattering geometry. The comparison to the elastically scattered line by the pure iron foil shows no difference to 70° scattering, which verifies that the broadening of 1.9 px is only the theoretical upper limit but the effect on the experiment is negligible, as the field of view of the spectrometer onto the sample is small enough to only detect photons scattered from an area in the vicinity of the sample. It is important to emphasize, that this broadening is not statistically in both directions but systematically shifted to lower energies and thus translates into an absolute error on the emission energy. The energy scale at the Kβ emission is ~0.42 eV/pixel. As the center of the elastic lines shifts to half of the height deviation, the error on the absolute energy is around 0.9 eV in case of forward scattering. To set this in context, for the ΔM_1 analysis method this shift translates to around 65 % of a complete HS to LS transition, as shown in section 4.3.

5.2 Data quality

In the following, the improvements on the data quality will be highlighted with the signal-to-noise ratio (SNR) as quantitative evaluation. It is calculated in this thesis by

$$\mathrm{SNR} = \frac{I_p - I_b}{\sqrt{I_b}}. \tag{5.3}$$

with the peak intensity I_p and the intensity of the background I_b. Both intensities are absolute counts detected in the respective ROI on the detector. For I_b the intensity of the background is chosen at the same energy position but extracted from the background ROI. There are different approaches to improve the SNR. An example of all cases for an initial SNR of 1 is shown in Fig. 5.3 a). When increasing I_p with a constant I_b, e.g., by a higher amount of iron in the sample or an enlarged opening angle of the cell towards

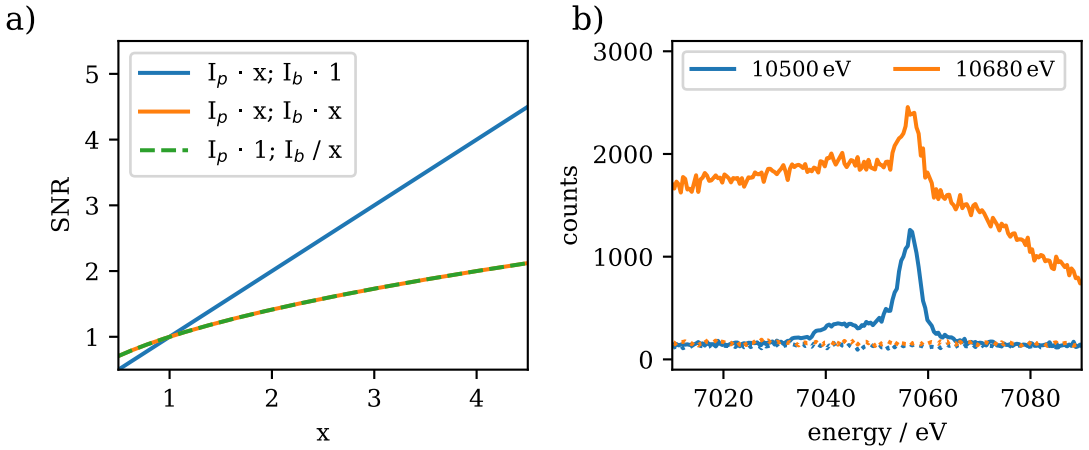

Figure 5.3: a) Influence of an increased intensity of the sample (blue), a total increase of counts (orange) and a reduced background (green) by the factor x on the SNR (see text for details). **b)** $K\beta_{1,3}$ emission for different incident energies. The dotted lines represent the background calculated by shifting the ROI next to the data ROI.

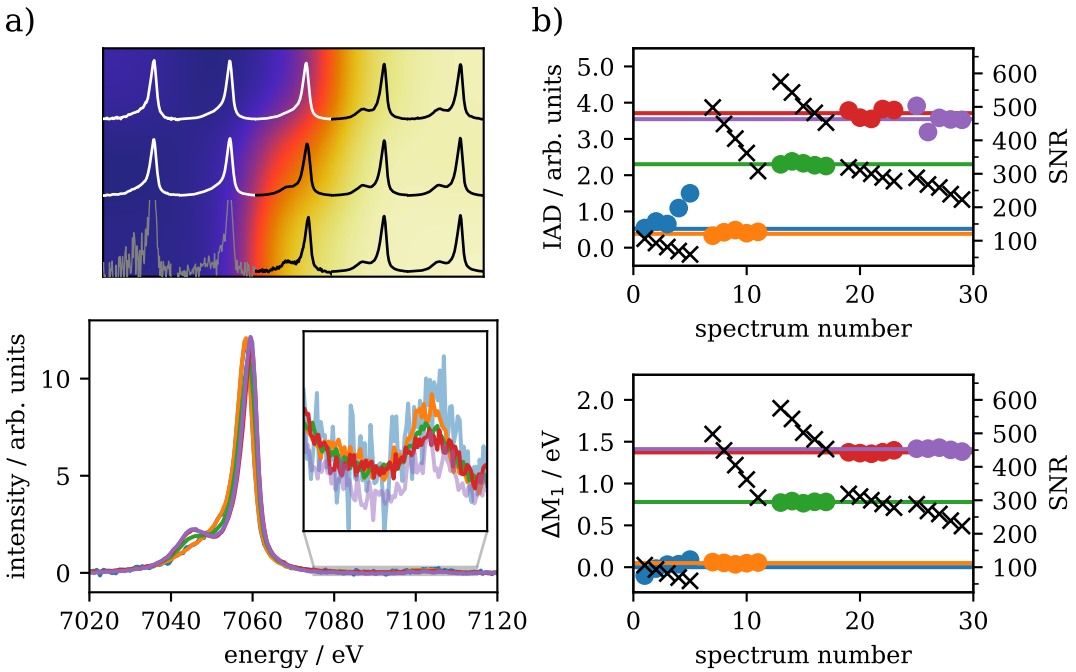

Figure 5.4: a) 3×5 spin map analyzed by IAD method with a step size of 7 µm in between positions of the *in situ* heated sample. The integration time was 5 minutes for each spectrum. Spectra within the map are plotted for representation of the measurement position. All spectra are normalized to their area and share the same axis scales. White and black spectra are shown on different colors for better visualization whereas the SNR of gray spectra is too low for a spin analysis. Underneath, the middle row of the map is shown with a zoom into the VTC area in the inset. **b)** IAD and ΔM_1 values for all 5 minutes spectra (lines) and each 1 minute spectrum (dots) for the middle row of **a)**. The black crosses represent the SNR for each 1 minute measurement (right scales). The color code is consistent for all plots (published in[46]).

the spectrometer, it is scaling linearly. In contrast, when increasing the amount of total counts of I_p and I_b by extending the data acquisition time or intensifying the photon flux on the sample, the SNR is scaling with the square root of the increasing factor. The same magnitude of improvement can be achieved by reducing the background intensity I_b. An easy but important way to decrease the backgrounds intensity is the choice of the correct incident energy. In Fig. 5.3 b) two $K\beta_{1,3}$ measurements of the same sample are shown for different incident energies. Both spectra were measured during energy calibration by elastically scattered photons, using the Si(660) reflection of the analyzer crystals. The incident energies of 10500 eV and 10680 eV are detected at the same detector positions as 7000 eV and 7120 eV, respectively, that are detected via the Si(440) reflection. At 10500 eV the position of the scattered photons on the detector is lower than the position of the $K\beta_{1,3}$ emission and no intensity due to Compton scattering is detected in the emission signal. In contrast, at 10680 eV the position of the scattered photons on the detector is higher than the position of the $K\beta_{1,3}$ emission and the intensity due to Compton scattering is dominating the spectrum. It has to be emphasized that both spectra are not shifted vertically for clarity and are calculated using the same ROIs on the detector image. Hence, an energy should be chosen whose position on the detector is either lower than 7000 eV or high above 7120 eV, regardless of the reflection order of the analyzer crystal, to prevent a strong background due to Compton scattering.

In Fig. 5.4 IAD and ΔM_1 analyses are compared for spin-state imaging of *in situ* laser-heated $FeCO_3$ at 75 GPa and set in context to their SNR (published in[46]). Spin-state imaging is the concept of measuring the $K\beta_{1,3}$ emission spectra on different position on the sample and evaluating the spin state for each unique position. The SNR was calculated using the maximum intensity of the $K\beta_{1,3}$ emission. The complete spin map is shown in Fig. 5.4 a) along with the spectra of a line over the sample. The spin map is calculated by IAD analysis with a spectrum of the sample before laser-heating as LS reference. Each position was measured for a total of 5 detector images with 1 minute integration time each, i.e., 5 minutes in total per position. In b) each 1 minute spectrum is analyzed by

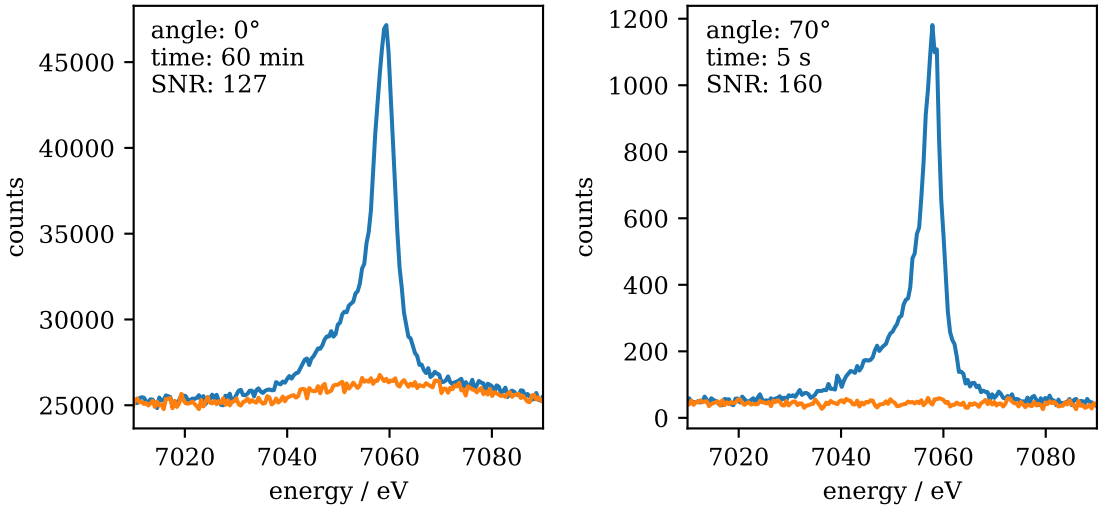

Figure 5.5: Comparison of different measurement times in forward scattering (left) and in 70° horizontal scattering angle (right) for high pressure $FeCO_3$. Both plots show a single analyzer crystal with a data (blue) and background (orange) ROI of 10 pixels each.

IAD and ΔM_1, respectively, with the colored lines corresponding to the analysis of the 5 minutes spectra. Furthermore, the black crosses represent the SNR of each 1 minute measurement. The data of the IAD analysis show, that the spin-state results for spectra with a SNR > 100 are stable and provide robust spin states, in line with their corresponding 5 minutes spectra. For lower SNRs, the resulting IAD values significantly differ from each other, which provides a lower limit of SNR > 100 for the IAD analysis. In contrast, ΔM_1 analysis is highly stable even for SNRs < 100. Nevertheless, as the accuracy of the energy scale is crucial for this analysis, it can only be applied for measurements with the exact same setup such as spin-state imaging. Furthermore, this means that only differences in between the spectra of such measurement can be compared and a comparison to data from the literature might not be possible.

With the SNR as quantitative evaluation of the spectra quality, improvements of the scattering geometry can be showcased. In Fig. 5.5 both geometries are compared regarding their SNR for a single analyzer crystal. The measurement in forward scattering with a diamond setup of ST and BA on the upstream and downstream side, respectively, was performed on laser-heated and temperature-quenched $FeCO_3$ at 85 GPa. The spectrum corresponds to sample C in Chapter 6 and is published by Albers et al.[23] In 70° horizontal scattering angle, the diamond setup consisted of an MD and an ST on the upstream and downstream side, respectively, and the measured sample was unheated $FeCO_3$ at 75 GPa. The spectra convincingly highlight the advantages of the improved geometry. Although the data acquisition time is decreased by almost three orders, the SNR in case of 70° horizontal scattering angle is improved from 127 to 160. Extrapolation to a minimal SNR of 100 results in a minimal measurement time of ~37 minutes for forward scattering and around 2 seconds for 70° horizontal scattering angle, a reduction of more than three orders of magnitude. It has to be noted that the sample in 70° horizontal scattering angle provided the best SNR of all samples and longer measurement times should be assumed for other samples. Nevertheless, an improvement of two to three orders of magnitude can be assumed when comparing both geometries.

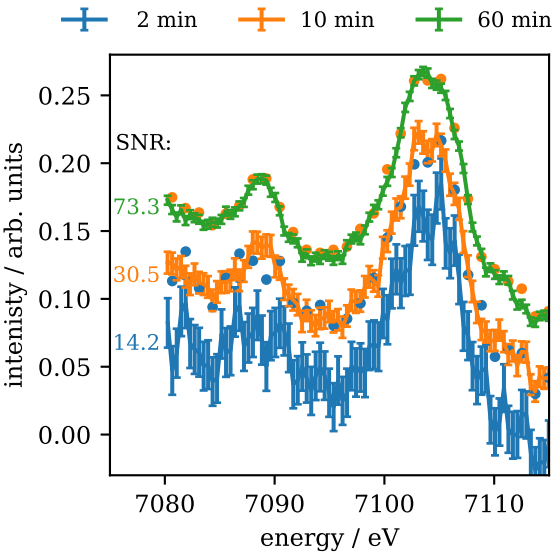

Figure 5.6: VTC region of Fe_2O_3 at 75 GPa for different integration times. The spectra are normalized to the complete $K\beta_{1,3}$ and VTC region and shifted in intensity for clarity. The dotted spectra represent the binned spectra of the same color with a binning size of 3 pixels (originally published in[46]).

With such an improvement of the experimental conditions, VTC measurements become feasible on reasonable time scales. Fig. 5.6 shows the VTC region of Fe_2O_3 at 75 GPa in 70° horizontal scattering angle with different integration times between 2 minutes and 60 minutes along with their SNRs. Although the spectrum after 2 minutes still contains noticeable noise, the $K\beta_{2,5}$ peak's position and intensity may be analyzed. With increasing integration time the SNR improves and after 10 minutes the data quality allows for determination of the Kβ" feature. For longer integration times the SNR improves more and more slowly.

One possibility to improve the SNR of the spectra is a binning of adjacent pixels as shown by the dotted spectra in Fig. 5.6. The binning size was three pixels, leading to an energy step size of ~1.2 eV. This in an adequate technique if the spectral width of the measured features is not narrower than the new energy step size. However, the maximum factor of improvement on the SNR cannot exceed the square root of the amount of binned pixel, which is ~1.73 in case of Fig. 5.6. The binning to ~1.2 eV emphasizes that a minimum acquisition time of 10 minutes is required for a reasonable data quality.

5.3 Two-color resonant X-ray emission spectrosopy

A further application that becomes feasible due to the improved experimental conditions is RXES. While in case of XES the use of an MD on the upstream side provides an increased intensity by a factor of 2 and thus is not essential for a successful experiment, for RXES measurements it is indispensable as it improves the photon flux by a factor of 15, due to the lower incident energy of around 7.1 keV.[20] Furthermore, the combination of significantly increased photon flux and the similar experimental geometries for Kα and Kβ emission detection allows for two-color experiments with simultaneous measurements of 1s2p and 1s3p RXES maps. This way the information of a single experiment is substantially

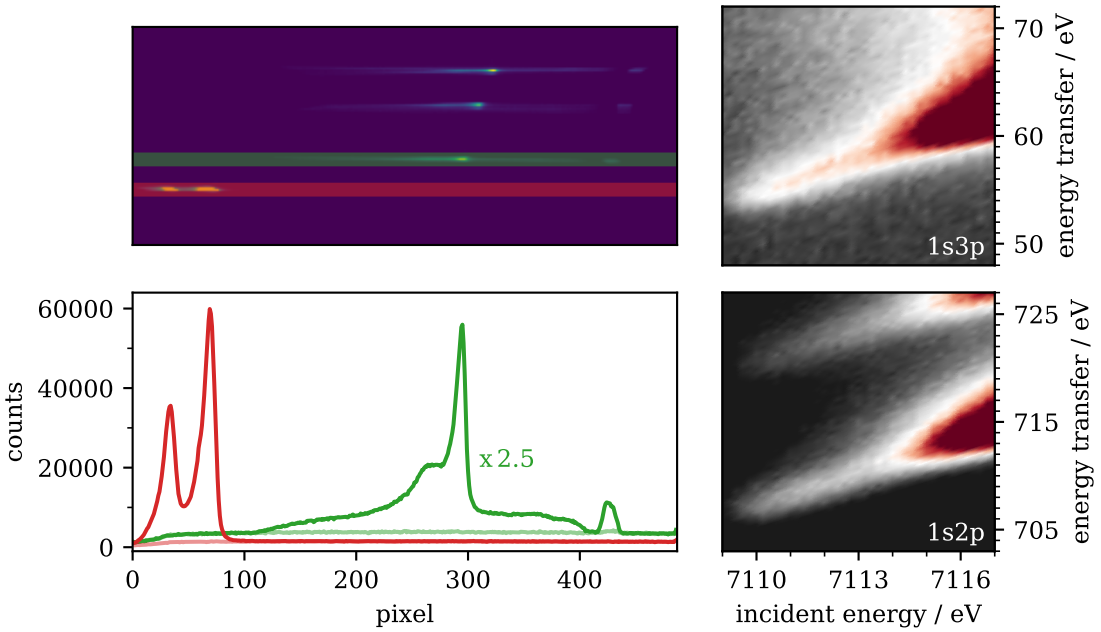

Figure 5.7: Simultaneous measurement of 1s2p (lower right) and 1s3p (upper right) RXES maps. The detector image (upper left) as well as the summed up crystals (lower left) were summed up for all incident energies between 7109 eV and 7115 eV. The Kβ emission is scaled with a factor of 2.5 to match the intensity of the Kα emission. The significantly increased background in the Kβ emission is due to Compton scattering of the diamond, as the incident energy is close above the emission energy. The background by the shifted ROI is shown as shaded lines of the same color as the emission and is nicely correlating to the pixel range in which no Compton scattering is detected, i.e., below pixel 100 and above pixel 450. The elastically scattered incident X-rays are visible around pixel 420.

enhanced. Nevertheless, 1s3p RXES measurements inside DACs bear further complications to the experiments. First of all, the background in the pre-edge region is considerably increased by Compton scattering of the diamond, as the incident energy is only about 50 eV above the emission energy. Additionally, the Kβ emission line is substantially less intense than the Kα emission line. This is highlighted in Fig. 5.7, which shows data from a two-color measurement of FeO at 34 GPa. The Kβ emission was scaled with a factor of 2.5 to roughly match the intensity of the Kα emission. However, around 15 % of the intensity is based on the increased background.

Despite these challenges, the combination of 1s2p and 1s3p RXES measurements adds more detailed information to an experiment. First, the experiment provides L-edge (1s2p) as well as M-edge (1s3p) like information. Second, 1s3p RXES allows for spin selective HERFD-XANES spectra,[80] as showcased in Fig. 5.8. The CEE-cut at the maximum intensity of the $K\beta_{1,3}$ emission at 7058 eV shows the expected pre-edge features, which are further analyzed in Chapter 8. In contrast, the CEE-cut at the Kβ' maximum at 7044 eV shows no particular pre-edge features but a constant rise of the absorption edge. Both spectra are integrated over 5 pixels each. These results verify that the features are solely based on spin-down transitions, as they are absent for spin-up transitions. More detailed information on this matter are published by Glatzel et al.[80]

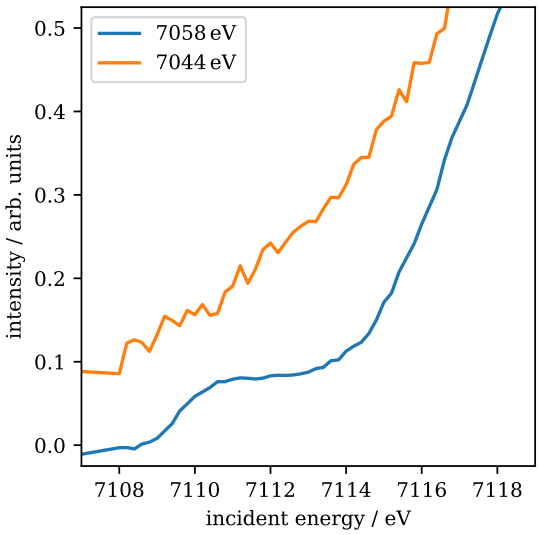

Figure 5.8: CEE-cuts at the $K\beta_{1,3}$ (blue) and Kβ' (orange) emission integrated over 5 pixels each of a 1s3p RXES measurement of FeO at 34 GPa.

For future applications, the setup has to be optimized further, especially by minimizing the additional background by the Compton scattering. As the incident X-rays are linearly polarized in the horizontal axis, a reduced background can be achieved by positioning the spectrometer further towards a horizontal scattering angle of 90° with a simultaneous rotation of the cell to keep the field of view towards the spectrometer. However, such a rotation prolongs the penetration length of the incident X-rays, which leads to an increased absorption by the upstream diamond. A rotation of 20° prolongs the penetration length from 500 µm to 532 µm and decreases the incident flux by ~6.6%.[20] Furthermore, the spectrometer could be positioned to the same height as the sample, which would then require a tilting of the analyzer crystals and the detector, to keep both close to the correct scattering angle for the energies required.

5.4 Conclusion

The change of the experimental setup from forward scattering geometry to ~70° horizontal scattering angle resulted in a variety of improvements in terms of accuracy, data quality and efficiency. The energy calibration in the enhanced geometry is significantly improved and shows no deviation compared to the energy calibration using a thin iron foil, which leads to the conclusion that it is close to the achievable optimum.

The spin determination of samples with a high iron content inside a DAC environment can now be carried out on timescales of seconds compared to hours in forward scattering and allows for new options for experiments such as *in situ* laser-heated spin-state imaging. Simultaneously, samples that were previously unable or inefficient to be measured in the previous setup due to their low iron content are now feasible in the enhanced geometry. A further improvement is achieved in terms of VTC spectroscopy, for which the measurement times have reduced to one hour, which can be further reduced to several minutes, if a binning of adjacent detector pixels is applied. Moreover, the SNR has been established as a useful tool to evaluate measurements during the process and may help for a more efficient usage of beamtime, especially for samples with low iron content and long measurement times.

In case of RXES, the measurement times depend on the used monochromator but can be shortened to around 30 minutes for 1s2p RXES with all four crystals and Si(111) monochromator, which allows for *in situ* laser-heated measurements. It has also been shown that 1s3p RXES as well as two-color RXES experiments are feasible with this setup. However, further improvements have to be implemented for a meaningful usage of this technique in experiments at high pressure and temperature conditions. A significant downside of RXES inside a DAC in this geometry is the inevitable effect of self absorption of the sample. As the measurement geometry requires the MD on the upstream side, the spectrometer has to be positioned on the downstream side. Hence, the emission of the sample will always be measured in transmission geometry. This limits the information content of the measurement and, e.g., an analysis of the iron's coordination by integration of the pre-edge intensity[24] is not feasible. Although there are different approaches to suppress this effect, such as the measurement of thinner samples or a measurement position on the rim of the sample at the side of the spectrometer, a remaining self absorption cannot be excluded and furthermore, both approaches lead to a decreased emission intensity.

All in all, the improvements of the setup allow for new experimental opportunities to reveal the electronic structure of iron-bearing compounds at lower mantle conditions. Moreover, the setup is not limited to iron but can be applied for a variety of (transition) metal complexes by exchange of the analyzer crystals and adjustment of von Hámos and detector heights. Also, a simultaneous measurement of different elements is possible if the geometrical requirements are similar enough, analogous to the Fe-Kα and Fe-Kβ measurements.

6 Spin state of tetrairon(III) orthocarbonate and diiron(II) diiron(III) tetracarbonate

6.1 Scientific background

Iron-bearing carbonates are important for the deep carbon cycle.[10] The cycle starts by subducting slabs that transport material from the oceanic crust deep into the Earth. Mineral inclusions in diamonds have verified their stability up to a depth of 700 km,[81,82] below the Earth's transition zone into the lower mantle. Thus, these phases are candidates for the carbon transport in the deep Earth.

In order to understand the stability of carbonates under mantle conditions, numerous high-pressure and high-temperature studies have been conducted for a variety of carbonates. These studies have revealed pressure- and temperature-induced transitions on a structural level and on the electronic states as well as stability conditions of given carbonates and decomposition into different reaction products.[26,30,33–39]

Siderite ($FeCO_3$) as iron-bearing carbonate is an important mineral in the context of the deep Earth. It has been shown, that siderite undergoes a spin transition at ~ 43 GPa, combined with a simultaneous isostructural volume collapse.[33,37,38,83] Recent studies have identified complex new phases with tetrahedrally coordinated carbon as reaction product of siderite at high pressure and high temperature,[22,40,41] namely tetrairon(III) orthocarbonate ($Fe_4^{3+}C_3O_{12}$) and diiron(II) diiron(III) tetracarbonate ($Fe_2^{2+}Fe_2^{3+}C_4O_{13}$). As the carbon in these structures is sp^3-hybridized, they are called sp^3-carbonates in the following. First data on the stability conditions imply that they form at pressures > 50 GPa and temperatures > 1400 K.[41] Although these phases are well understood on a structural level, information on their electronic structure is scarce. In general, three different spin values are possible for each sp^3-carbonate, as both contain two different iron sites. The possibilites are spin values of 2.5 (2.25) or 0.5 (0.25) if both sites of $Fe_4^{3+}C_3O_{12}$ ($Fe_2^{2+}Fe_2^{3+}C_4O_{13}$) are in HS or LS state, respectively. The third possibility is, that the different iron sites are in different spin states, which then results in a total spin value of 1.5 (1.25). Both phases are predicted to incorporate iron in HS state in all iron sites, as the distance between iron and oxygen atoms is longer than for LS iron complexes.[21,34] This is also supported by density functional theory (DFT) based calculations for both sp^3-carbonates.[23,60] Furthermore, it was unclear if the oxidation state in $Fe_4C_4O_{13}$ is sharply separated into ferrous and ferric iron or if there is an intermediate valence state, between Fe^{2+} and Fe^{3+}, due to the similarity of the iron polyhedra. Recent DFT calculations[23] suggest a distinct separation between both polyhedra in ferrous and ferric iron. As both phases contain ferric iron, their presence in the deep Earth may influence the $Fe^{3+}/\sum Fe$ ratio, a balance that is otherwise solely constrained by ferropericlase (FP) and silicate perovskite (SP). The results of this study are published in Albers et al.[23] This work was financially supported by the DFG via STE 1079/4-1 within DFG-FOR2125 (CarboPaT).

6.2 Experimental details

The experiments were conducted using single crystalline $FeCO_3$ as starting material.* The synthesis process is described by Cerantola et al.[37] Each sample was pressurized to its final pressure prior to the heating process, i.e., iron being in the LS state in all samples. After laser heating, the samples were characterized by Raman spectroscopy and XRD. Spin-state imaging, *ex situ* and *in situ* was performed using $K\beta_{1,3}$ XES with the setup described in Chapter 3. Samples A and D were measured in 70° horizontal scattering angle, whereas samples B and C were measured in 0° horizontal scattering angle, which accounts for the difference in data quality. Further details on each sample are listed in Tab. 6.1

Table 6.1: Experimental details for each sample.

sample	cell type	culet / µm	diamonds down / up	pressure medium	laser
A	BX90-RO	200	ST/MD	Argon	Yb:YAG single-sided
B	Plate DAC	200	BA/BA	Argon	CO_2 double-sided
C	BX90-RO	200	BA/ST	Neon	Yb:YAG double-sided
D	BX90-RO	150	ST/BA	Argon	Yb:YAG single-sided

6.3 Laser-heating system

Most of the samples were heated using a portable laser-heating setup,[84] which will be described in the following. The laser heating system was funded via BMBF 05K10PEC. Sample B was heated using the CO_2 laser-heating system of the AG Winkler at University of Frankfurt,[85] which will not be further described here.†

The portable laser-heating system was build in cooperation between University of Potsdam and Technische Universität Dortmund. The setup was originally designed for the use at beamline P01 and subsequently stationed at the University of Potsdam for maintenance and optimization, with the option to set it up quickly at P01 on user demand. It contains a 100 W Yb:YAG fiber-laser with a wavelength of 1070 nm for on-axis and double-sided laser heating. Therefore, the laser beam is split into two parts by a polarizing beam splitter. Each beam can be tuned in intensity by a combination of a motorized phase-shifting plate and a subsequent polarizing beam splitter. Depending on the phase shift, a fraction of the laser is directed into a metal block which functions as a beam dump. The laser is then guided in 90° angle to the X-rays on the upstream and downstream side of the sample. The collimated beam is focused by geoHEAT 60_NIR objectives onto the sample. On the upstream side, the collimated beam is first focused and subsequently redirected by a mirror to be in line with the X-rays. On the downstream side the collimated beam is first redirected by a mirror to be in line with the X-rays and subsequently focused. Sample C was heated with this set of objectives from both sides, whereas in case of samples A and D the geoHEAT 60_NIR objectives were removed and a Mitutoyo M Plan Apo 20x was positioned on the downstream side for one-sided laser heating. The mirror on the upstream

*The samples were synthesized by Stella Chariton and Valerio Cerantola at Bayerisches Geoinstitut.

†The laser heating was supported by Lélia Libon and Georg Spiekermann in Potsdam and Lkhamsuren Bayarjargal in Frankfurt.

side contains a hole of 300 µm in diameter to allow transmission of the incident X-rays without intensity loss. These mirrors on upstream and downstream side can be adjusted by motors to ensure a homogeneous heating from both sides. For temperature measurement during heating, the emitted thermal radiation of the sample is collimated with the same objectives and guided to a spectrometer to analyze its black-body-radiation and calculate its temperature by a Planck fit. The entrance of the spectrometer is covered by a mirror with two holes drilled into it. The mirror allows an observation of the glowing sample during heating and through the two holes, the upstream and downstream temperature of the sample can be measured independently. As basis for the Planck fit, a spectrum of a tungsten filament lamp with a well known temperature was measured prior to the experiment. The lamp itself was calibrated against a radiance standard from Gooch Housego PLC. Fig. 6.1 shows the whole setup with an example of a temperature measurement and the image on the mirror.

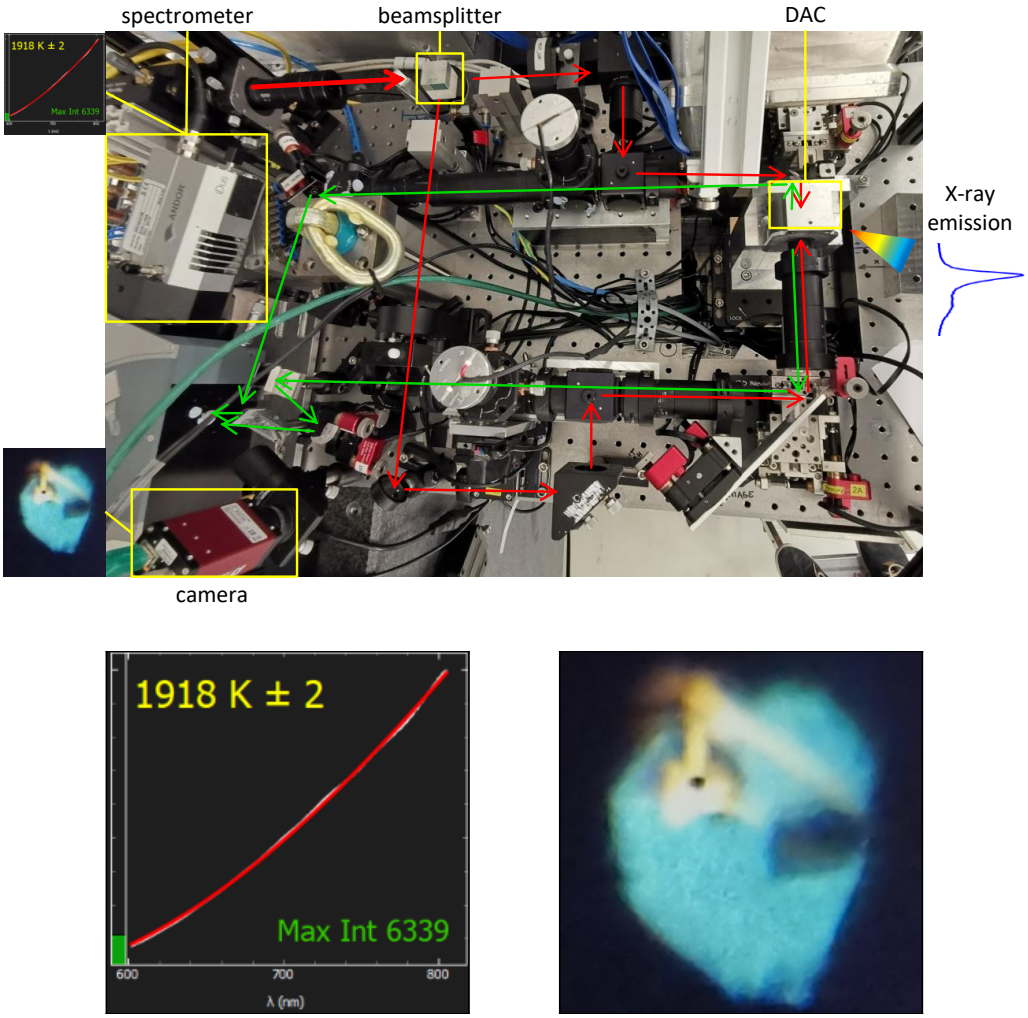

Figure 6.1: Top view of the laser heating setup at P01. The laser path and the optical path for thermal radiation for temperature measurement are indicated by red and green arrows, respectively. The X-ray emission is indicated by the rainbow colored cone. On the left side, an example of the temperature analysis using T-Rax[86] (top) and the camera image of the glowing sample (bottom) are shown. Enlarged views of both images are shown underneath the laser setup.

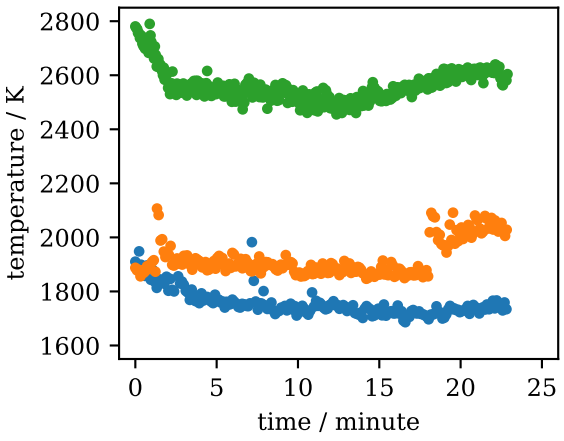

Figure 6.2: Temperature measurements during *in situ* laser heating of sample D for different laser powers.

To keep track of the temperature during heating, a spectrum of the glowing sample was measured every 1 to 4 seconds. The different integration times are based on the different intensities of the glowing samples to obtain a reasonable intensity at low temperatures but avoid saturation of the spectrometer at higher temperatures. Within a heating process, the laser and also the temperature was stable over long measurement times. Fig. 6.2 shows the temperature variations during the *in situ* measurements of sample D. As can be seen, the temperature variation within one measurement is small and varies between 50 K and 70 K standard deviation. However, the uncertainty of each temperature measurement itself is significantly higher than these standard deviations. There is a wide range of possible source for errors in the temperature measurements of a laser-heating experiment such as inaccuracies in the setup, an inaccurately calibrated spectrometer or reference spectrum. Besides this, a possible source of error that is not caused by handling of the setup is the chromatic aberration of the used lenses, which leads to a displacement of different wavelength on the spectrometer. However, this effect can be reduced either by the use of apochromatic lenses or the combination of apochromatic lenses with an iris in front of it, which, on the down side, also reduces the numerical aperture and results in a reduced image quality. Furthermore, the temperature measured with the spectrometer is the temperature at the surface of the sample, but, especially in case of single-sided laser heating, the laser causes an axial temperature gradient within the sample that is not reflected in the temperature measurement. Additionally, there is also a temperature gradient orthogonal to the laser axis and a large range of temperatures may be probed, depending on the spatial resolution of the incident X-rays. Consequently, an error was estimated of 200 K for double-sided and 300 K for one-sided laser heating. A more detailed overview of laser-heating in general can be found in Anzellini et al.[18] and the references therein.

6.4 Characterization of samples after heating

6.4.1 Raman spectroscopy

Optical Raman spectroscopy is an experimental technique to determine vibrational modes of a sample by exciting it via a laser to a virtual state and detecting the scattered photons afterwards.[87] Fig. 6.3 shows the principle of three possible cases. Elastic scattering of the photons results in Rayleigh scattering and results in no energy shift, whereas Stokes and anti-Stokes scattering result in an energy decrease or increase, respectively. As the ground state has a higher population than the excited states, the probability for Stokes scattering is higher than for anti-Stokes scattering. Raman spectroscopy is sensitive to changes in the geometric structure of a sample that affect their polarizability and generally a well available technique, which is relatively easy to apply, even for challenging sample environments such as DACs.[88,89] Thus, it was chosen to verify the decomposition of the starting material.

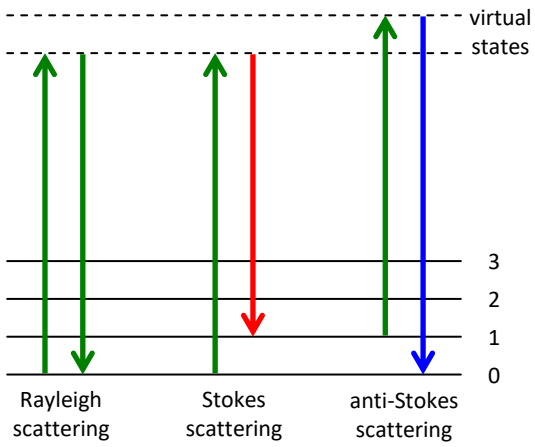

Figure 6.3: Principle of Rayleigh, Stokes and anti-Stokes scattering.

All samples in this chapter were characterized after laser heating by optical Raman spectroscopy imaging at GFZ with a laser of 532 nm wavelength and a spot size of 2 µm. Raman bands were measured in a wavenumber range from 100 cm^{-1} to 1300 cm^{-1}. This technique is a fast and easy way to detect changes in the sample, particularly the decomposition of $FeCO_3$ can be verified. At pressures below the spin transition, $FeCO_3$ shows four Raman bands in the observed wavenumber range, the T, L, ν_4 and ν_1 mode.[90] However, at such high pressure as in this study, only three Raman bands are detectable at around 630 cm^{-1}, 915 cm^{-1} and 1200 cm^{-1}, the L, ν_4 and ν_1 mode, respectively (see Fig. 6.4 a)).[91] Integration of its most intense mode ν_1 provides a good overview on the spatial distribution of $FeCO_3$ in the sample. Due to the heating process, the intensity of the ν_1-mode significantly decreased in the vicinity of the heating spot, which indicates a decomposition. Furthermore, in some parts of the samples, new low-wavenumber Raman bands appeared in a wavenumber range of 100 cm^{-1} to 350 cm^{-1}. An example spectrum is shown in Fig. 6.4 b). To estimate its amount and spatial distribution within the sample, the most intense mode at around 230 cm^{-1} was integrated and transferred into a map.

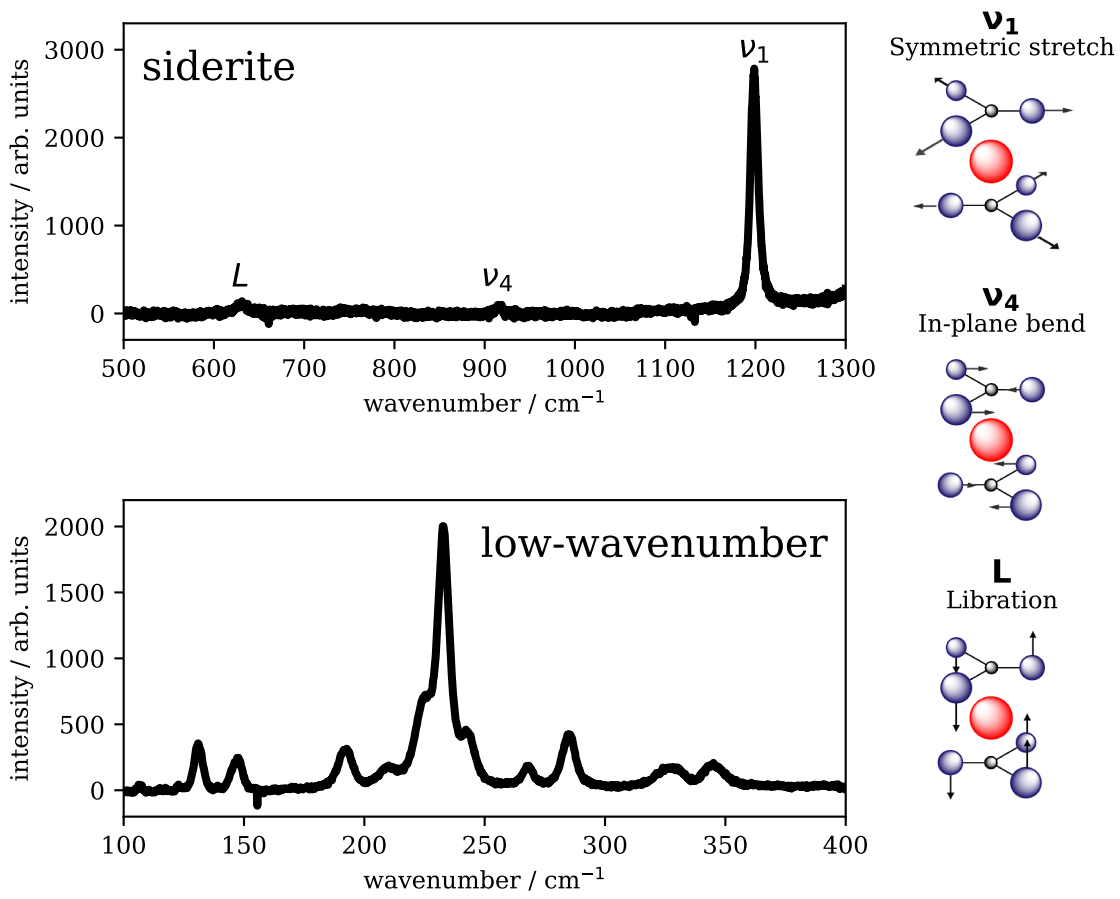

Figure 6.4: Example spectra of high pressure $FeCO_3$ (**top**) and the new low-wavenumber Raman bands (**bottom**). Known Raman modes of $FeCO_3$ are labeled modeled on the right side (modified after Boulard et al.[92]) with permission by Springer Nature.

6.4.2 X-ray diffraction

XRD is an X-ray technique to gain information on the structure of samples. In such an experiment, usually monochromatic X-rays interact with the electrons of the samples crystal structure and are elastically scattered by the electrons of the sample. The theory of XRD is widely known and and can be found in the literature, e.g., in Kopitzki and Herzog.[93] In the following a short outline of the theory will be presented.
The incident X-rays are interacting with the electrons of the sample. The incident and scattered photons can be described by their wave vectors $\mathbf{k}$ and $\mathbf{k}'$, respectively. In case of elastic scattering is follows that $|\mathbf{k}| = |\mathbf{k}'|$ The wave vector transfer is defined as $\mathbf{k}' - \mathbf{k} = \mathbf{q}$ and is depending on the scattering angle 2Θ

$$|\mathbf{q}| = \frac{4\pi}{\lambda} \sin\Theta \tag{6.1}$$

The amplitude of the scattered photons in an XRD experiment is a summation of the contributions of all participating atoms in the scattering process

$$A(\mathbf{k}) = \sum_n f_n(\mathbf{q}) e^{i\mathbf{q}\cdot\mathbf{r}_n}. \tag{6.2}$$

Here, $\mathbf{r}_n$ and f_n represent all atom positions and their regarding atomic form factor. In case of an XRD experiment, the measurable instance is the intensity, which is defined as the square of the absolute amplitude

$$I(\mathbf{q}) = |A(\mathbf{q})|^2 \tag{6.3}$$

On crystallized samples, symmetry properties can be exploited and the crystal can be defined by its unit cell and its lattice. Hence, each atom position within the crystal can be described by its lattice translation vector $\mathbf{r}_j = a\mathbf{x} + b\mathbf{y} + c\mathbf{z}$ and its basis δ_k, i.e., its position within the unit cell

$$\mathbf{r}_{jk} = \mathbf{r}_j + \delta_k \tag{6.4}$$

with $\mathbf{x}$, $\mathbf{y}$ and $\mathbf{z}$ as unit vector of the lattice and a, b and c as integers. This simplifies Eq. 6.2 to

$$A(\mathbf{q}) \propto S(\mathbf{q}) \cdot F(\mathbf{q}). \tag{6.5}$$

with the structure factor

$$S(\mathbf{q}) = \sum_{k}^{cell} f_k(\mathbf{q}) e^{i\mathbf{q}\cdot\delta_k} \tag{6.6}$$

and the lattice sum

$$F(\mathbf{q}) = \sum_{j} e^{i\mathbf{q}\cdot\mathbf{r}_j}. \tag{6.7}$$

$F(\mathbf{q})$ (and consequently also $A(\mathbf{q})$) only provides a contribution for $\mathbf{q} \cdot \mathbf{r}_j = 2\pi \cdot m$ with m as an integer. As a consequence of this, the Laue equation

$$\mathbf{q} \stackrel{!}{=} \mathbf{G}_{hkl} \tag{6.8}$$

follows with $\mathbf{G}_{hkl}$ as the reciprocal lattice and h, k and l as the Miller indices.

For the samples studied in this chapter, XRD imaging was performed at beamline P02.2 of PETRA III (DESY) with a spatial resolution of 2 µm and an incident energy of 42.7 keV, in order to obtain a detailed phase distribution of the whole sample after laser heating. The beamline uses a PerkinElmer XRD 1621 detector with a pixel size of $200 \times 200\,\mu m^2$, which was positioned at a distance between 400 mm and 500 mm downstream of the sample, varying between different experiments. The detector was calibrated using CeO_2(NIST standard647b). Example diffraction patterns of $FeCO_3$, $Fe_4C_3O_{12}$ and $Fe_4C_4O_{13}$, measured on different positions of sample C, are shown in Fig. 6.5 along with a cut from the detector image. To quantify the occurrence of each phase, a 2-Θ-range was selected which only contains diffraction peaks of a single phase and its intensity was integrated. However, as no powder average was measured, this method cannot verify the exact amount of each phase, but provides a good overview of the lateral phase distribution of the sample.

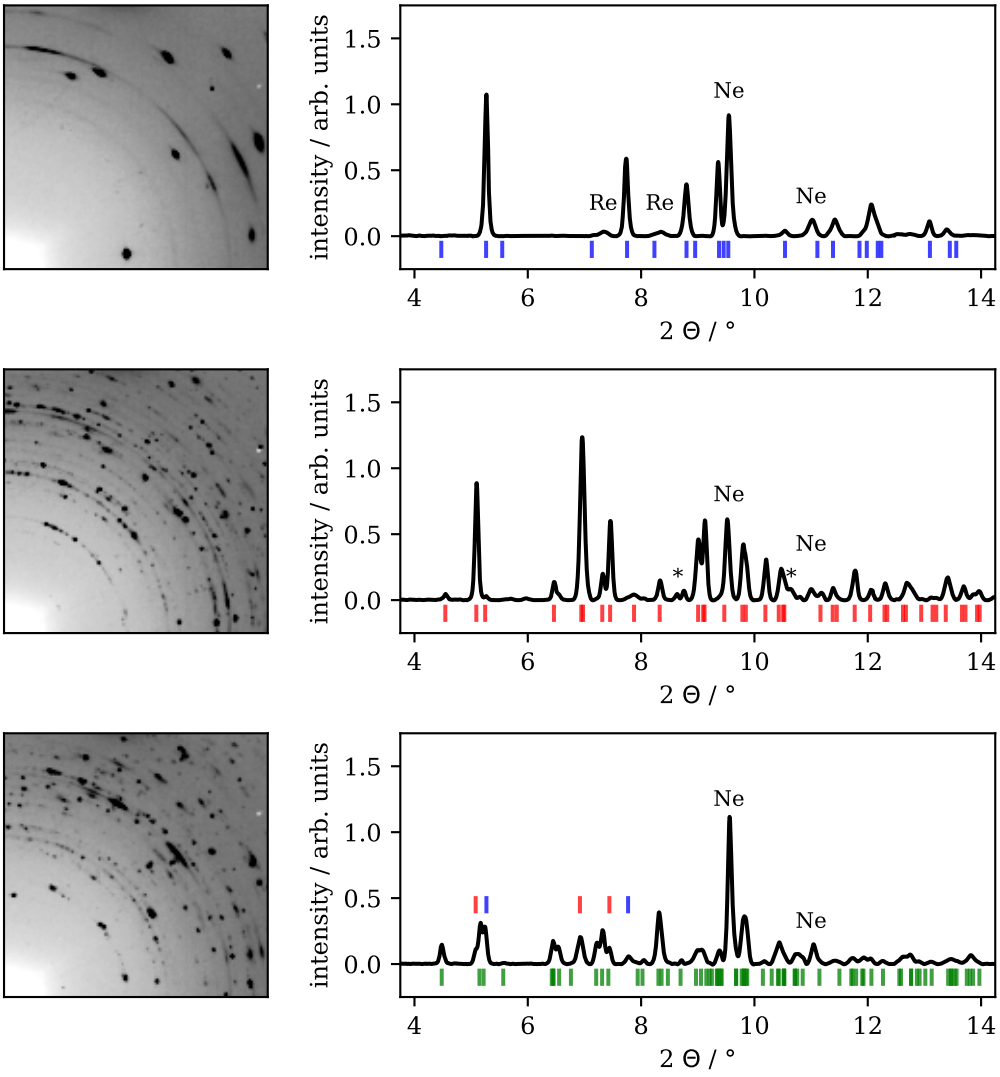

Figure 6.5: Detector images (left) and corresponding integrated diffraction pattern (right) of $FeCO_3$ (top, blue), $Fe_4C_3O_{12}$ (middle, red) and $Fe_4C_4O_{13}$ (bottom, green). Underneath each pattern all reflexes with an intensity of more than 2% are indicated by the colored lines. Peaks that cannot be assigned to a certain phase are marked by an asterisk.

6.5 Experimental results

In the following, the results on laser heated siderite samples at high pressure will be presented for four samples in total. Each sample shows a different phase distribution and thus provides complementary information for the analysis on the electronic structure of iron-bearing sp^3-carbonates. The phase distribution is analyzed by optical Raman spectroscopy as well as XRD after temperature quenching and listed in Tab. 6.2 for all measurements. The spin state is analyzed by XES for all samples after temperature quenching and *in situ* during heating for sample D. The spin state of $Fe_4C_3O_{12}$ will be determined by samples A and C, whereas sample B and C provide information about $Fe_4C_4O_{13}$. Sample D will then extend the information from temperature quenched samples to *in situ* conditions up to 2600 K.

Table 6.2: List of sample conditions and dominant reaction products. Gray phases might not be present at given conditions. The phase occurrence during *in situ* heating is an educated guess and will be elaborated in the discussion.

sample	pressure / GPa	temperature / K	reaction product
A	80 ± 2	2700 ± 300	$Fe_4C_3O_{12}$
B	83 ± 2	3000 ± 200	$Fe_4C_4O_{13}$
C	85 ± 2	2300 ± 200	$Fe_4C_3O_{12}$, $Fe_4C_4O_{13}$
		2800 ± 200	$Fe_4C_3O_{12}$, $Fe_4C_4O_{13}$
D	82 ± 2	1700 ± 300 (*in situ*)	$Fe_4C_3O_{12}$, $Fe_4C_4O_{13}$
		2000 ± 300 (*in situ*)	$Fe_4C_3O_{12}$, $Fe_4C_4O_{13}$
		2600 ± 300 (*in situ*)	$Fe_4C_3O_{12}$, $Fe_4C_4O_{13}$
		3000 ± 300	$Fe_4C_3O_{12}$, $Fe_4C_4O_{13}$

A Tetrairon(III) orthocarbonate

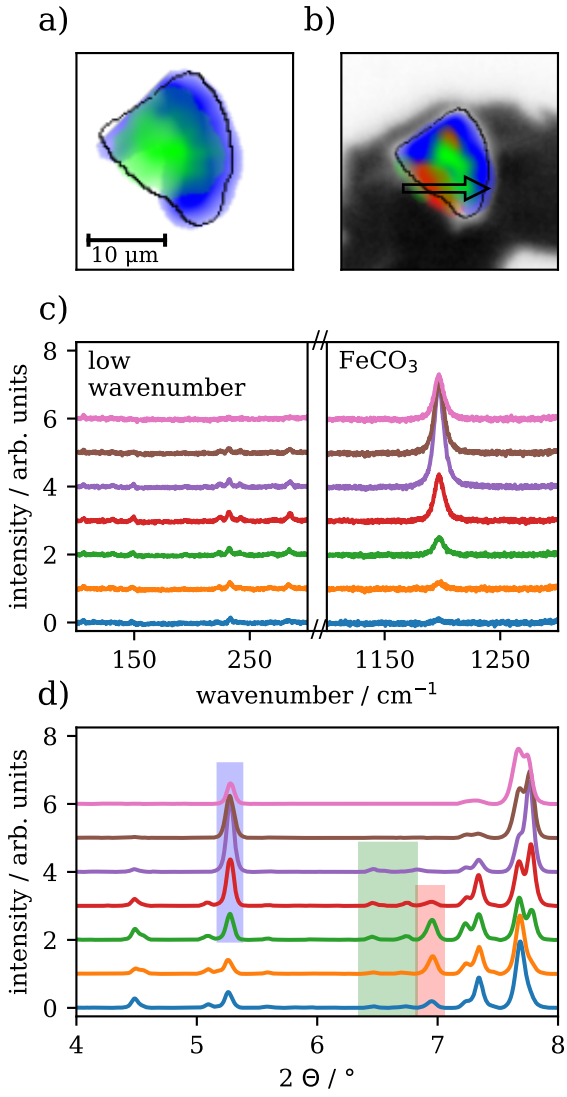

Figure 6.6: Raman spectroscopy (a) and XRD imaging (b) of sample A. The $FeCO_3$ contribution is shown in blue in both images, whereas the $Fe_4C_4O_{13}$ contribution, determined via XRD imaging is shown in green. The occurrence of the low-wavenumber bands in a) is visualized in green as well. The red area indicates $Fe_4C_3O_{12}$. Raman spectra and XRD pattern for the traverse indicated by the black arrow in (b) are shown in (c) and (d), respectively (modified after Albers et al.[23]).

Sample A was laser-heated to 2800 K using the Yb:YAG-laser heating system[84] and all measurements were performed after temperature quenching at 80 GPa. The phase distribution is visualized in Fig. 6.6. Raman spectroscopy imaging in a) shows a significant amount of unreacted siderite (blue) on the right and upper side of the sample. Furthermore, starting from its center to the sample's left side, low-wavenumber bands (green) are present. The $FeCO_3$ distribution could be verified by XRD imaging with the results presented in b). In the sample area where low-wavenumber bands appear, both sp^3-carbontes are present (left side of the sample) with the contribution of $Fe_4C_3O_{12}$ in red and $Fe_4C_4O_{13}$ in green. Fig. 6.6 c) and d) display a traverse across the sample in terms of Raman and XRD data, respectively. The Raman spectra show first an onset of the low-wavenumber bands without a significant contribution of the $FeCO_3$-band. Afterwards, both phases are simultaneously present and eventually the low-wavenumber bands vanish while the $FeCO_3$-band is still present. XRD data from the same traverse show first an onset of both sp^3-carbonates without a significant contribution of $FeCO_3$ and a subsequent vanishing of both sp^3-carbonates with the onset of the $FeCO_3$ contribution. The overlap between the spatial distributions of $FeCO_3$ and $Fe_4C_4O_{13}$ is larger than for $Fe_4C_3O_{12}$. However, the total amount of $Fe_4C_4O_{13}$ is estimated to be smaller by a factor of 10 compared to $Fe_4C_3O_{12}$, indicated by the integrated intensities of the XRD pattern, although an exact determination of the phase composition is not possible as no powder average was measured. The shaded areas in Fig. 6.6 d) indicate the Bragg reflections used to determine the distribution of each phase. The distribution of $FeCO_3$ is based on single crystal peaks in the detector image. Thus, its contribution is indicated only on the right part of the sample, although the integrated pattern from the left side show a contribution in the same 2-Θ-range.

XES measurements were performed on a 5 x 5 grid with a step size of 5 µm and the results are presented in Fig. 6.7. Single $K\beta_{1,3}$ emission spectra are shown in a) with their corresponding IAD values in b) for the same traverse discussed before. For comparison the M_1 value is shown with the right y-axis as scale. The data show a significant HS contribution on the left side of the sample, developing to a mostly LS value on the right side of the sample. Within the limits of this analysis the spin values on the right side are considered as completely in LS state. Both spin values at the edge of the sample are based on a low data quality due to low emission intensity. Thus, the results of the IAD analysis of these points may be inaccurate which shows especially for the LS spectrum on the right side. All in all, IAD and ΔM_1 analysis are in good agreement for spectra with an SNR > 100. Fig. 6.7 c) (left) extends the information from b) to the whole sample with its contour in black. The positions were determined by overlapping the COG positions of XES and XRD intensities. The results are shown in Fig. A.1 in the appendix. The IAD map visualizes the HS and LS contribution on the left and right side, respectively. The HS regime correlates with the distribution of the sp^3-carbonates. The fact that the highest spin values are located next to the sample is based on the spot size of 8 x 8 µm^2, indicated by the gray circles, and thus a non-negligible amount of unreacted $FeCO_3$ in the spectra when scanning the sample. If the COG of the incident X-rays beam is located next to the sample, only its tail is interacting with the sample and thus mostly sp^3-carbonate is probed. To underline this, a theoretical spin map is calculated based on the XRD results and is visualized in Fig. 6.7 c) on the right side, assuming the spatial resolution of the XES experiment. As the sample characterization indicates a significantly less amount of $Fe_4C_4O_{13}$ in the sample, only the $Fe_4C_3O_{12}$ contribution was considered. The spin state of $Fe_4C_3O_{12}$ was set to HS state, in line with the literature[22,60] and the spin state

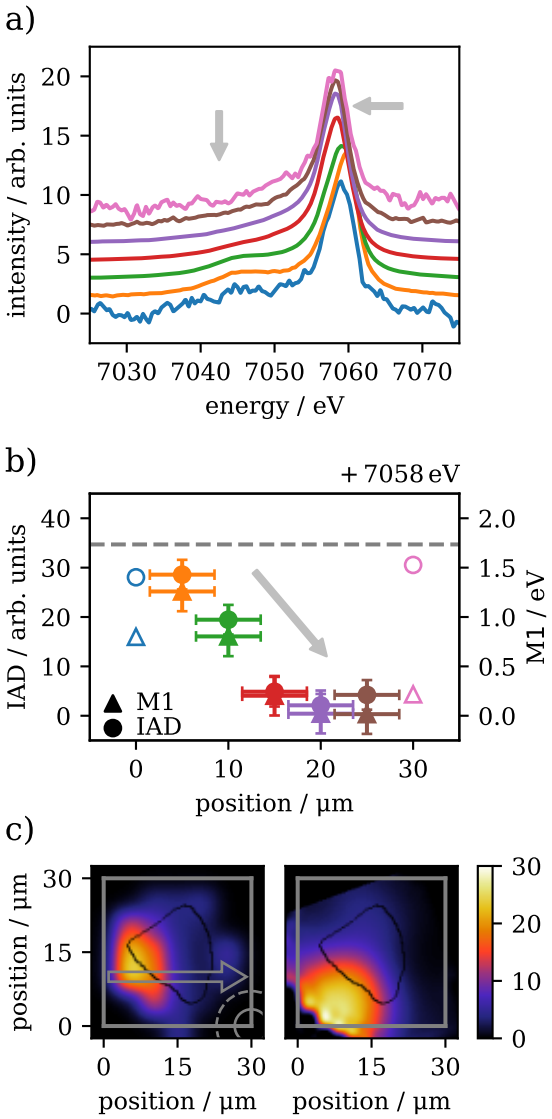

Figure 6.7: a) $K\beta_{1,3}$ XES spectra of sample A for the same traverse shown in Fig. 6.6 with their IAD results and M_1 position (offset by 7058 eV) in b). Open symbols represent spectra with a SNR < 100. The difference spectra to the LS reference are shown in Fig. A.2 in the appendix. The gray arrows in a) and b) indicate changes while following the gray arrow in c). The color code matches the spectra in a). The gray dashed line in b) indicates the IAD value between a LS and HS $FeCO_3$ reference. c) (left) Resulting IAD map for the whole sample. The gray circles indicate the beam size for intensities of 50 % (solid) and 5 % (dashed). (right) Calculated spin value map based on contributions of $FeCO_3$ and $Fe_4C_3O_{12}$ as identified by XRD (see text for details, modified after Albers et al.[23]).

of $FeCO_3$ was set to LS state. As the exact amount of each phase could not be determined unambiguously, the contribution of $Fe_4C_3O_{12}$ was arbitrarily scaled with a factor of 3 compared to $FeCO_3$. The results are in mutually agreement with that of the spin-state imaging by XES. Thus, the spin state of iron of temperature quenched $Fe_4C_3O_{12}$ can be verified as HS state. The spin state of $Fe_4C_4O_{13}$ could not be determined in this sample and will be discussed in the following along with the occurrence of low-wavenumber Raman bands. IAD and ΔM_1 analysis are in good agreement as seen for the traverse in Fig. 6.7 b) as well as for the whole map. Fig. 6.8 visualizes all spectra measured at their respective position on the map with the spin state calculated by the ΔM_1 analysis overlapping with the spectra. Spectra with an SNR < 100 are plotted in gray and their spin value was set to 0 as the data quality was not sufficient for a dedicated analysis.

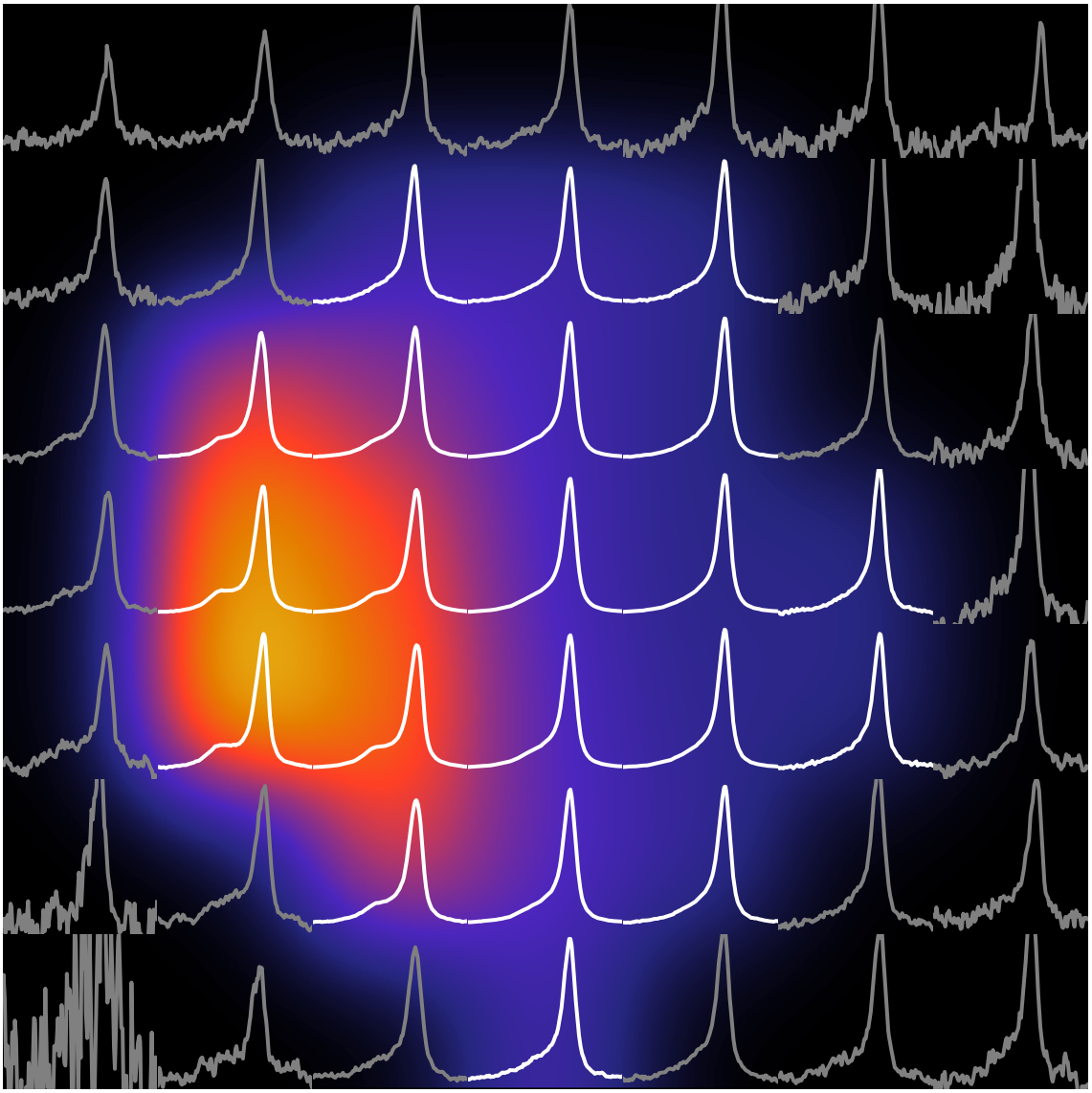

Figure 6.8: Representation of all $K\beta_{1,3}$ spectra measured during spin-state imaging at the position of measurement, along with the spin-state map analyzed via ΔM_1. All spectra are normalized to the same area and each spectrum is represented on the same y-scale. Spectra with an SNR < 100 are shown in gray and their spin state is not analyzed but set to 0.

B Diiron(II) diiron(III) tetracarbonate

Sample B was heated by a CO_2-laser to 3000 K. Fig. 6.9 a) and b) show results of Raman and XRD imaging after temperature quenching at 83 GPa, respectively. Raman spectroscopy verifies low-wavenumber bands for the majority of the sample with a small contribution of $FeCO_3$ in the lower part. XRD imaging verifies the occurrence of $Fe_4C_4O_{13}$ in the whole sample. Due to the vicinity of Bragg reflections and the presumably low amount of $FeCO_3$ in the sample, no single crystal reflexes could be identified unambiguously and the $FeCO_3$ signal could not be extracted by XRD. Furthermore, contributions of iron oxides, as predicted by Cerantola et al.,[22] were not found but could also not be excluded definitely due to complexity of Bragg reflections. In addition, Raman spectroscopy was performed for the most common iron oxides FeO, Fe_2O_3 and Fe_3O_4 at 75 GPa in order to interpret the low-wavenumber Raman bands. No Raman bands could be observed in the wavenumber range between 100 cm^{-1} and 1300 cm^{-1}. Thus, these phases can be excluded as possible cause. However, the appearance of the low-wavenumber bands is strongly correlated to the appearance of $Fe_4C_4O_{13}$ in the XRD measurements, which indicates that the Raman bands either occur from the $Fe_4C_4O_{13}$ directly or indirectly due to a byproduct in the synthesis process.

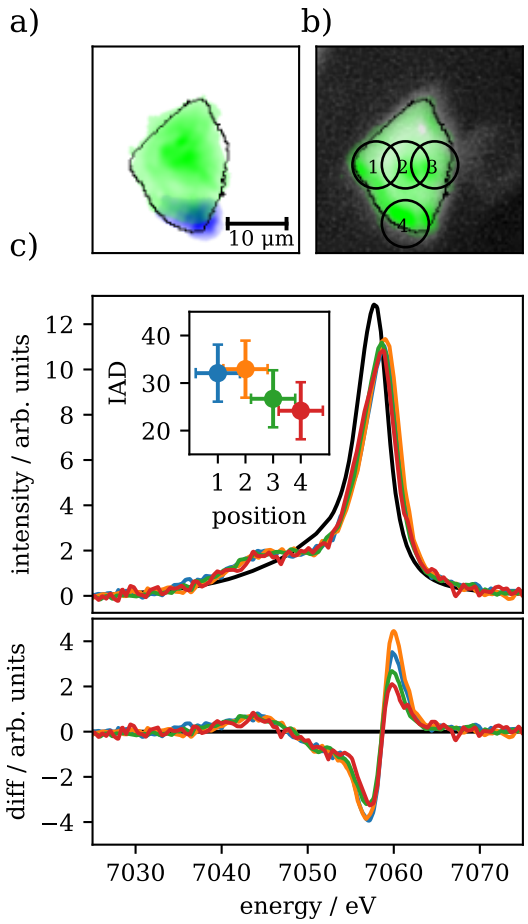

Figure 6.9: Phase characterization by Raman spectroscopy a) and XRD b) imaging for sample B. The $FeCO_3$ contribution is shown in blue in both images, whereas the $Fe_4C_4O_{13}$ contribution, determined via XRD imaging is shown in green. The occurrence of the low-wavenumber bands in a) is visualized in green as well. c) $K\beta_{1,3}$ XES spectra with the difference to the LS reference underneath for 4 positions on the sample indicated by the circles in b). The LS reference is shown in black as a guide to the eye. The inset shows the IAD results for all 4 positions (modified after Albers et al.[23]).

XES measurements were performed at 4 different positions on the sample and are shown in Fig. 6.9 c) along with the difference to the LS reference underneath. As the data acquisition was performed in forward scattering geometry with BA diamonds on the upstream and downstream side, the data quality is significantly lower compared to the previously presented sample, despite a substantially increased acquisition time. Nevertheless, all spectra indisputably contain a significant contribution of HS iron, which indicates that the iron in both coordinations in $Fe_4C_4O_{13}$ is in HS state. Furthermore, variations between the XES spectra can be spotted when focusing on the difference to the LS reference. This is reflected in the results of IAD analysis, visualized in the inset of Fig. 6.9 c). Positions 1 and 2 show a higher IAD value than positions 3 and 4, which might be attributed to unreacted $FeCO_3$ in the sample, at

least for the spin value of position 4. However, these variations have to be interpreted carefully due to the low SNR of all spectra. Despite the challenging data analysis, the results clearly verify $Fe_4C_4O_{13}$ with iron in HS state in both coordinations.

C Tetrairon(III) orthocarbonate and diiron(II) diiron(III) tetracarbonate

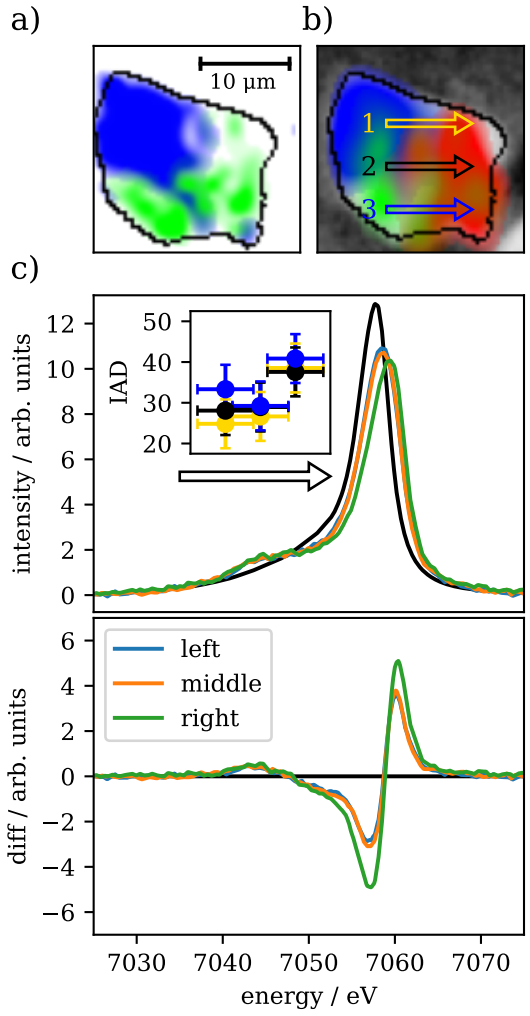

Figure 6.10: Phase characterization by Raman spectroscopy a) and XRD b) imaging for sample C. The colors correspond to the low-wavenumber bands and $Fe_4C_4O_{13}$ in green for Raman spectroscopy and XRD, respectively. The $FeCO_3$ contribution is shown in blue in both images, whereas the red area corresponds to $Fe_4C_3O_{12}$. c) $K\beta_{1,3}$ XES spectra (top) and difference to the black LS reference (bottom) for line 1 across the sample as indicated in b). The LS reference is shown in black as guide to the eye. The inset shows the IAD results for lines 1, 2 and 3 with matching colors (yellow, black, blue, modified after Albers et al.[23]).

Sample C was laser heated two times using the Yb:YAG-laser heating system. In the first heating process the sample was heated to 2300 K and in the second process to 2800 K. Raman spectroscopy in Fig. 6.10 a) shows remaining unreacted $FeCO_3$ in the upper left part and low-wavenumber bands in the lower and the right part of the sample after temperature quenching at 85 GPa. XRD imaging in Fig. 6.10 b) shows a clear spatial separation of $FeCO_3$ and both sp^3-carbonates, with little overlap in the central part. The $FeCO_3$ contribution correlates with the Raman imaging results. Contributions of $Fe_4C_3O_{12}$ and $Fe_4C_4O_{13}$ are located on the right and lower part of the sample, respectively. The low-wavenumber bands appear exclusively in the sample area where XRD verifies $Fe_4C_4O_{13}$.

XES imaging was performed on a 3 x 3 grid with 5 µm step size in between measurements. The experimental geometry was in forward scattering with a diamond setup of ST and BA on the upstream and downstream side, respectively, which causes the lower data quality compared to samples A and D. Fig. 6.10 c) shows $K\beta_{1,3}$ spectra for line 1 (yellow) as indicated in b), with the difference to the LS reference in the plot below. Corresponding IAD values are shown in the inset of c). The results are in good agreement with the previously reported samples and show in general two directions of spin increase. First, from left to right, the change from probing mainly $FeCO_3$ to probing mainly $Fe_4C_3O_{12}$ is accompanied by a significant increase in spin value, at least for lines 1 and 2. The second increase in spin value occurs from the upper part to the lower part of the sample and is more complicated and not as straight forward as the first one. However, all spin values of line 3 are higher than for line 1,

which is most significant for the most left points and occurs due to the change from probing mainly $FeCO_3$ to probing mainly $Fe_4C_4O_{13}$.
The phase distribution of sample C may occur due to the two-fold heating process. Based on the results by Cerantola et al.,[22] $Fe_4C_3O_{12}$ is forming at lower temperatures than $Fe_4C_4O_{13}$ which could also be the case for this sample. This would imply that the first heating process to 2300 K was located on the right part of the sample, whereas the second heating process to 2800 K was located on the lower part of the sample. These findings are in accordance with the results of sample B that was heated to even higher temperatures of 3000 K and only contains $Fe_4C_4O_{13}$ and no $Fe_3C_4O_{12}$. However, as the stability regions of both sp^3-carbonates are not well established and also the exact positions of both heating spots are not exactly known, this conjecture is only speculative. Conclusions on the spin state, on the other hand, are well founded and in accordance with both samples presented previously. Thus, this sample verifies again iron in both sp^3-carbonates being in HS state.

D In situ measurements

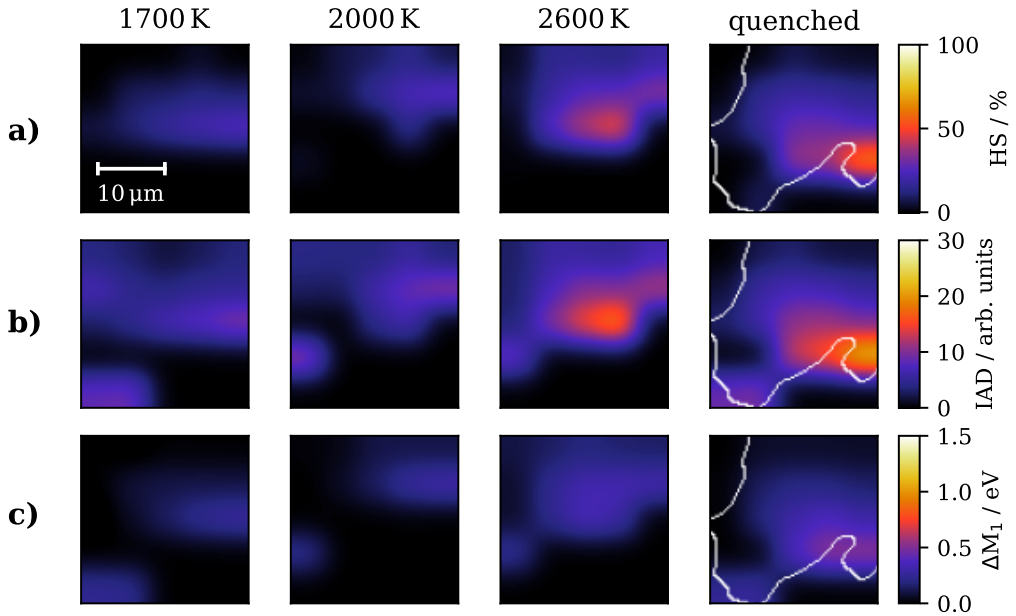

Figure 6.11: Spin-state imaging results of sample D for different temperatures measured *in situ* during heating and after temperature quenching. The phase distribution was analyzed after temperature quenching by Raman and XRD imaging. The spin maps were calculated using linear combination of HS and LS references (a), IAD (b) and ΔM_1 (c) analyses. As HS reference for the compositional fit a spectrum of sample A was used (orange spectrum in Fig. 6.7) and for ΔM_1 analysis the spectrum before heating was used.† The different maps are not overlapping due to movement of the sample and holder by thermal expansion and compensatory movements. Thus, the rim of the sample is indicated only in the spin maps after temperature quenching. The scale in the top left image is valid for all maps (modified after Albers et al.[23]).

†Between measurements of the *in situ* maps and the quenched map, the cell was removed from the beamline. Thus, the map after temperature quenching was calculated with a different calibration and showed a small offset in the energy positions and 0.2 eV were added to the quenched map, to align it with the other measurements.

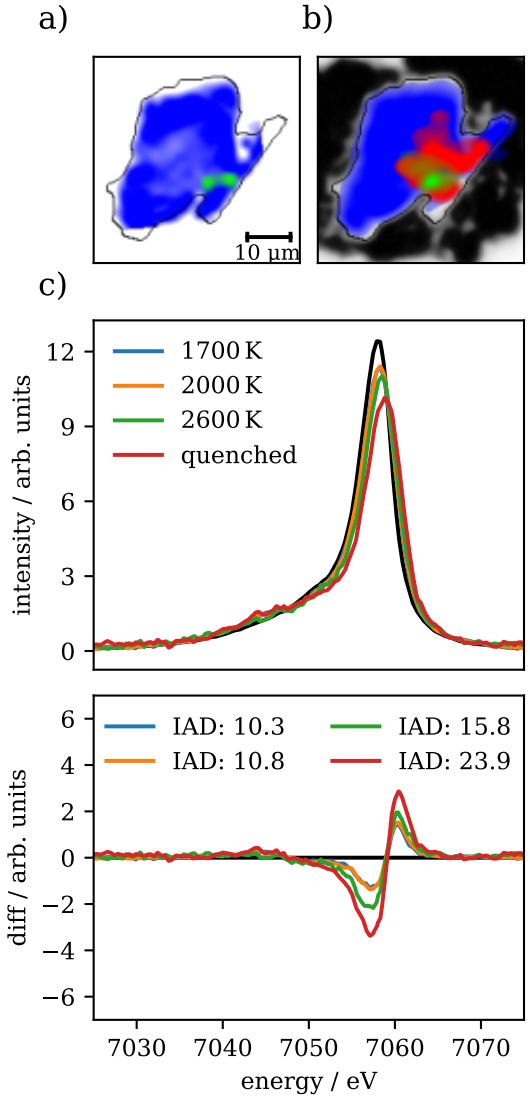

Figure 6.12: Phase characterization by Raman spectroscopy a) and XRD b) imaging for sample D. The colors correspond to the low-wavenumber bands and $Fe_4C_4O_{13}$ in green for Raman spectroscopy and XRD, respectively. The $FeCO_3$ contribution is shown in blue in both images, whereas red indicates $Fe_4C_3O_{12}$. c) $K\beta_{1,3}$ XES spectra (top) and difference to the LS reference (bottom) for spectra with a large HS contribution in the vicinity of the heated area for the different temperatures and after temperature quenching. Furthermore, the LS reference is shown in black as guide to the eye (modified after Albers et al.[23]).

In sample D the results of the previously temperature-quenched samples are extended to *in situ* conditions at high temperature. The sample was heated in several steps with increasing laser power between 1700 K and 2600 K. During heating, XES maps were measured on a 5 x 5 grid with 5 µm step size and 1 minute integration time per spectrum. After temperature quenching, the sample was measured again. The corresponding spin-state imaging results based on three different analysis techniques are shown in Fig. 6.11 for all temperatures during *in situ* heating and after temperature quenching. All spectra are shown in Fig. A.3. To ensure stable results, only spectra with an SNR < 100 were taken into account. As LS reference a spectrum of the sample measured directly before switching on the laser at 82 GPa was used for all analyses. Additionally, a spectrum of sample A (orange spectrum in Fig. 6.7) was used as HS reference for the compositional fit analysis by linear combination of HS and LS references. Despite some variations, all analysis techniques show the same results for the different measurements. The position of the HS area is shifting between the different maps, which is based on the heating process and a slight shift of the cell due to thermal expansion of the cell holder. Thus, the positions of sample and laser had to be adjusted in between each spin-state map and the maps do not necessarily represent identical positions in the cell. Nevertheless, all maps screen a similar part of the sample, which is shown by the distribution of the HS containing area. The temperature quenched map was measured after the cell was cooled down completely and the rim of the sample is indicated in white. Within these maps a continuous trend is detectable as the total area containing HS iron is increasing with temperature, which is based on two effects. First, slight movements of the sample position enlarge the heated area and thus an increase the HS contribution. Second, as the laser power is increased, the spot size, with a temperature high enough to induce a reaction, is increasing. Furthermore, the highest spin value of each map is also rising with increasing temperature, which is shown in Fig. 6.12 c) and is also attributed to an increased amount of reacted sample.

Characterization of the sample was performed after temperature quenching at 82 GPa and the results are presented in Fig. 6.12. The Raman spectroscopy imaging in a) was performed on the unheated side of the sample and shows unreacted $FeCO_3$ in the complete sample, overlapping with a small contribution of low-wavenumber bands on the right side. As Raman spectroscopy is surface sensitive for opaque samples, the resulting distribution of $Fe_4C_4O_{13}$ might be incomplete and the amount of $FeCO_3$ might be overestimated. XRD mapping in b) confirms the distribution of $FeCO_3$ in the complete map. Moreover, the small contribution of low-wavenumber Raman bands is again overlapping with the position of $Fe_4C_4O_{13}$ detected by XRD mapping. $Fe_4C_3O_{12}$ can be found in the same area as $Fe_4C_4O_{13}$ but with a significantly higher contribution. Comparison with the spin-state map after temperature quenching shows a good overlap with the spatial distribution of both sp^3-carbonates. Based on these results and along with the previously presented samples, both sp^3-carbonates can be verified in HS state under pressure and temperature conditions of the Earth's lower mantle and after temperature quenching. The fact that the spin values of this sample are relatively low compared to the other ones is due to a substantial amount of unreacted $FeCO_3$ in the sample as verified by the Raman and XRD imaging. Hence, the $K\beta_{1,3}$ spectra are based on a mixture of $FeCO_3$ and (primarily) $Fe_4C_3O_{12}$ with changing proportions. The results indicate that in the beginning of the heating process $Fe_4C_3O_{12}$ is forming, which reacts only at the highest temperatures to $Fe_4C_4O_{13}$ in the center of the heating spot. This is in accordance with the thermodynamic conditions published in the literature[22,94] and in agreement with samples B and C.

6.6 Discussion

The results of all four presented samples are consistent within each other and show complementary information for each sample. Combination of both characterization techniques, i.e., XRD and Raman imaging, shows a convincing overlap for $FeCO_3$ and the distribution of the low-wavenumber bands is correlating with the occurrence of $Fe_4C_4O_{13}$ for all samples with a mutual agreement between both techniques. From this correlation, the

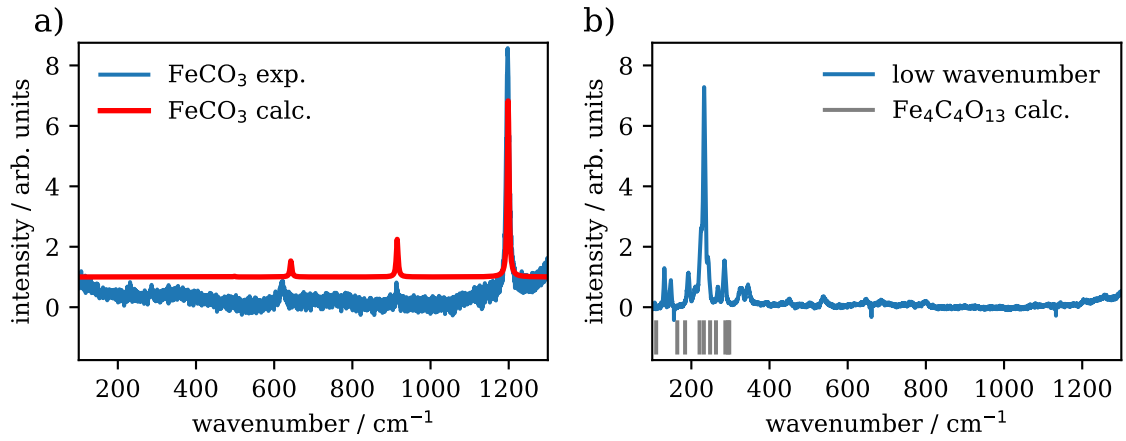

Figure 6.13: a) Experimental and calculated Raman spectra of $FeCO_3$ at 80 GPa. **b)** Low-wavenumber Raman bands along with a selection of Raman active modes of $Fe_4C_4O_{13}$, calculated by Prof. Dr. Björn Winkler, to highlight the differences to the Raman spectrum of LS $FeCO_3$ (modified after Albers et al.[23]).

low-wavenumber bands can be assigned either to $Fe_4C_4O_{13}$ or another phase emerging during the reaction. DFT calculations, performed by Prof. Dr. Björn Winkler of the University of Frankfurt (published in[23]), show several Raman active modes for $Fe_4C_4O_{13}$ at 80 GPa in the wavenumber region between 100 cm^{-1} and 350 cm^{-1} (see Fig. 6.13). Hence, the low-wavenumber Raman bands are a product of $Fe_4C_4O_{13}$, although a determination of the peak intensity was not possible.

The combination of Raman and XRD imaging as characterization methods provides a detailed spatial phase distribution with consistent results between both methods. Especially Raman spectroscopy imaging is an easy but useful tool to determine the decomposition of $FeCO_3$ due to laser heating. However, the verification of newly formed phases requires Raman active bands. The low-wavenumber bands are corresponding to the formation of $Fe_4C_4O_{13}$, whereas $Fe_4C_3O_{12}$ shows no sign of Raman bands in the measured wavenumber range and is thus probably not Raman active. Furthermore, Raman spectroscopy is a surface sensitive method for opaque samples like $FeCO_3$ at high pressures as shown for sample D and its results depend on the samples' orientation, especially if one-sided laser heating was used. Hence, a detailed phase distribution by XRD imaging is indispensable to obtain meaningful results, with the downside of a lower accessibility due to the experimental requirements of highly focused synchrotron radiation.

The phase characterization verifies different phase distributions for all samples. Sample A and D contain a significantly higher amount of $Fe_4C_3O_{12}$ compared to $Fe_4C_4O_{13}$, whereas sample B contains almost solely $Fe_4C_4O_{13}$ and no $Fe_4C_3O_{12}$. These results in combination with the thermodynamic conditions during laser heating suggest a decomposition of $FeCO_3$ and a formation of $Fe_4C_3O_{12}$ at lower temperatures with a subsequent formation of $Fe_4C_4O_{13}$ at higher temperatures, which is in accordance with the findings of Cerantola et al.[22] Based on this premise, the formation of $Fe_4C_3O_{12}$ in sample C is likely due to the first heating process at 2300 K, whereas $Fe_4C_4O_{13}$ was forming in the second heating process at 2800 K. In fact, sample C was the first cell in which sp^3-carbonates have been synthesized and after the first heating process Raman spectroscopy showed only contribution of $FeCO_3$. Thus, it was unclear if new phases have been synthesized and the sample was heated a second time. After the second heating process the low-wavenumber bands appeared. Furthermore, both samples that contain a significant amount of $Fe_4C_4O_{13}$ were laser heated from both sides, which reduces the temperature gradient in the sample and enlarges the area with sufficiently high temperature for the synthesis of $Fe_4C_4O_{13}$. Based on these findings a formation path is suggested as follows:

$$Fe^{2+}CO_3 \longrightarrow Fe_4^{3+}C_3O_{12} \longrightarrow Fe_2^{2+}Fe_2^{3+}C_4O_{13} + \text{iron-oxides}$$

Stoichiometric considerations imply that in the first reaction process carbon has to be released. Moreover, in the second reaction process further iron-bearing phases have to be synthesized, most probably iron oxides.[22] Possible candidates are FeO, FeO_2, Fe_2O_3, h-Fe_3O_4, Fe_4O_5 and higher order oxides. However, due to the complexity of Bragg reflections of both sp^3-carbonates no oxide phase could be identified.

Despite the complexity of the phase distribution, the combination of characterizing methods with XES imaging provides convincing results of iron in both sp^3-carbonates in HS for both iron containing sites. This is verified for $Fe_4C_3O_{12}$ by sample A and $Fe_4C_4O_{13}$ by sample B, whereas sample C again confirms the results for both sp^3-carbonates. Sample D extends these results from temperature quenched to *in situ* high temperature conditions, at least for $Fe_4C_3O_{12}$.

These findings are important for the chemical composition in the Earth's mantle, especially in the vicinity of subducting slabs, due to the increased amount of carbonates present compared to the other parts of the lower mantle. It has been shown that the iron's spin state strongly influences the element partitioning between FP and SP, which are the most abundant phases in the deep Earth.[11–16] In case of ferrous iron an exchange of iron with magnesium is possible and Piet et al.[15] have shown that with the onset of the iron's HS to LS transition in FP its abundance in the FP is increasing on loss of iron in the SP. For ferric iron the mechanism is more complex. Piet et al.[15] report an increasing iron content in FP starting at around 70 GPa, i.e., the onset of the spin transition. The maximum of iron content is at 85 GPa, which is subsequently reversed with an iron migration into the SP. The effect is explained by a change of the iron's valence state from ferric to ferrous iron in the SP as the $Fe^{3+}/\sum Fe$ fraction in SP follows the same course, although they do not report data on the $Fe^{3+}/\sum Fe$ fraction that represent the complete pressure range. As the FP has an affinity for (ferrous) LS iron, the resulting ferrous iron then migrates to the FP. Shim et al.[16] report the same behavior, but for a lower pressure range with a minimum of the Fe^{3+} content between 40 GPa and 70 GPa. This effect is explained by a change in the substitution mechanism in which it changes from a charge-coupled combined substitution of aluminum and iron to a process in which aluminum incorporates both distinct cation sites in the SP structure.

The increased ionic radius of HS iron compared to LS iron favors a substitution reaction of ferric (ferrous/ferric) iron in $Fe_4^{3+}C_3O_{12}$ ($Fe_2^{2+}Fe_2^{3+}C_4O_{13}$). As both sp^3-carbonates are stable under deep Earth conditions, they may play an important role in the redox equilibrium of the Earth's lower mantle and should be considered in the complex chemistry of the aluminum and magnesium exchange, which is otherwise solely constrained by FP and SP.

In a recent study, Spahr et al.[95] have shown for Sr_2CO_4 that the stability conditions of sp^3-carbonates can be shifted to lower pressures if oxides are present prior to the heating process. It is possible that these findings can be adapted to the formation of iron-bearing sp^3-carbonates, which would stabilize the phases at shallower depth and impact the redox conditions throughout the lower mantle. However, this has to be verified experimentally before conclusions can be drawn.

7 Electronic structure of Fe_2O_3 under pressure

7.1 Scientific background

Iron oxides are highly relevant when discussing the composition of the Earth's lower mantle, as their high density compared to the surrounding phases leads to the subduction all the way down to the CMB.[96] Especially hematite (α-Fe_2O_3) is an interesting case in terms of geolocically relevant materials as it contains ferric iron and is a potential source for magnetic anomalies in the Earth's mantle.[97] The importance of ferric iron is elaborated in Chapter 1. Thus, it has been investigated in numerous studies within the last decades[21,25,28,42,80,98–111] in terms of its structural and electronic changes reaching from ambient to high-pressure and high-temperature conditions. The phase diagram of Fe_2O_3 is complex and contains a variety of phase transitions with pressure and temperature. Recently, Bykova et al.[21] published a detailed stability diagram up to around 110 GPa and 3000 K. As it is the most detailed study in the recent past, it serves as the basis for the following elaboration.

At ambient conditions Fe_2O_3 occurs in the α-phase (hematite) in a $R\bar{3}c$ structure. In this phase, all the iron is in octahedral coordination and in HS state. Under cold compression, the phase is stable to about 54 GPa with a subsequent transition into the ζ-phase with a distorted perovskite structure ($P\bar{1}$). Here, one half of the iron is in octhaedral coordination in LS state and the other half is in trigonal-prismatic coordination in HS state. The transition from the α- to ζ-phase is accompanied by a volume collaps of $\sim 8.4\,\%$. At even higher pressures of 67 GPa a transition into the Θ-phase occurs, accompanied by a further volume collaps of 1.7 %. In this phase, all iron is in trigonal-prismatic coordination in LS state. Θ-Fe_2O_3 is stable to at least 100 GPa under cold compression. However, laser heating from the Θ-phase to temperatures above 1600 K leads to the formation of η-Fe_2O_3 in the post-perovskite structure ($Cmcm$) with again two distinct iron sites in octahedral and trigonal prismatic coordination with both iron sites in HS state but the same unit cell volume as Θ-Fe_2O_3. After temperature quenching only the η-phase remains present. Furthermore, the phase is stable under decompression to around 26 GPa and subsequently transforms back to α-Fe_2O_3. Heating the sample after decompression at 50 GPa results again in a the formation of ζ-Fe_2O_3 and at 41 GPa in the formation of ι-Fe_2O_3, which is in a Rh_2O_3-II type structure ($Pbcn$). This phase contains all iron in octahedral coordination but with a smaller cell volume than α-Fe_2O_3.

For the phases appearing during cold compression (α-, ζ- and Θ-Fe_2O_3) Sanson et al. and Greenberg et al.[25,42] have further investigated the structural and electronic changes. Sanson et al. confirm the volume collapse at ~ 50 GPa but did not detect a further transition within the limits of their analysis. However, their results determined by EXAFS measurements imply, that the Fe-O distances at 74 GPa are best fitting to the Θ-phase. Hence, they put into question the existence of the ζ-phase. On the electronic structure they observe a HS to LS transition by analyzing the pre-edge position of XANES measurements in the pressure range where Bykova et al.[21] report the transition into ζ-Fe_2O_3, but did non detect further changes at higher pressures. In contrast, Greenberg et al.[42] have verified the findings of Bykova et al.[21] on both, structural and electronic changes, with a mutual agreement of the

corresponding pressures. Furthermore, they report a delocalization of the 3d electrons of half of the iron in ζ-Fe_2O_3 and all of the iron in Θ-Fe_2O_3. This delocalization process has been suggested earlier as a possible driver for the drastic volume collapse in the ζ-phase.[101] The following chapter investigates the electronic transitions from α- via ζ- into Θ-Fe_2O_3 under cold compression, using K$\beta_{1,3}$ and VTC emission spectroscopy in addition to 1s2p RXES measurements. The discrepancy between the works of Sanson et al.[25] and Greenberg et al.[42] will be solved and the possibility of a delocalization of the electronic states in ζ- and Θ-Fe_2O_3 will be discussed. Parts of these results are published in Albers et al.[46]

7.2 Experimental details

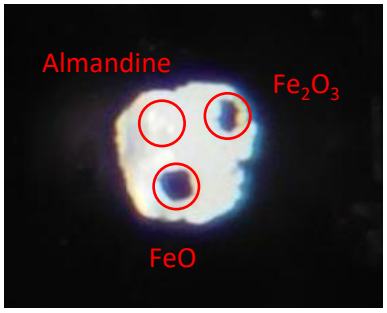

Figure 7.1: Photo of the sample chamber loaded with three different samples as indicated by the red circles. The sample chamber has a size of around 80 µm in diameter.

The sample was commercially available hematite (α-Fe_2O_3) powder (Sigma-Aldrich, 99.995% trace metalbasis), loaded in a BX90-RO cell with argon as pressure transmitting medium. The diamond setup contained an MD on the upstream side and an ST on the downstream side with a culet of 200 µm in diameter without a bevel. Due to the large sample chamber of around 80 µm in diameter, the cell could be loaded with three different samples for different experiments with sufficient distance in between to avoid superposition of the XES signals as shown in Fig. 7.1. The presented data set is a combination of experiments using three different samples in different cells, measured at two different beamtimes at beamline P01 (DESY). A complete list of all measurements is presented in Table B.1. The von Hámos spectrometer was positioned in 70° horizontal scattering angle as described in Chapter 3. The incident energy for K$\beta_{1,3}$ and VTC measurements was fixed to 10400 eV using a Si(111) double crystal monochromator and varied around 7100 eV using a Si(311) double crystal monochromator for RXES measurements, except for the measurements at 13 GPa and 75 GPa which were measured using the Si(111) double crystal monochromator. The incident energy resolution of the RXES measurements was 0.2 eV and 1.0 eV at 7100 eV for Si(311) and Si(111) monochromator, respectively. The energy steps of the incident energy in between measurements were 0.2 eV in the pre-edge area and larger steps in the other energy ranges. For energy calibration, a 1s2p RXES measurement of an iron foil was measured and the inflection point of its K-edge spectrum was set to 7111.1 eV.[24] Hence, all spectra of that beamtime, i.e., all spectra measured with the Si(311) monochromator, were then shifted by the same energy offset of 1.1 eV. For the 1s2p RXES measurement at 11 GPa, a different cell was used that showed an ambiguous energy calibration of the von Hámos spectrometer as the elastically scattered photons appeared on several positions of the detector. Thus, the RXES maps were shifted by 0.8 eV in transfer energy to match the energy calibration of the other measurements during that beamtime. The spectra measured using the Si(111) monochromator were calibrated by overlapping the CEE-cuts and CIE-cuts of 11 GPa and 13 GPa and applying the same parameters for shifting and stretching the spectrum to the measurement at 75 GPa. The raw and adjusted CIE-cuts at 11 GPa and 13 GPa are shown in Fig. B.1. Nevertheless, all CIE-cuts might have an offset in terms of their energy transfer axis, but, the relative energy scale between all plots is correct.

7.3 Experimental results

7.3.1 K$\beta_{1,3}$ XES - spin state

The spin-state development of Fe_2O_3 with pressure was determined by its K$\beta_{1,3}$ emission using the spectrum at 13 GPa as HS reference for IAD analysis. All spectra are shifted to the same COG and normalized to the same area. Fig. 7.2 a) shows K$\beta_{1,3}$ spectra for different pressures along with the difference to the reference spectrum. For clarity, only a selection of spectra is shown (see all spectra in Fig. B.2 in the appendix). The spectra show a slight difference between 13 GPa, 30 GPa and 42 GPa, which is still within the margin of error. Thus, the spectra most probably indicate the iron being a 100 % in HS state. The differences may occur due to a slight distortion with pressure and will be analyzed in detail in Chapter 8. At 50 GPa and 56 GPa the spectrum has changed significantly with a drop in spin state, but the sample is still not completely in LS state. At 75 GPa the LS amount has further increased and the spectrum is significantly closer a complete LS state. In b), the IAD values for all pressures are visualized for two different experiments. To quantify the IAD value changes, a scale was spanned open by the IAD value calculated for the difference between $FeCO_3$ measured at 36 GPa (HS) and 75 GPa (LS).[33,37,83,112] This sets a scale for a spin state change of ΔS=2.0 and is indicated by the gray dashed lines for steps of ΔS=0.5 as orientation. The gray shaded area serves as a guide to the eye to follow the spin state development. The IAD values of Fe_2O_3 are in a complete HS state within the margin of error up to 42 GPa. At increasing pressure the sample shows a two-fold transition, first between 42 GPa and 57 GPa and second at pressures above 64 GPa. At 50 GPa the IAD value is in between the values from 42 GPa and 57 GPa, which suggests a mixture of the α- and ζ-phase with different spin states. Starting at 57 GPa, a plateau ranges to at least 64 GPa, which is in the stability range

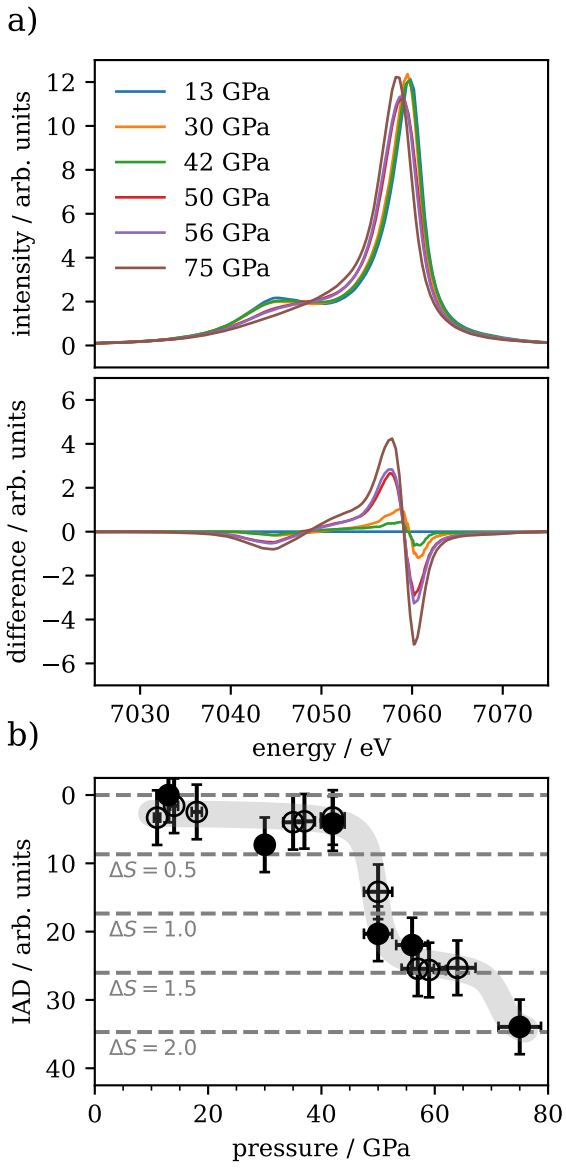

Figure 7.2: a) Selected K$\beta_{1,3}$ emission spectra of Fe_2O_3. Underneath the spectra the difference to the spectrum measured at 13 GPa is shown for IAD analysis. b) IAD values of Fe_2O_3 under pressure, measured at two different beamtimes (solid: 2020, open: 2022). The solid points represent the spectra in a). The gray dashed lines indicate spin value changes, determined by the difference between $FeCO_3$ measured at 36 GPa and 75 GPa (ΔS = 2). The gray shaded area is a guide to the eye (modified after[46]).

of ζ-Fe_2O_3. Although the ζ-phase contains HS and LS iron sites with equal abundance, the IAD values between 57 GPa and 64 GPa substantially differ from the value for ΔS=1.0. This might be based on the symmetry reduction of the trigonal prismatic HS site, as seen similarly for FeO (compare Chapter 8), which undergoes a rhombohedral distortion under pressure and its K$\beta_{1,3}$ XES spectra also show a decreased Kβ' intensity.[47] The resulting IAD value change in FeO is about 20 % of a complete HS-LS transition. Transferred to this case, the IAD value of ζ-Fe_2O_3 should be around 60 % of a completed spin transition, i.e., ΔS=1.2. The values determined here are noticeably higher, which might be due to the fact that the scale of ΔS=2.0 for $FeCO_3$ is not necessarily the same for Fe_2O_3, or that the impact of the symmetry reduction on the IAD-value is higher in this case. At 75 GPa the IAD value increases further to ΔS=2.0. As no spectrum was measured at higher pressures it is unclear if the sample is in a complete LS state. Based on Mössbauer measurements by Greenberg et al.,[42] about 70% of the sample should be in the Θ-phase at 75 GPa, while 30% remains in the ζ-phase, which might explain the difference in IAD value in the ζ-phase and implies a higher range for ΔS=2.0 in case of Fe_2O_3. However, due to the limited amount of measurements in this pressure range, a definitive conclusion cannot be drawn. Nevertheless, a two-step reduction of the average spin state with pressure that relates to the expected phase boundaries of Fe_2O_3 under cold compression can be concluded.

7.3.2 K$\beta_{2,5}$ XES - valence-to-core

VTC-XES is useful tool to analyze the chemistry around the absorbing iron atom, as it is sensitive to the coordination, bonding distance and type of ligand.[50] However, its intensity is small compared to the K$\beta_{1,3}$ emission and requires significantly longer measurement times. Thus, only at selected pressures high-quality VTC spectra were acquired. In Fig. 7.3 a) VTC spectra are shown for the same pressures as in Fig. 7.2 a) (all spectra are shown in Fig. B.3). To analyze the VTC features, the spectra are background corrected by an arctangent function to remove the tail of the K$\beta_{1,3}$ emission. The spectra show a slight difference in the K$\beta_{2,5}$ line shape between 13 GPa and 30 GPa, which might be induced by a distortion of the iron octahedra within the α-phase.[101] Starting at 50 GPa, its intensity is increasing substantially along with a shift to lower emission energies. The increasing intensity of the K$\beta_{2,5}$ peak is small compared to the intensity increase of the Kβ" peak (compare Fig. B.3). The changes are quantified and shown in Fig. 7.3 b) with the COG position of the K$\beta_{2,5}$ peak in the upper as well as the integrated intensity of the Kβ" peak in the lower plot. The differences in errorbars are due to differences in the spectras' quality and are calculated by the square root of the counting rate n of all integration points N, multiplied by $\sqrt{2}$ to account for the background subtraction:

$$\Delta\text{K}\beta\text{"-intensity} = \sum_N \sqrt{2} \cdot \sqrt{n}$$

The error of the COG-position was estimated with 0.6 eV for the solid symbols and 0.9 eV for the open symbols to account for the lower data quality. The COG-position shift correlates with the first phase-transition at around 50 GPa. However, the second phase transition is not detectable within the limits of this analysis due to limited amount of spectra in the respective pressure region. To some extent the shift can be explained by the overall shift of the K$\beta_{1,3}$ emission and the shift of the whole spectrum to the same COG. However, the difference between the α-phase and the ζ/Θ-phase is ∼1.8 eV for the K$\beta_{2,5}$ peak and only ∼1.0 eV for the K$\beta_{1,3}$ main line.

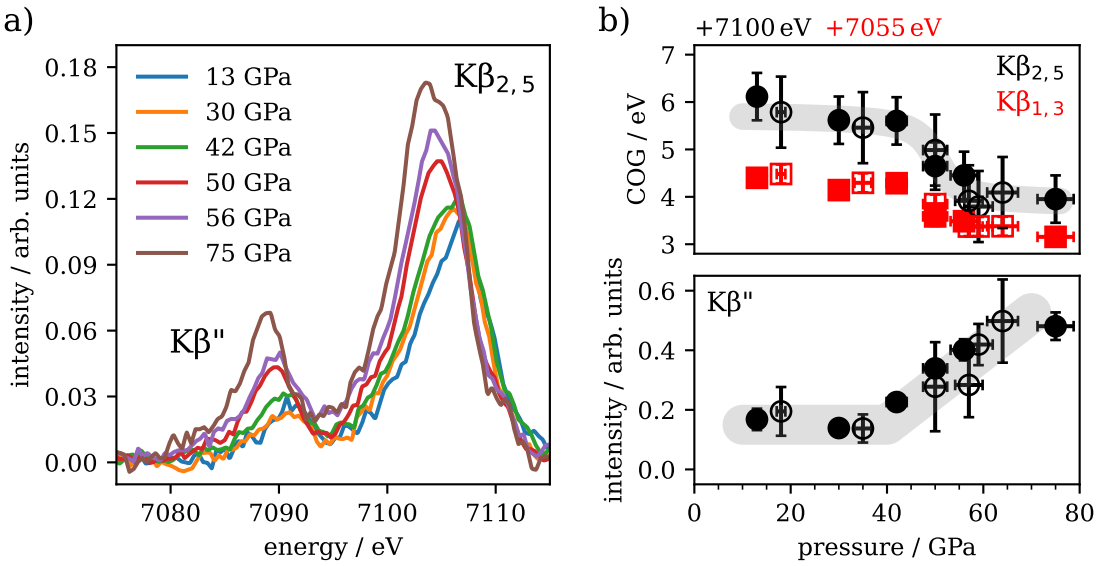

Figure 7.3: a) Selected background corrected VTC spectra of Fe_2O_3 for different pressures and phases, corresponding to the spectra shown in Fig. 7.2. b) (top) COG position of the $K\beta_{2,5}$ emission line (black) compared to the $K\beta_{1,3}$ main line position (red) along with a guide to the eye in gray, measured during two different beamtimes (solid: 2020, open: 2022). For a better comparison, the COG positions are shifted by 7100 eV (black) and 7055 eV (red). (bottom) Integrated Kβ" intensity with a guide to the eye as gray shaded area. (Modified after[46]).

The Kβ" peak originates from hybridization with the ligand's 2s orbital and is very sensitive to changes in the Fe-O bonding distance. It has been shown, that the Kβ" peak rises exponentially with decreasing metal-ligand distance,[50] due to increased hybridization. Thus, its intensity originates mainly from the lowest Fe-O distance rather than the mean distance. Contrary, Spiekermann et al.[29] report a linear relation between the Kβ" and $K\beta_5$ intensity, but, as the $K\beta_5$ peak cannot be isolated here, an analysis of the relation is not possible. As seen also for the spin state, up to 42 GPa the Kβ" intensity is constant within the margin of error (Fig. 7.3 b)). Subsequently, there is a strong increase in intensity with pressure, indicated by the gray shaded area. In α-Fe_2O_3 at ambient conditions there are two Fe-O distances of 1.94 Å and 2.11 Å ,[113] which decrease to 1.83 Å and 1.99 Å at 51 GPa.[42] In ζ-Fe_2O_3 the iron is present in different coordinations with the general formula $A_2B'B''O_6$.[42] The lowest Fe-O distance at 54 GPa is present on the LS octahedral B' and B'' sites with mean distances of 1.86 Å and 1.78 Å, respectively, and little variation in between the distances.[42] Hence, the majority of the intensity is originating from the B'' site, followed by the B' site. However, both octahedra are only occupied by 25 % of the total iron. At 75 GPa the integrated intensity has more than tripled compared to the pressures below 42 GPa, in the α-phase. Structural data by Greenberg et al.[42] report, that at 74 GPa, in the Θ-phase, the iron is only present in a single trigonal prismatic LS site and its mean Fe-O distance (1.82 Å) is slightly higher than for the B'' site, but, as there is only a single iron site with little variation in between the Fe-O distances, 100 % of the iron is contributing to the Kβ"-peak.

7.3.3 1s2p resonant X-ray emission

The XES measurements have shown that the sample remains in a complete HS state with octahedral coordination to at least 42 GPa. Fig. 7.4 a) shows 1s2p RXES maps for pressures between 11 GPa and 46 GP, along with CIE-cuts in b) for each incident energy in the pre-edge region with focus on the $K\alpha_1$ emission. The CIE-cuts are shifted in intensity for clarity. In Fig. 7.5 a) CEE-cuts are shown with an integration range of 3 pixels, i.e., ~ 1.1 eV. The sample is in HS state for all pressures as the pre-edge area contains both expected transitions into the $^5T_{2g}$ and ^5E_g states. However, a small mixture of LS iron can not be ruled out unambiguously for the highest pressure as no XES spectrum was acquired. To analyze the crystal field splitting, the pre-edge region was reconstructed using two

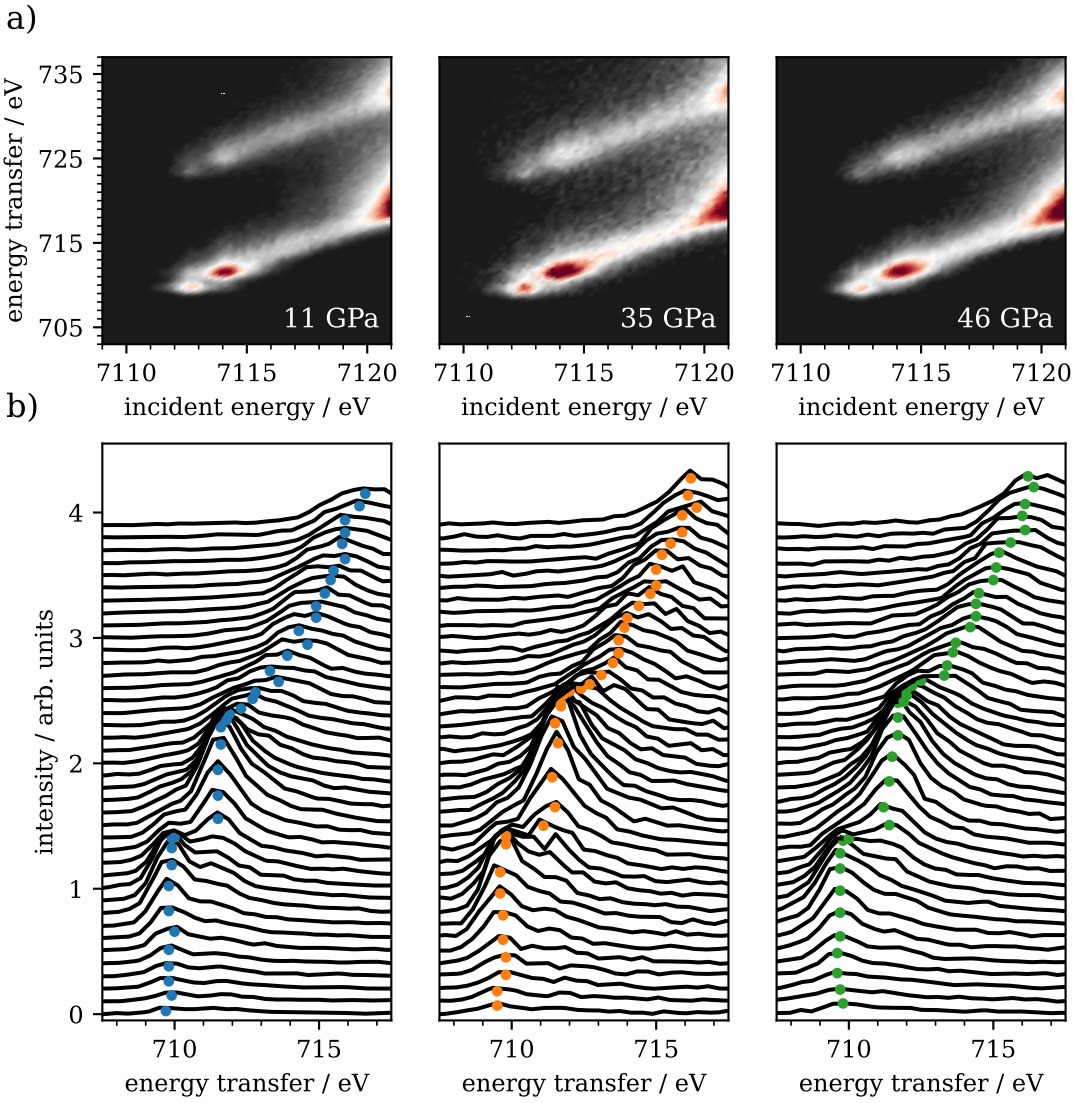

Figure 7.4: a) 1s2p RXES maps of α-Fe_2O_3 for different pressures along with the corresponding CIE-cuts in the pre-edge region with focus on the $K\alpha_1$ emission in b). The CIE-cuts are vertically shifted for clarity. The colored dots mark the maximum position of each CIE-cut (see Fig. 7.9, modified after[46]).

Table 7.1: Crystal field splitting values for different pressures of α-Fe_2O_3 calculated by the position of two Pseudo-Voigt profiles each. The error of each peak position is estimated with ± 0.1 eV and 0.14 eV for the splitting energy between the $^5T_{2g}$ and ^5E_g states (see fit results in Fig B.4).

pressure / GPa	CEE-split / eV	CIE-split / eV
11	1.59	1.83
35	1.70	1.90
46	1.78	1.97

Pseudo-Voigt profiles for the $^5T_{2g}$ and ^5E_g transitions and an arctangent function as step function to reproduce the delocalized transitions at higher incident energies.[24] The position of the step function is fixed to 7115 eV and the spectrum was fitted between 7110 eV and 7116 eV. The resulting crystal field splittings are listed in Table 7.1. Theoretically, the intensity ratio between $^5T_{2g}$ and ^5E_g states should be 3:2 due to the number of orbitals in each state. However, the deviation from this ideal ratio is due to orbital hybridization[80] and is reported in the literature.[24,80,114]

At ambient pressures, the crystal field splitting of α-Fe_2O_3 is reported to be ∼1.4 eV.[80,114] Here, the crystal field splitting is increasing with pressure from 1.59 eV at 11 GPa to 1.78 eV at 46 GPa. An increasing crystal field splitting is expected due to the decreased Fe-O distance with increasing pressure. The crystal field splitting energy at the spin transition is estimated to be ∼ 1.8 eV. The intensity at higher incident energies (> 7115 eV) is due to delocalized states with a hybridization via bridging oxygen 2p orbitals to neighboring Fe-atoms, leading to a mixing of Fe_1(3d)-O(2p)-Fe_2(4p) states.[79,80,115,116] Its intensity is depending on the degree of orbital mixing and is influenced by the Fe-O-Fe bond length as well as the bonding angle.[79] The intensity is maximized for small distances and angles close to 180°. For all phases discussed here the maximum bonding angle is around 130°.[21,101]

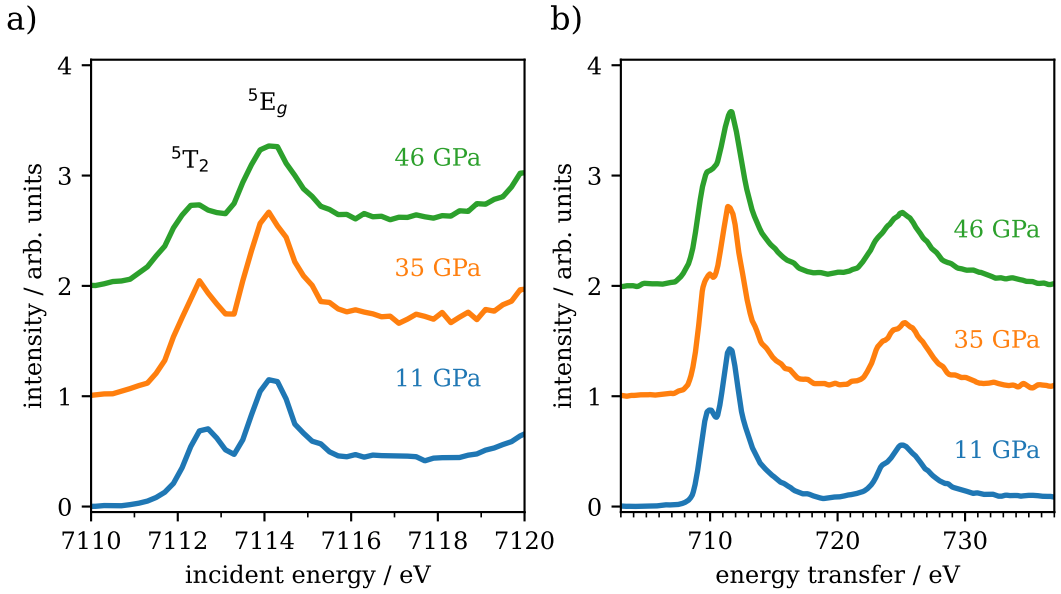

Figure 7.5: a) Integrated CEE-cuts and b) CIE-cuts for different pressures in the α-phase with an integration range of 3 pixels each, i.e., 1.1 eV and 0.6 eV, respectively (modified after[46]).

Hence, the intensity is relatively low compared to the $^5T_{2g}$ and ^5E_g transitions.

Integrated CIE-cuts are shown in Fig. 7.5 b) with an integration range of 3 pixels for each transition, i.e., 0.6 eV. The energy scales of the resulting spectra show an offset to spectra published in the literature,[80,114] which is likely due to an absolute error in the energy calibration. However, as this offset is present in all L-edge like spectra, the comparability between the spectra is maintained. Again two Pseudo-Voigt profiles are fitted to the transitions along with a third Pseudo-Voigt profile fixed at 714 eV to reproduce the tail at higher transfer energies. The energy splittings are also shown in Table 7.1. Between 11 GPa and 46 GPa the energy splitting increases by about 0.19 eV and 0.14 eV for CEE- and CIE-cuts, respectively. The error of each peak position is estimated with 0.1 eV, which leads to an error of 0.14 eV for the energy splitting. Although the accuracy of each single

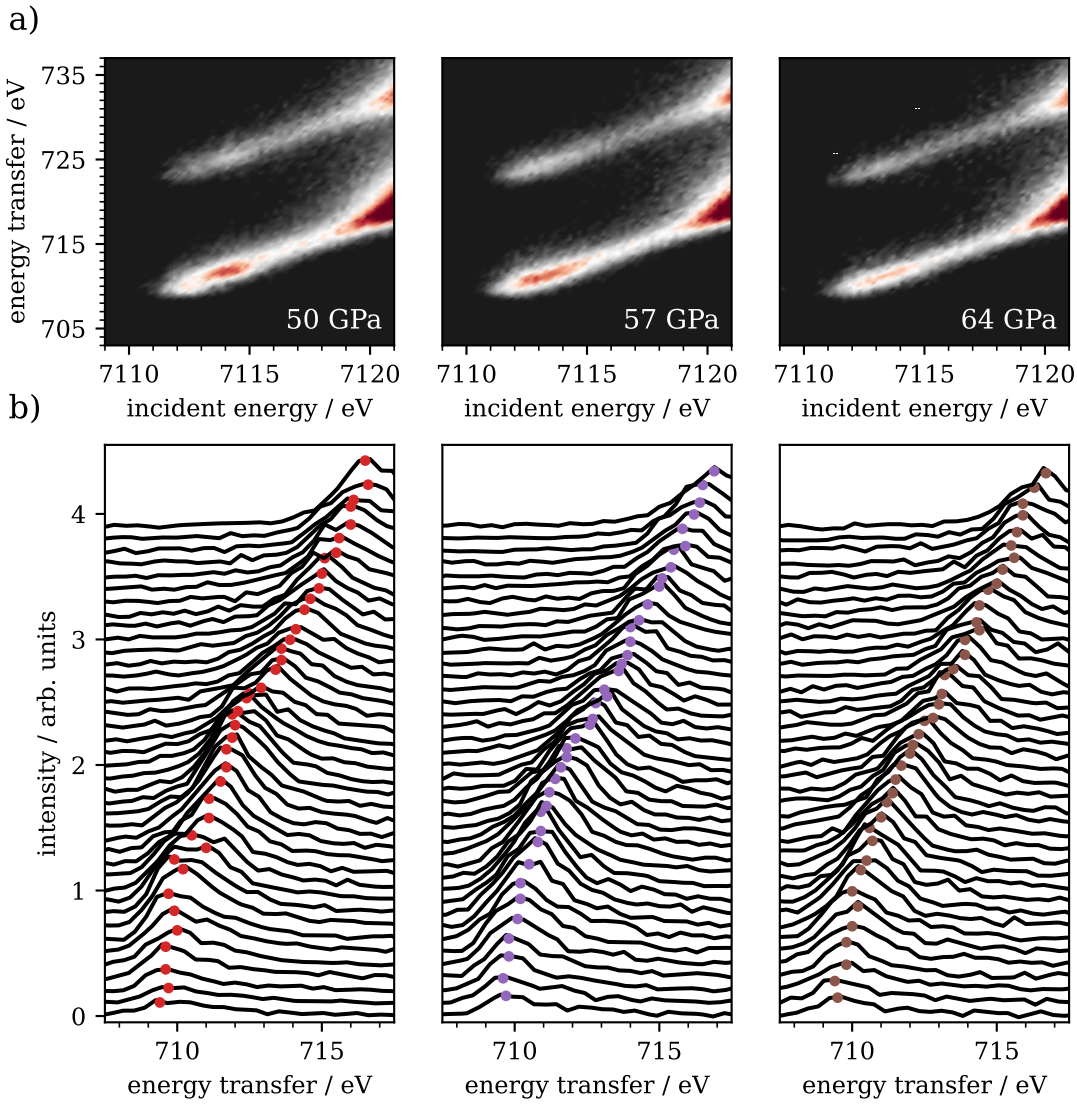

Figure 7.6: a) 1s2p RXES maps for different pressures during the transition from the α- to the ζ-phase along with the corresponding CIE-cuts in the pre-edge region with focus on the $K\alpha_1$ emission in b). The CIE-cuts are vertically shifted for clarity. The colored dots mark the maximum position of each CIE-cut (see Fig. 7.9, modified after[46]).

fit has a large uncertainty, a clear trend can be detected. Furthermore, the energy splitting of the CIE-cuts is ~ 0.2 eV larger than for the CEE-cuts, as the intermediate states are screened via CEE-cut analysis, whereas the final states are screened in the CIE-cut analysis and the changed electron-electron repulsion due to the extra electron in the 3d orbitals may influence the final states by coulomb and exchange interactions.

At high pressures, the XES results show a transition from pure HS state to a mixed spin state. Further, 1s2p RXES maps were acquired at 50 GPa, 57 GPa and 64 GPa to screen the α- to ζ-Fe_2O_3 transition. The results are shown in Fig. 7.6 with the RXES maps in a) and the corresponding CIE-cuts in b), shifted in intensity for better visualization. The CEE-cuts are again calculated by a range of 3 pixels and are shown in 7.6 a) for 46 GPa, 50 GPa and 57 GPa along with integrated CIE-cuts of the whole range between 7111 eV and 7115 eV in b) in order to include all transitions, as no states could be singled out at the higher pressures. During the pressure increase from 46 GPa to 57 GPa, the electronic structure changes significantly. In the CEE-cuts, the COG of the pre-peak region is shifting to lower incident energies, which is consistent to the findings of Sanson et al.,[25] although their limited resolution does not clearly resolve the two-peak feature in the α-phase. However, an exact COG determination is not possible due to the influence of the main-edge subtraction and the delocalized transitions about 7115 eV. Furthermore, the clear distinction between $^5T_{2g}$ and ^5E_g states in the CEE-cuts is vanishing. However, at 50 GPa both transitions are still indicated in the spectrum but superposed with an underlying broad feature. The integrated CIE-cuts show a similar change from two distinct electronic states at 46 GPa into a broad featureless spectrum at 57 GPa with a superposition of both spectra at 50 GPa. As the XES results imply, that the spectrum at 50 GPa is a superposition of the α- and ζ-phase, a compositional fit was performed for both analysis methods and is visualized by the gray dashed lines. The fit range was between 7110 eV - 7116 eV for CEE- and 705 eV - 735 eV for CIE-cuts. The results show a ratio of 57 ± 10 % and 60 ± 10 % of the

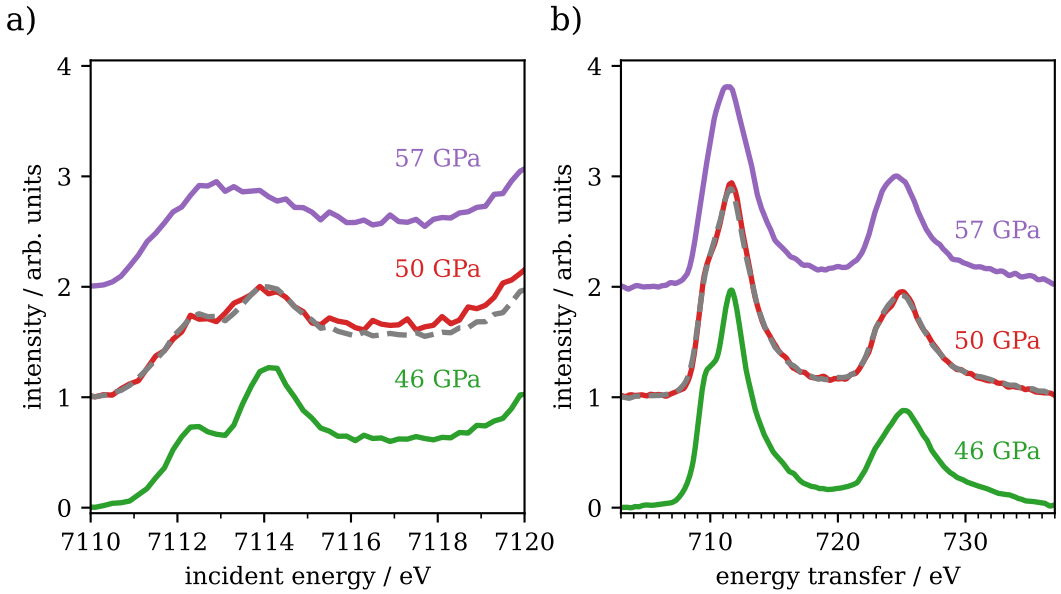

Figure 7.7: a) Integrated CEE-cuts and b) CIE-cuts for different pressures during the transition from the α- to the ζ-phase with an integration range of 3 pixels each, i.e., 1.1 eV and 0.6 eV, respectively. The gray dashed lines are the resulting CEE- and CIE-cuts of the fit results (see text for details) (modified after[46]).

46 GPa spectrum, i.e., the α-phase, in the data for the CEE- and CIE-cuts, respectively. This is in reasonable agreement with the results from the spin state analysis of ∼ 50 % α- and ζ-phase. Furthermore, a small contribution of the ζ-phase at 46 GPa would increase its ratio in the fit results, which might explain the differences between XES and RXES results. Nevertheless, both techniques are in good agreement within the margin of error.

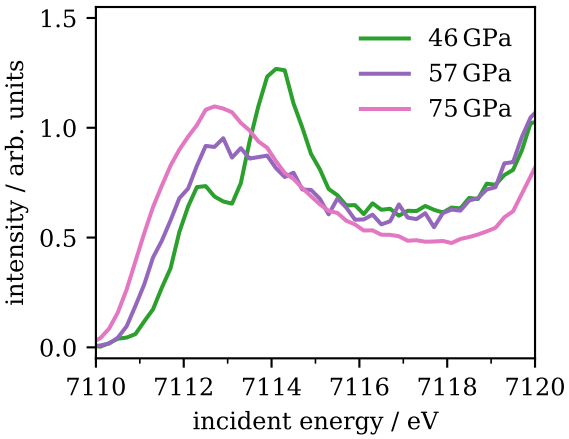

Figure 7.8: CEE-cuts in the α- (46 GPa), ζ- (57 GPa) and Θ-phase (75 GPa).

The transition from ζ- into Θ-Fe_2O_3 is more difficult to analyze as the measurement at 75 GPa was performed during a different beamtime and also using the Si(111) instead of the Si(311) monochromator, which decreases the incident energy resolution from 0.2 eV to 1.0 eV for this measurements. Furthermore, the correct normalization of the absorption edge is difficult due to a Bragg reflection occurring in the post-edge region. Despite these deficiencies, the general structure of the CEE-cuts of the pre-edge region, shown in Fig. 7.8, matches the results of Sanson et al.[25] and Boulard et al.[117] (Supplementary Information) as the COG of the pre-edge region is shifting from the α-phase via the ζ-phase to the Θ-phase to lower incident energies and the transitions around 7113 eV are increasing in intensity with respect to the delocalized transitions at 7118 eV.

The transition from α- to ζ-phase has been investigated before and an insulator-metal transition has been proposed,[42,101] with a delocalization of the 3d electrons, at least for one of the two iron sites. Furthermore, Greenberg et al. [42] proposed that all the 3d electrons in the Θ-phase are delocalized. One indicator for the delocalized continuum-like character of a transition is its dispersion with the incident energy. A discrete localized state is dispersing in emission energy, i.e., is constant on an energy transfer grid, whereas the emission of delocalized states with continuum-like character is constant in energy and thus disperses with the energy transfer.[76–80] Hence, the dispersion characteristics of the emission energy may provide information about the localization of electronic states. However, this assignment is not unambiguous but only an indicator.[118] To analyze this, the shift of the maximum position of the L-edge like spectra from the CIE-cuts were determined for every incident energy in the pre-edge region. Therefore, the spectra were interpolated to 0.1 eV and smoothed by 0.5 eV to eliminated effects of the finite energy resolution by the detector's pixel size. In Fig. 7.9 the maximum shift of the CIE-cuts is shown along with the corresponding CEE-cuts for all pressures. The data points are shown on an arbitrary energy grid as only the dispersion behavior of the maximum is of interest.

The results show that in the α-phase, up to 46 GPa, the maximum position determined from the CIE-cuts is not shifting with the incident energy for the $^5T_{2g}$ and ^5E_g states and that the maximum positions determined from the CIE-cuts at higher incident energies are linearly dispersing. This shows that both states, $^5T_{2g}$ and ^5E_g, are discrete localized states, whereas the intensity at higher incident energies (> 7115 eV) is due to continuum-like delocalized states.[79,118] At 50 GPa the energy dispersion is still detectable for the $^5T_{2g}$ and ^5E_g states but the effect of the ζ-phase is clearly visible. At pressures of 57 GPa and 64 GPa the spectra are almost completely dispersing with the incident energy except for small

range below 7112 eV. The shift at such pressures implies the delocalized continuum-like character of the electronic states. However, according to Greenberg et al.[42] the ζ-phase contains delocalized states in the octahedral LS site and localized states in the trigonal prismatic HS site. Due to the lower symmetry in the trigonal prismatic site, the 3d orbitals split further from t_{2g} and e_g into a_{1g}, e_g^σ and e_g^π orbitals.[42] Following Greenberg et al.,[42] the pre-edge region is thus a superposition of 3 localized states from the trigonal prismatic site and at least two energy dispersive peaks from both delocalized octahedral sites, *B*' and *B*". This might cover several localized states and appear as delocalized states so the results have to be carefully interpreted. In the Θ-phase, the same dispersion behavior can be detected as the maxima are completely dispersing with the incident energy, only at an incident energy around 7110 eV the maxima are constant on an energy transfer grid. These results indicate the delocalized continuum-like character of the transitions, in line with the findings reported by Greenberg et al.[42] Nevertheless, this interpretation is not unambiguous as explained previously and is further complicated by the decreased energy resolution, which might blur out adjacent discrete transitions. Thus, this interpretation has to be taken with care.

Another observation can be made by analyzing the energy splitting between the CIE-cuts at the Kα_1 and Kα_2 emission, i.e., L_3- and L_2-edge like transitions, respectively. Fig. 7.10 presents the splitting energy in a) along with all the CIE-cuts in b), integrated for all incident energies between 7110 eV and 7115 eV. The splitting energy was determined by

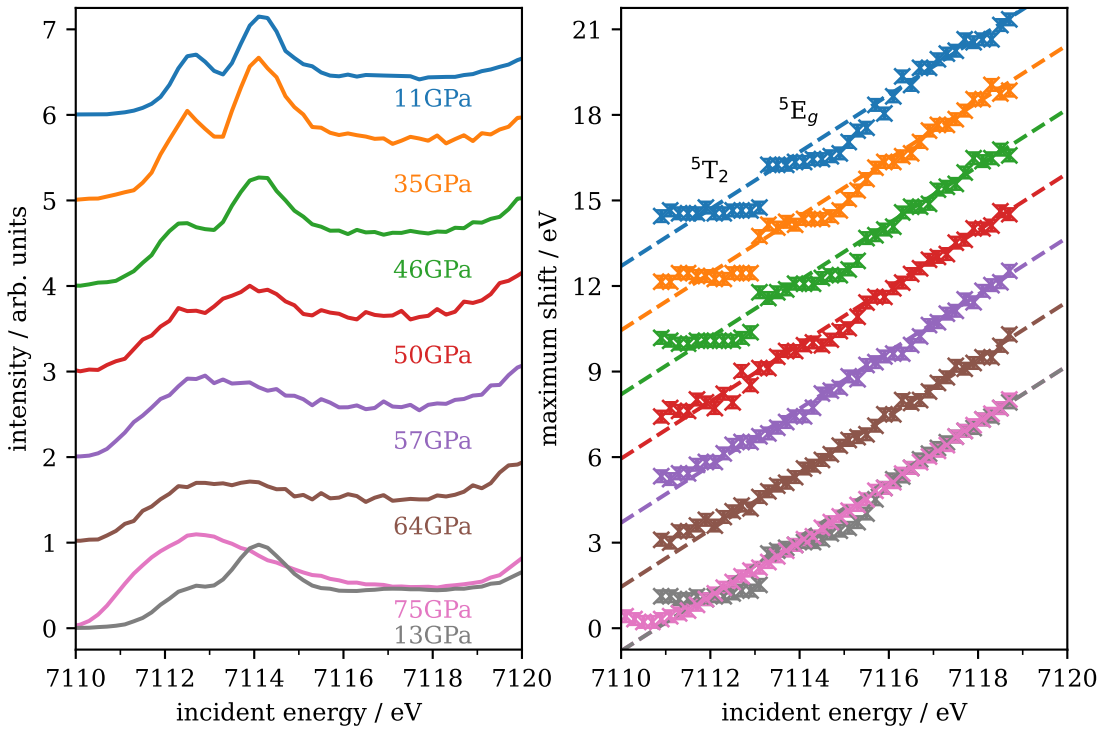

Figure 7.9: (left) CEE-cuts of all pressures with an integration range of 3 pixels each. (right) Dispersion behavior of the maximum of the CIE-cuts in the pre-edge region (see and text for details). The maximum positions are marked in Figs. 7.4 and 7.6 b). Data from both plots are shifted vertically for clarity and the color code is matching. The dispersion behavior of the measurement at 75 GPa could be determined at lower incident energies due to the increased intensity and data quality.

the difference of COG positions of both peaks, calculated on the upper 50% of intensity. The error of each COG-position was estimated to 0.2 eV by varying the range of COG-determintation. The resulting error for the splitting energy is then ∼0.28 eV. It shows, that the splitting energy is decreasing by around 1 eV between the α-phase and the ζ/Θ-phase, which is a result of the decreased spin-orbit splitting at higher pressures due to the spin transition. However, as mentioned previously, the energy calibration of the measurement at 75 GPa was different to the measurements using the Si(311) monochromator and had to be adjusted accordingly for analysis. Therefore, the resulting values for 13 GPa and 75 GPa may differ in regard to the rest of the data set.

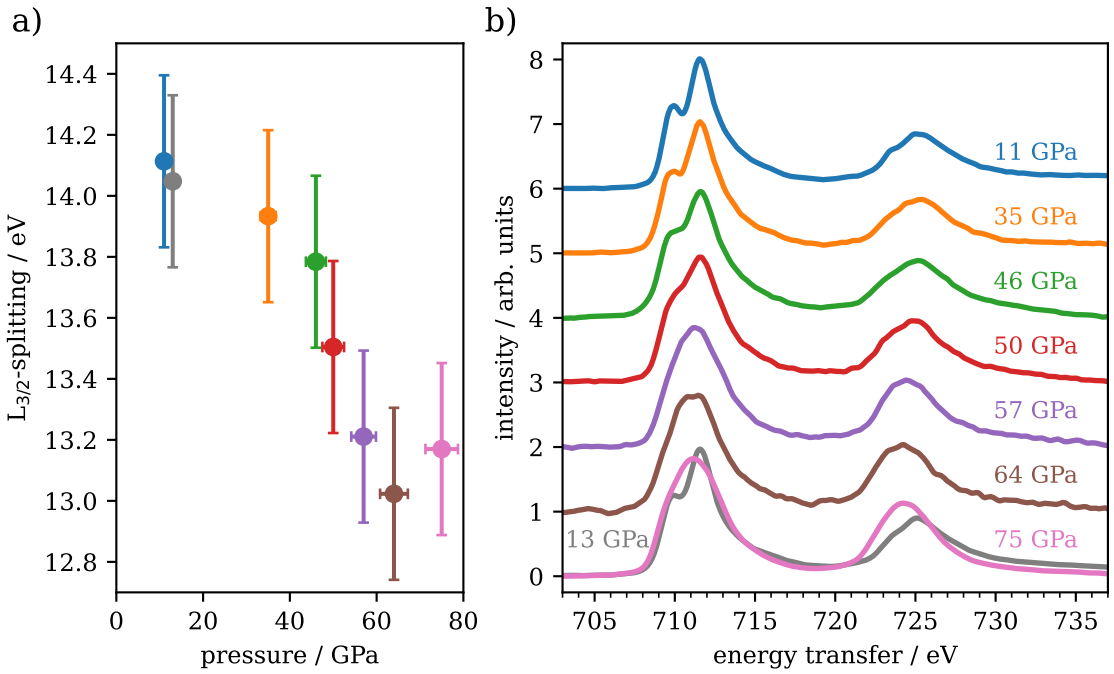

Figure 7.10: a) Splitting energy between the L_3- and L_2-like edge for the CIE-cuts in b), integrated between 7110 eV and 7115 eV incident energy.

7.4 Discussion

In this chapter, the change of the electronic structure of Fe_2O_3 under cold compression was investigated up to the final pressure of 75 GPa using complementary X-ray spectroscopy techniques.

The results of the spin-state analysis by $K\beta_{1,3}$ emission are in good agreement with the findings of Greenberg et al.,[42] which report a first transition between 48 GPa and 56 GPa from the α-phase into the ζ-phase, with a mixed iron spin state, and the onset of the transition into the Θ-phase at 62 GPa, with all iron being in LS state, which is completed by about 70% at 75 GPa. The pressures of the phase transitions observed in this thesis are also in good agreement with the phase transitions published by Bykova et al.,[21] although their X-ray Mössbauer measurements slightly differ from the results of Greenberg et al.,[42] which might be a combination of the lower number of measurements and the data quality. Contrary, the results of Sanson et al.[25] could not be verified, as they report only a single

electronic transition at around 50 GPa with no further changes up to 79 GPa and assign the iron to be fully in LS state above 55 GPa, questioning the existence of the ζ-phase completely. The offset in IAD value for the mixed spin state phase to the expected value can likely be traced back to a reduction in symmetry in the trigonal-prismatic HS site and is in accordance with the results obtained for the distortion in FeO (compare Chapter 8). At the highest pressure of 75 GPa, it is unclear if the sample is already completely in the Θ-phase. Based on the results published by Greenberg et al.,[42] a remaining amount of 30% of the ζ-phase can be expected. Hence, the IAD value compared to the 13 GPa spectrum might increase further with pressure, which would increase the scale of a spin value change of ΔS=2.0 and thus also shift the IAD values in the ζ-phase closer to ΔS=1.0.
Moreover, the VTC measurements are in accordance with the $K\beta_{1,3}$ results and verify the α-phase up to 42 GPa for both, the Kβ" and $K\beta_{2,5}$ peak, with an onset of the phase transition at higher pressures in both features. However, a distinction between the ζ- and Θ-phase was not possible, which might be connected to the limited data quality. It is also possible that the difference between the phases is so subtle that both phases cannot be separated with this method.
Although the data originate from different beamtimes, DACs and samples, the results are in good agreement with each other. Only at 50 GPa the deviation between both measurement series is significant, which is likely due to uncertainties in the pressure determination. As both measurements are very close to the phase transition, an inaccuracy of only 1 GPa might have a high impact on the IAD value.

The RXES measurements up to 46 GPa show the expected behavior with the sample still in the α-phase, i.e., all of the iron is octahedrally coordinated and in HS state.[21,25,42] Both $^5T_{2g}$ and ^5E_g states are clearly detectable and the crystal field splitting is increasing with pressure, which is expected due to the decreased Fe-O distance and results in around 1.8 eV at the spin transition. The transition from α-Fe_2O_3 to ζ-Fe_2O_3 at around 50 GPa is clearly detectable in both, CIE- and CEE-cuts, with an overlap of both phases at 50 GPa. The abundance of the α-phase with 60% and 57%, respectively, is in good agreement between both analysis methods and the results of the XES measurements of ∼50%. The RXES measurement at a pressure of 75 GPa is more difficult to compare as the incident energy resolution is 1.0 eV instead of 0.2 eV due to the Si(111) monochromator. However, the spectrum determined by the CEE-cut is in line with the results of the literature.[25,117]
As explained, the dispersion behavior of the single CIE-cuts might reveal if an electronic state is localized or delocalized. For all measurements in the α-phase, this provides the correct results of discrete localized $^5T_{2g}$ and ^5E_g states and continuum-like delocalized states at higher incident energies.[79,80] After the phase transition from α-Fe_2O_3 to ζ-Fe_2O_3, the electronic states are almost completely dispersing for all pressures with the incident energy except for a small energy range below 7112 eV. Although this assignment might be a product of overlapping localized states, the dispersion behavior and thus the possible delocalization is in line with the results by Greenberg et al.[42] of a site selective delocalization in the ζ- and a complete delocalization in the Θ-phase. However, this assignment is not unambiguous and might lead to false conclusions when only focusing on the dispersion behavior. A linearly dispersing feature might also be a combination of overlapping localized states, whereas delocalized states may also appear as a sharp transition without an energy shift if the transitions is well separated from other excited states.[118]

Furthermore, the splitting energy between the L_3- and L_2-like edges due to the α- to ζ-Fe_2O_3 transition is decreasing by around 1 eV due to a decreased spin-orbit splitting due to the spin transition. A further change in the Θ-phase was not observable in this data

set and might be too subtle to be detected within the limits of the analysis. However, the difficulties in the energy calibration might have a large influence on the results and a more detailed and consistent study has to be performed.

All in all, the results are in line with the findings of Bykova et al.[21] and Greenberg et al.[42] of a two-step transition from α- via ζ- to Θ-Fe_2O_3, accompanied by a two-step spin transition. This is in contrast to the findings of Sanson et al.[25] that only report the first transition at around 50 GPa, which might be due to the limited energy resolution in their study as conventional XANES was applied instead of HERFD-XANES. Furthermore, the 1s2p RXES measurements indicate a possible delocalization of the electronic states as reported by Greenberg et al.[42]

8 Electronic structure of FeO under pressure

8.1 Scientific background

Ferropericlase (FP) $(Fe_x,Mg_{1-x})O$ is an iron-bearing oxide of high relevance in the deep Earth assemblage. Along with silicate perovskite (SP), it builds the dominating phases in the lower mantle.[9,119]
FP has been investigated in numerous studies regarding its electronic structure with a variety of spectroscopic approaches, ranging from optical absorption[120–122] to X-ray Mössbauer[123–129] and (R)XES[28,130–133] experiments. Most of these studies investigated FP in its mixed $(Fe_x,Mg_{1-x})O$ crystal system. Nevertheless, the pure FeO system (wustite) has been also in focus of some studies. As early as 1999, Badro et al.[28] performed first $K\beta_{1,3}$ XES studies on pure FeO and reported no complete spin transition from HS to LS up to a pressure of 143 GPa. However, the $K\beta_{1,3}$ emission line shape changed significantly at the highest pressure. In contrast, Ozawa et al.[134] identified a nearly complete LS state with a transition occurring between 103 GPa and 119 GPa. This is supported by findings of Hamada et al.[135] and Pasternak et al.,[136] who report a slow spin decrease with pressure above 90 GPa, obtained by X-ray Mössbauer spectroscopy.
Complementary studies on the crystal structure of FeO have shown that it undergoes a first transition at a relatively low pressure from cubic ($Fm\bar{3}m$) to rhombohedral ($R\bar{3}m$) crystal symmetry. Yagi et al.[43] report this transition at 16 GPa, whereas Jacobsen et al.[44] report a higher pressure of 23 GPa, with the difference of helium as their pressure transmitting medium instead of a mixture of methanol-ethanol in case of Yagi et al.[43] Hence, the pressure at which the distortion is occurring is depending on the choice of pressure medium. Yagi et al.[43] also report a further distortion of the rhombohedral unit cell at around 40 GPa, which could not be confirmed by Jacobsen et al.[44] up to at least 51 GPa. This might also be based on the different choice of pressure transmitting medium, which shifts the further distortion either to a higher pressure or hinders this transition completely. At higher pressures of about 100 GPa the crystal structure changes into the B8 phase having a NiAs-type structure,[43,137–139] which will not be discussed here.

To investigate the cubic to rhombohedral distortion of pure FeO regarding its influence on the electronic structure, $K\beta_{1,3}$ and VTC results will be presented for pressures up to 75 GPa. The $K\beta_{1,3}$ spectral-shape changes will further be discussed in comparison to Fe_2O_3 spectra in the α-phase, which also undergoes a slight distortion with increasing pressure, but without a change of the crystal symmetry. The impact of this transition in comparison to an increased distortion within one crystal symmetry will be analyzed. Additionally, 1s2p RXES measurements of FeO will be presented in the cubic and rhombohedral phase at 13 GPa and 75 GPa, respectively. Parts of these results are published in Albers et al.[47]

8.2 Experimental details

The investigated sample was synthetic $Fe_{0.94}O$ (FeO from here on).[†] The diamond setup contained an MD on the upstream and an ST on the downstream side with a culet of 200 µm in diameter and no bevel. Argon was used as the pressure transmitting medium. The von Hámos spectrometer was positioned in 70° horizontal scattering angle as described in Chapter 3. All spectra between 13 GPa and 75 GPa were measured on the same sample and in the same sample environment at P01 (DESY), whereas the spectrum at ambient conditions was measured outside of a cell during another experiment at beamline P64 (DESY). In contrast to the experiment at P01, the measurement geometry was horizontally with both, the von Hámos spectrometer and detector on the same height as the sample. Hence, there might be differences between the two experiments regarding background subtraction, energy calibration and energy resolution. An overview of the setup at P64 is presented by Kalinko et al.[140] The RXES measurements were conducted at beamline P01 using the Si(111) monochromator for an incident energy resolution of 1.0 eV at 7100 eV. The energy steps in between measurements were 0.2 eV in the pre-edge area and larger steps before and after the pre-edge region. Information on the measurement of Fe_2O_3 spectra can be found in Chapter 7, as the same spectra were used.

8.3 Experimental results

8.3.1 K$\beta_{1,3}$ XES - spin state

The pressure dependent spin-state changes of FeO were investigated from ambient conditions up to a pressure of 75 GPa. K$\beta_{1,3}$ XES spectra are shown in Fig. 8.1 a) for all pressures, shifted in emission energy to the same COG of 7055 eV for IAD analysis. For an improved visibility, a zoom into the Kβ' emission is shown in the inset. The differences to the LS reference are shown in the plot underneath. As LS reference a spectrum of $FeCO_3$ measured at 75 GPa was used.[46] Overall, the K$\beta_{1,3}$ emission shows a relatively small variation over a high pressure range without complete HS to LS transition. However, at a more detailed analysis certain changes can be identified and in general two pressure regimes can be spotted. With increasing pressure the Kβ' peak is constantly decreasing, typically for a HS - LS transition. These changes are reflected in the resulting IAD values, shown in Fig. 8.1 b), which are constant within the margin of error for the first two spectra, up to 13 GPa. Subsequently, the IAD value drops by $\sim 20\,\%$ and remains on a plateau to least 56 GPa. At 75 GPa there is another decrease in IAD value, which might be connected to the onset of a HS - LS transition, but, as the change is relatively small and only present in a single data point, the results have to be interpreted carefully. In addition, the angle of distortion ($\Delta\phi$) is shown as red crosses with the right axis as scale in Fig. 8.1 b). The angle of distortion is here defined as the mean deviation from the 90° O-Fe-O angle in the cubic phase and was extracted from the structural data of Jacobsen et al.[44] up to 51 GPa.

$$\Delta\phi = \sum_{i=1}^{12} \frac{|90 - \phi_i|}{12}$$

[†]The sample was synthesized by heating of Fe_2O_3 at 1300°C for 48 hours under reducing conditions and was synthesized and provided by Christian Plückthun of European XFEL. Mössbauer spectroscopy showed a fraction of $\sim 6\%$ Fe^{3+} in the sample, which leads to the stoichiometry of $Fe_{0.94}O$.

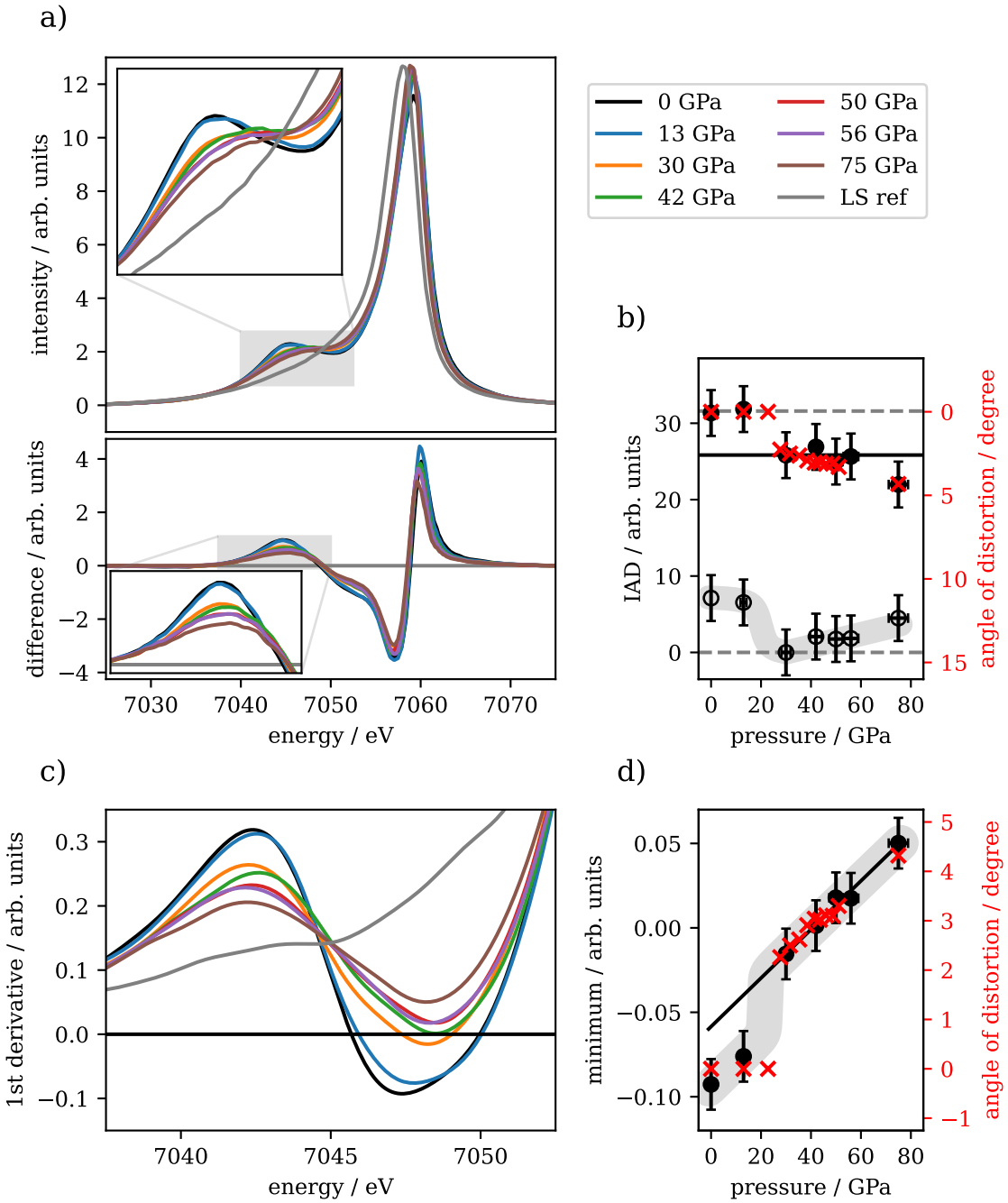

Figure 8.1: a) $K\beta_{1,3}$ spectra of FeO between 0 GPa and 75 GPa along with a spectrum of $FeCO_3$ measured at 75 GPa as LS reference. The inset is a zoom into the Kβ' region for better visualization. Underneath the spectra, the difference to the LS reference is shown. The results of the IAD analysis using $FeCO_3$ at 75 GPa as reference are presented in b) (black, closed) along with IAD values calculated with the spectrum of FeO at 30 GPa as reference (black, open). Gray dashed lines are guides to the eye and represent a full HS - LS transition. The black line also functions as a guide to the eye and represents the offset between 13 GPa and 30 GPa. The red crosses represent the angle of distortion[44] (see text for details). c) 1st derivatives of the Kβ' region for all spectra from a), smoothed by 2 eV. d) Minimum value of the derivatives from c) shown on a pressure grid, again with the angle distortion as red crosses.[44] The black line is a linear fit through the pressures above 30 GPa. The gray shaded area is a guide to the eye. The legend for the spectra is shown in the top right corner and applies to all spectra in a) and c). All spectra except for the ambient pressure are published in[47].

The value at 75 GPa was determined by extrapolation via a linear fit as shown in Fig. C.1 in the appendix. The small distortion of around 3° in the rhombohedral phase is correlating with the drop in IAD value. However, it has to be kept in mind that the value at 75 GPa is only an extrapolation and thus might deviate from the actual distortion at such pressure. To underline the two different regimes, the IAD values are additionally calculated using the spectrum of FeO at 30 GPa as reference in the rhombohedral phase and presented in Fig. 8.1 b) as open symbols, with a gray shaded area as a guide to the eye. It shows that the IAD values at higher pressures up to 56 GPa show a small offset value, which is a systematic inaccuracy caused by the nature of the IAD analysis as showcased in Chapter 4. Nevertheless, the resulting IAD values are even lower than the assumed error of 10 %. In contrast, the IAD values at lower pressures are substantially larger, which underlines that this effect is not caused by the analysis method but a change in the structure of the sample. Furthermore, both pressure regimes show IAD values on a plateau that are constant within the margin of error.

As seen, a disadvantage of the IAD analysis is, that it only shows the difference to a certain reference and might be inaccurate regarding structural changes that do not trigger a complete HS - LS transition. Hence, a more in depth analysis is necessary to account for changes without a spin transition. As seen in the XES spectra in Fig. 8.1 a), the Kβ' peak measured at ambient pressure and at 13 GPa, in the cubic phase, shows a line progression with a clear maximum at around 7045 eV, followed by a clear minimum at around 7050 eV. With increasing pressure in the rhombohedral phase, the shape is changing and the maximum as well as the minimum are significantly less pronounced and converge to a saddle point. The 1st derivatives in Fig. 8.1 c) of the XES spectra from a) illustrate this effect clearly. At 0 GPa and 13 GPa, both minima around 7047 eV are clearly negative whereas at higher pressures the minima are close to zero or even positive. When the minimal values are shown in dependence of their pressure as in Fig. 8.1 d), two distinct domains become noticeable. All pressures above 30 GPa are lining up linearly with pressure as indicated by the black line, which is a linear fit through these pressure points, but the minima in the cubic phase are substantially lower than the linear trajectory. This again indicates, that the cubic to rhombohedral distortion between 16 GPa and 23 GPa is causing changes in the line shape of the $K\beta_{1,3}$ emission as also seen in the IAD analysis, but in contrast, the minimum of the 1st derivative of the spectrum at 75 GPa is lining up with all pressures between 30 GPa and 56 GPa. Again, the angle of distortion is shown as red crosses with the right axis as scale and are in correlation with the analyzed results.

8.3.2 Comparison between FeO and Fe_2O_3

To set the spectral line-shape changes more into context and quantify the changes due to the distortion, the pressure dependent development of FeO and Fe_2O_3 was compared. In case of α-Fe_2O_3 the iron is already coordinated in an distorted octahedra at ambient conditions and with increasing pressure this distortion is slightly increasing,[101] whereas FeO is coordinated in a non-distorted cubic crystal symmetry that transitions into a distorted rhombohedral symmetry. In Fig. 8.2 the Kβ' peak of the difference to the $FeCO_3$ LS reference is compared between FeO and Fe_2O_3 spectra for pressures up to 42 GPa, with Fe_2O_3 being in the α-phase for the complete pressure range. Spectra of FeO at higher pressures are also shown for completeness. The spectra of FeO in a) again underline the offset between the cubic phase at low pressures and the rhombohedral phase at higher pressures. However, the spectra of Fe_2O_3 in b) also show these two regimes at similar

pressures, i.e., all pressures up to 18 GPa as well as between 30 GPa and 42 GPa are identical within the margin of error. For a better visualization and comparison, all spectra in the respective pressure regimes are averaged for both samples individually and visualized in Fig. 8.2 c). The position of the maximum is shifted to lower emission energies by 0.7 eV for Fe_2O_3 (similar to Fig. S18 in Lafuerza et al.[75]), but is constant with increasing pressure for both samples. To quantify the difference in peak intensity, all averaged spectra are integrated for ±2 eV around their maximum and shown in d) for both samples. The intensity loss between the low pressure (LP) and high pressure (HP) spectra is higher for FeO ((25.1 ± 4)%) than for Fe_2O_3 ((14.5 ± 4)%), which is likely due to the higher

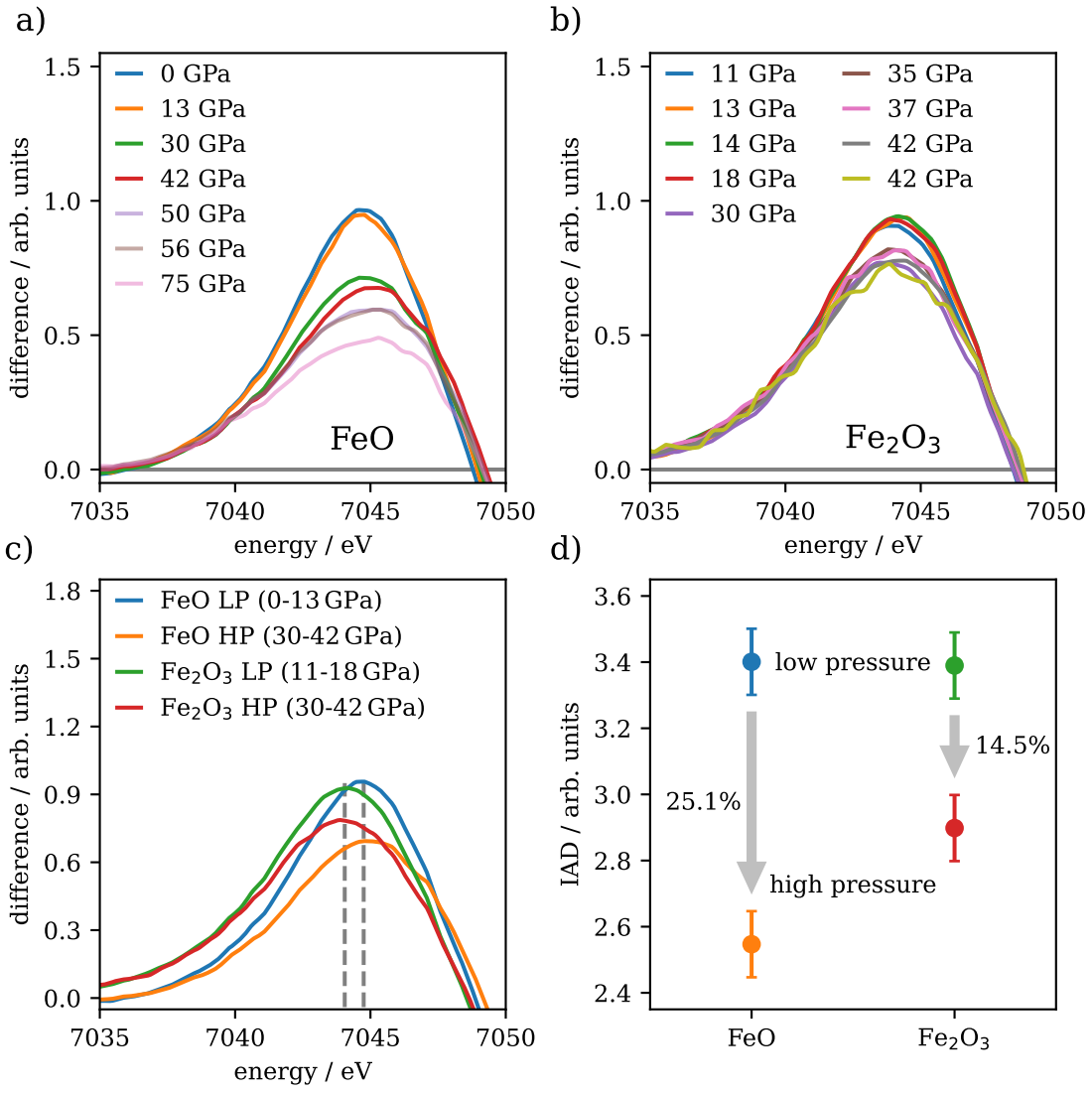

Figure 8.2: a), b) Difference of $K\beta_{1,3}$ spectra of FeO and Fe_2O_3 to the $FeCO_3$ LS reference with focus on the Kβ' area. Spectra of FeO measured above 42 GPa are shown for completeness but are not further analyzed at this point. c) Summed up Kβ' differences for LP and HP regimes. The HP regime contains all spectra with pressure between 30 GPa and 42 GPa. The gray dashed lines underline the difference in peak maxima between both oxidation states. d) IAD value of the peaks from c) integrated for ±2 eV around its maximum. The errorbars are estimated by shifting the spectrum by ±0.2 eV (compare Chapter 4).

degree of distortion as a change in crystal symmetry is occurring. In case of FeO, the angle distortion is increasing from 0° to 2.91° between 13 GPa and 38.5 GPa for all angles uniformly,[44] whereas for Fe_2O_3 the angle distortion is more complex, as the difference to 90° is not uniformly. However, both the mean value of the angle distortion as well as the maximum difference to 90° are only slightly increasing with pressure. Between 12.9 GPa and 38.3 GPa the mean value is changing from 7.13° to 7.24° and the maximum difference is increasing from 12.75° to 13.17°.[101] Hence, the angular distortion is higher in case of Fe_2O_3 for all pressures, but the variation with pressure is much smaller than for FeO. Contrary, the Fe-O distance in Fe_2O_3 is not uniformly, as in FeO, but inhibits two different distances. Rozenberg et al.[101] report an increase of this difference between both distances from 11% to 18% between 12.9 and 38.3 GPa, which might cause the difference in intensity. Furthermore, spectra of FeO measured at pressures above 42 GPa show a further decrease in intensity up to around 50% at 75 GPa, which might be due to a further distortion with higher pressure as reported by Yagi et al.[43] However, this conclusion is only speculative and requires an in depth study (including XRD) to confirm it.

8.3.3 $K\beta_{2,5}$ XES - valence-to-core

At all pressures, VTC spectra were measured and are presented in Fig. 8.3 a). For a better analysis of the features, the tail of the $K\beta_{1,3}$ main line was subtracted by an inverse tangent function. With rising pressure, both Kβ" and $K\beta_{2,5}$ intensities are increasing. Furthermore, the $K\beta_{2,5}$ peak is shifting to lower emission energies as well as its FWHM is decreasing with increasing pressure. This effect is even more pronounced when all peaks are scaled to the same maximum value as shown in appendix C. Nevertheless, a quantitative analysis of the $K\beta_{2,5}$ peak visualizes these changes also very clearly. In Fig. 8.3 b) the COG and

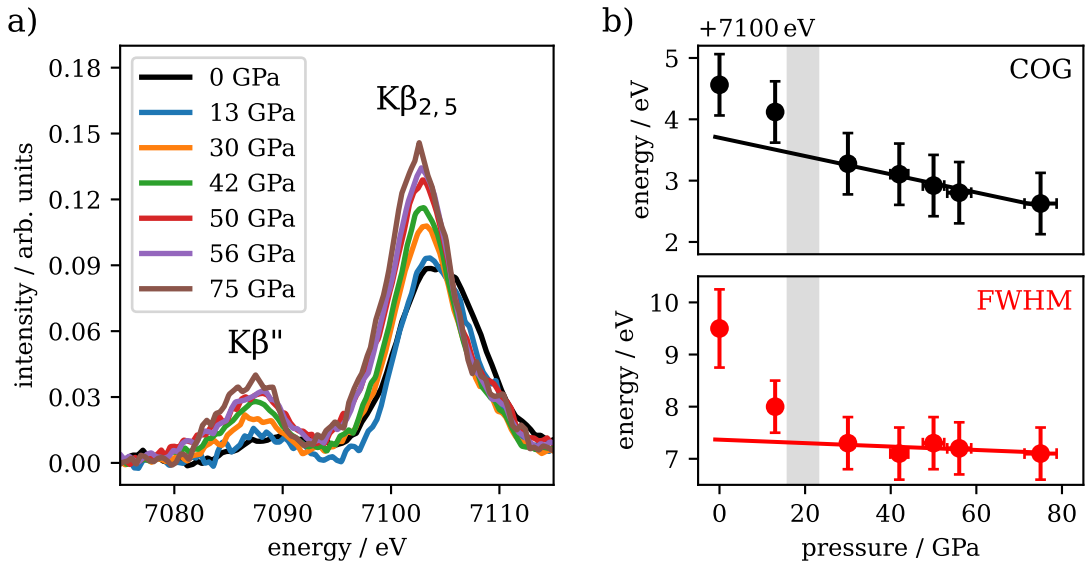

Figure 8.3: a) Background subtracted VTC spectra of FeO measured between ambient pressure and 75 GPa. b) Analysis of the $K\beta_{2,5}$ feature regarding its COG and FWHM. The errorbars were estimated with 0.5 eV. The gray shaded area marks the pressure of the distortion between 16 GPa and 23 GPa. The black and red lines are linear fits through all data points with pressures between 30 GPa and 75 GPa. All spectra except for the ambient pressure are published in[47].

the FWHM of the K$\beta_{2,5}$ peak are shown in relation to their pressure during the measurement. In addition, the gray shaded areas mark the pressure of the cubic - rhombohedral distortion.[43,137–139] Due to the low emission intensity, the VTC spectra are very sensitive to the data handling process, e.g., the background subtraction. Thus, the uncertainties for the COG and FWHM were estimated with a comparably large error of ± 0.5 eV for all measurements at pressure. The uncertainty of the FWHM of the ambient measurements was increased by 50% to account for possible changes in the energy resolution due to the different experimental conditions. The COG was calculated for the upper 50 % of intensity, i.e., the same values that provide the FWHM, to minimize the effect of the background subtraction on the results. Similar to the K$\beta_{1,3}$ emission, the spectra at ambient pressure and 13 GPa differ substantially from the spectra at higher pressures. Between 13 GPa and 30 GPa the COG-position shifts around 0.9 eV to lower emission energies, whereas the COG shifts between 30 GPa and 75 GPa only around 0.7 eV. When taking the linear fit through the values between 30 GPa and 75 GPa as basis, the offset is $\sim$0.9 eV and $\sim$0.6 eV for 0 GPa and 13 GPa, respectively. Additionally, the FWHM drops in the cubic phase from 9.5 eV and 8.0 eV at 0 GPa and 13 GPa, respectively, to around 7.2 eV in the rhombohedral phase. Between 30 GPa and 75 GPa it stays constant within the margin of error. The shift of the COG is neither a product of the energy grid, nor the shift of the spectra to the same COG of the K$\beta_{1,3}$ main line, as the main line is constant at 7058.8 eV with a standard deviation of only 0.1 eV for all pressures (compare appendix Fig. C.2).

The Kβ" emission is very sensitive to the metal-ligand distance.[50] In Fig. 8.4 the integrated intensity of the Kβ" emission is shown along with the Fe-O distance based on the EOS published by Jacobsen et al.[44] For the Fe-O distance at 0 GPa and 13 GPa, the EOS of the cubic phase and at higher pressures the EOS of the rhombohedral phase was used. The intensity was extracted by a simultaneous fit of the Kβ" and K$\beta_{2,5}$ peak with two Pseudo-Voigt-profiles each. Afterwards, the profile of the K$\beta_{2,5}$ peak was subtracted from the spectrum and the Kβ"-peak was integrated between 7078 eV and 7095 eV. This way the rising intensity of the K$\beta_{2,5}$ peak is eliminated. Nevertheless, the results have to be interpreted carefully as the data handling may influence the results. The subtraction procedure is visualized in Fig. C.3. The error was calculated by the square root of the counting rate n of all integration points N, multiplied by $\sqrt{2}$ to account for the background subtraction:

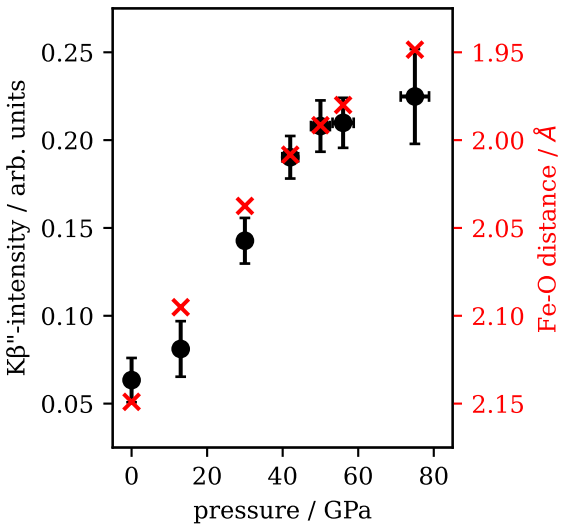

Figure 8.4: Integrated intensity of the Kβ"-peak (black, left axis) along with the Fe-O distances based on the EOS by Jacobsen et al.[44] (red, right axis).

$$\Delta\text{K}\beta\text{"-intensity} = \sum_{N} \sqrt{2} \cdot \sqrt{n}.$$

The error of the ambient measurement was increased by 50% to account for the different experimental conditions. Despite the difficult analysis, a clear trend can be identified within the results and the strong correlation between Fe-O distance and Kβ"-peak intensity is showing. While the Fe-O distance is decreasing by around 10% between ambient conditions

and 75 GPa, the integrated intensity of the Kβ"-peak is approximately tripled. The results show that the structural changes and especially the cubic - rhombohedral distortion is also reflected in the VTC spectra, consistent to the results of the $K\beta_{1,3}$ main line.

8.3.4 1s2p resonant X-ray emission

At 13 GPa in the cubic phase and at 75 GPa in the rhombohedral phase 1s2p RXES maps were acquired. A zoom in the pre-edge region is visualized in Fig. 8.6 a) with focus on the $K\alpha_1$ emission. According to multiplet theory, a $3d^6$ transition metal in octahedral coordination contains 3 electronic states in the HS state, a lower $^4T_{1g}$ (I) state, a $^4T_{2g}$ (II) and another $^4T_{1g}$ (III) state at higher incident energy.[52] Despite the limited energy resolution and the strong overlap of the states, a qualitative analysis of the RXES map may indicate a splitting into 3 different states at 13 GPa. The positions of the states are marked in the RXES map. At 75 GPa, the states cannot be separated anymore by qualitative analysis. By comparing both pressures, it is noticeable that the general structure of the pre-edge region is conserved but the different transitions are smeared out at the higher pressure, which might be connected to the cubic - rhombohedral distortion of the unit cell. Furthermore, the distortion changes the crystal field splitting from a three-fold t_{2g} and a two-fold e_g into a non-degenerate a_{1g} and two two-fold e_g states.[141]

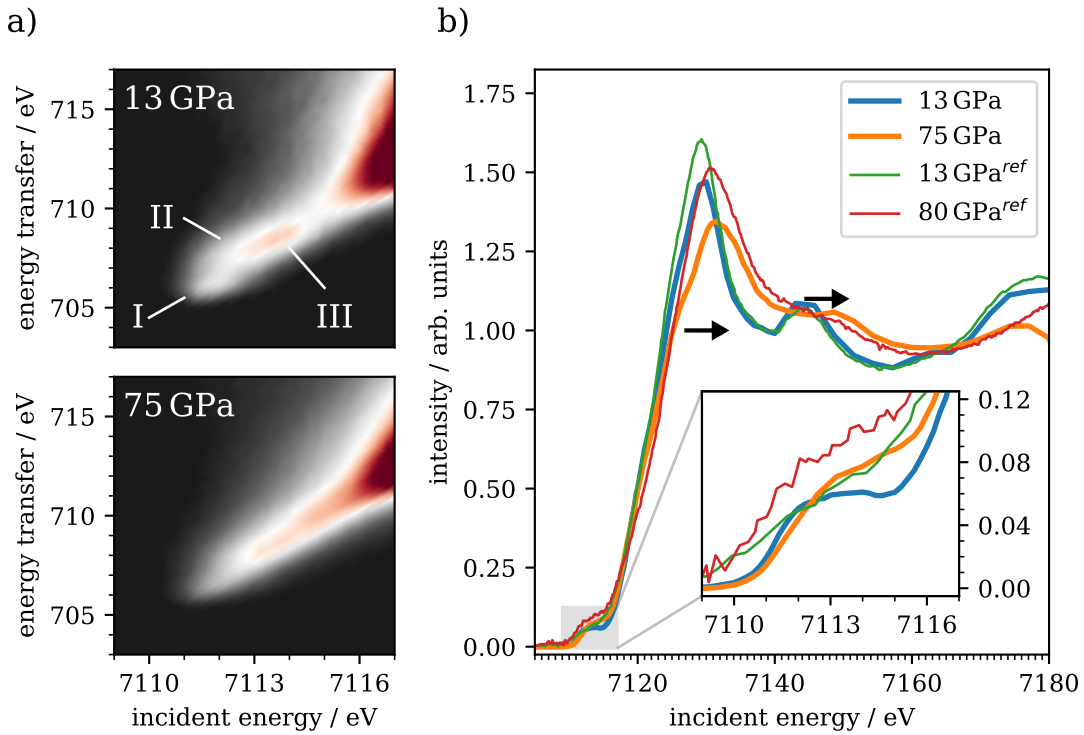

Figure 8.5: a) 1s2p RXES measurements of FeO at 13 GPa and 75 GPa with focus on the pre-edge region. I, II and III indicate the positions of the three expected electronic states (see text for details). b) CEE-cuts for both pressures for an integration range of 11 pixels each. The inset shows a zoom into the pre-edge region. The green and red spectra are digitized versions of Boulard et al.[117] (ref, Fig. S3) measured at 13 GPa and 80 GPa, for comparison. The spectra of the reference are shifted 1 eV to lower incident energies to overlap with the spectra from this study.

The CEE-cuts of the complete XANES spectra are shown in Fig. 8.6 b) for an integration of 11 pixels for each spectrum in the inset with a zoom into the pre-edge region. Additionally, digitized reference spectra published by Boulard et al.[117] at 13 GPa and 80 GPa are added to the figure for comparison. All spectra are scaled to overlap between 7140 eV and 7180 eV, after the K-edge onset. Both spectra measured at 13 GPa are in good agreement with the difference of more distinct features in the reference spectrum, which is probably connected to a lower degree of self-absorption and a smaller energy step size. However, an exact measurement of the sample's thickness was not possible. Although the XANES spectrum reported by Boulard et al.[117] shows a better data quality in the post-edge region, the pre-edge features are significantly less pronounced. At 75 GPa, the XANES spectrum changed substantially with a shift of all features towards higher incident energies. Additionally, all feature are smeared out at the high pressure spectrum. In contrast to both spectra at low pressure, this is no effect of self-absorption as the XANES spectra were measured both on the same sample during the same experiment. The comparison with the reference spectrum shows slight changes between both spectra, which might be due to the difference in pressure. These XANES spectra verify a change in the local coordination of the sample, which is not connected to a full HS - LS transition, when taking into account the results of the $K\beta_{1,3}$ emission analysis.

With increasing pressure also the pre-edge region changes significantly. In Fig. 8.6 all spectra are shown with a subtracted edge for further analysis. Due to the limited energy resolution of the incident X-rays and an overlap of the different states, a dedicated analysis of the single features is not possible in the CEE-cuts. However, with increasing pressure the edge subtracted pre-edge features are shifting to higher incident energies, i.e., from 7112.9 $\pm$0.1 eV at 13 GPa to 7113.3 $\pm$ 0.1 eV at 75 GPa. Additionally, the FWHM on the features is also slightly increasing from $\sim$3.3 eV to $\sim$3.5 eV which might be connected to an increased crystal field splitting by pressure. Nevertheless, the limited energy resolution and data quality require a careful interpretation of the results especially as the change is so subtle. The change in FWHM might also be strongly influenced by the edge subtraction. A comparison with the digitized spectra published by Boulard et al.[117] underlines the substantially improved data quality as well as energy resolution of the RXES measurements. Hence, a dedicated analysis of the digitized data is not feasible.

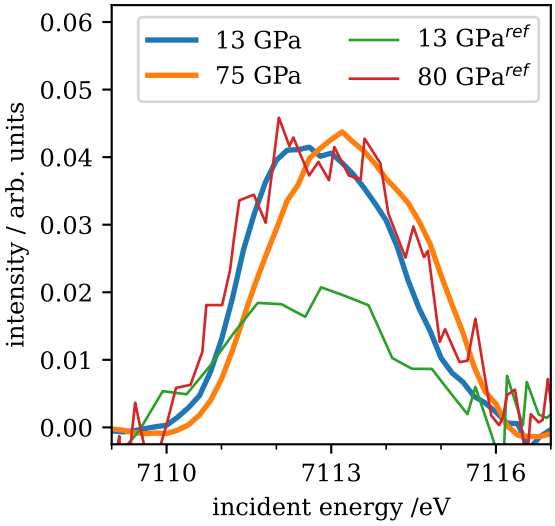

Figure 8.6: Pre-edge features of FeO at 13 GPa and 75 GPa after edge subtraction along with the edge subtracted spectra published by Boulard et al.[117] (ref).

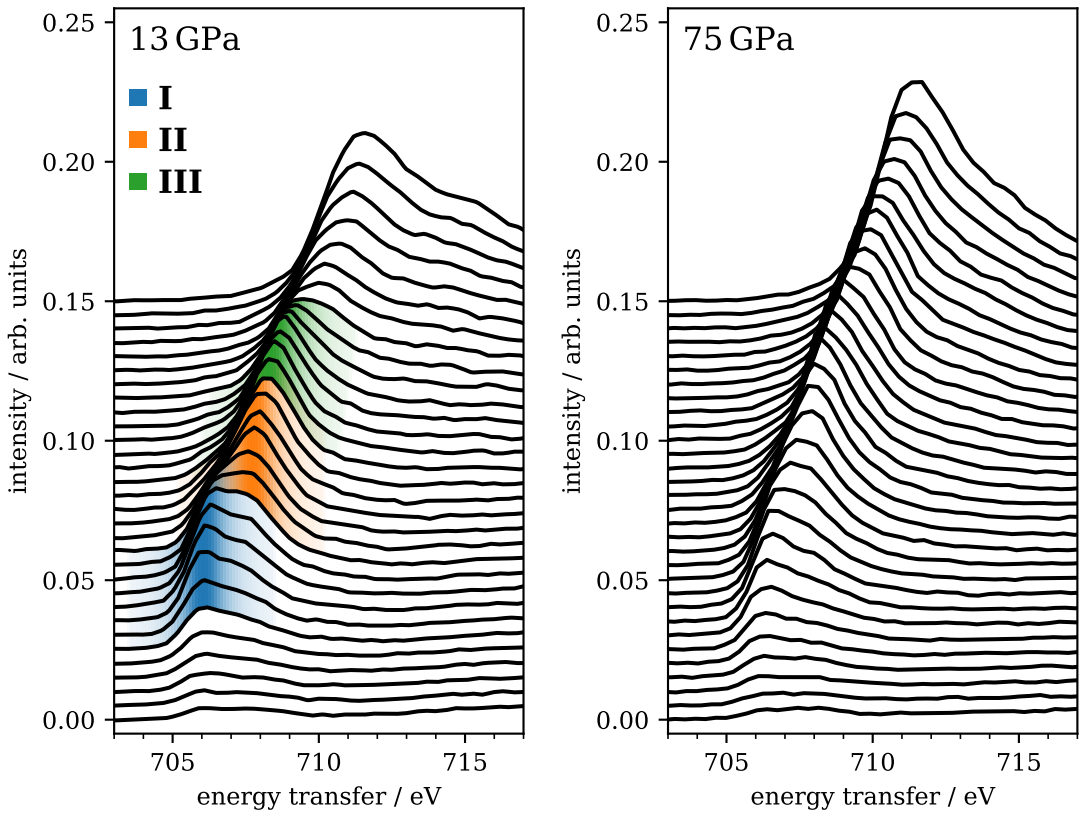

Figure 8.7: 1s2p RXES CIE-cuts at 13 GPa and 75 GPa for incident energies between 7110 eV and 7116 eV, offset in intensity for better visibility.

In Fig. 8.7 all CIE-cuts are shown for incident energies between 7110 eV and 7116 eV, shifted in intensity for clarity. The step size in between two CIE-cuts is 0.2 eV. At 13 GPa a clear distinction between the three transitions is visible, that vanishes when increasing the pressure on the sample. The three different electronic transitions, I, II and III ($^4T_{1g}$, $^4T_{2g}$ and $^4T_{1g}$), are indicated by the shaded areas. At 75 GPa the general structure of the spectra is conserved but smeared out due to the distortion by pressure, which underlines the previous findings.

8.4 Discussion

In this chapter, pressurized $Fe_{0.94}O$ has bee studied up to 75 GPa using different spectroscopic techniques to study the influence of structural variations on the electronic structure and spectral shape changes of a system that does not undergo a spin transition in the investigated pressure range.

Analysis of the $K\beta_{1,3}$ emission to identify changes in the spin state verifies that the sample remains in HS state for the complete pressure range. However, the line shape is changing noticeably for spectra measured before and after the distortion pressure. Especially the Kβ' peak shows a significant decrease in intensity, which is detectable by the derivative

of the spectrum. Although the minimum of the 1st derivative consistently decreases, the change at the pressure of distortion is substantially higher and leads to an offset, which correlates with the angle of distortion in the crystal structure. Furthermore, the line-shape change results in an IAD value change, that is most clearly pronounced when the spectrum measured at 30 GPa is considered as the reference. The results are in line with the reported literature of no spin transition up to at least 90 GPa.[28,134–136] Furthermore, the change in $K\beta_{1,3}$ emission at higher pressures matches the spectra reported by Badro et al. and Ozawa et al.[28,134] The resulting drop in IAD value due to the distortion is $\sim$20% of a complete HS - LS transition. This effect should always be considered in the analysis of pressure induced spin changes of iron-bearing complexes, as it otherwise might lead to incorrect conclusions. Hence, it is unclear if the further decrease of IAD value at 75 GPa indicates a beginning HS - LS transition or is caused by a further distortion of the iron polyhedra with pressure, as indicated by the results of Yagi et al.[43]

The comparison between FeO and Fe_2O_3 in the pressure range up to 42 GPa shows certain differences between both oxides. The significant drop in intensity is due to the higher degree of distortion occurring in FeO than in Fe_2O_3, as in case of FeO the crystal symmetry is changing with pressure whereas in case of Fe_2O_3 the iron is already coordinated in a distorted octahedra at low pressures that gets further distorted at higher pressures, as reported by Rozenberg et al.[101] Contrary to FeO, the Fe-O distances in Fe_2O_3 are not decreasing uniformly, which might have a larger impact on the line shape than the small angular distortion. The onset of the distortion is at around 20 GPa, which is at the hydrostatic limit of argon.[68] In contrast, Schouwink et al.[142] report no increased distortion up to at least 25 GPa with the difference of neon as pressure transmitting in their study, which has better hydrostatic properties at these pressures.[68] Thus, the effect might be based on the choice of pressure transmitting medium. The further decrease of intensity of the Kβ' peak of FeO at higher pressures again indicates a further distortion of the iron polyhedra.[43]

VTC spectroscopy is in general more sensitive to the local coordination around the iron. Hence, the data presented in this chapter also show spectral changes at the pressure of distortion, but, as the features are relatively weak in intensity compared to the $K\beta_{1,3}$ emission, an analysis is even more delicate. In case of Kβ" emission, the integrated peak intensity is significantly increasing with pressure and approximately triples between ambient pressure and 75 GPa, while the Fe-O distance decreases by about 10% in the same pressure range.[44,50] In contrast, the $K\beta_{2,5}$ emission is around 4 to 7 times more intense and allows for a dedicated analysis of the peak shape. Again, the two pressure regimes are detectable in the COG and FWHM of the $K\beta_{2,5}$ emission, in line with the pressures of the cubic to rhombohedral distortion. In case of VTC spectroscopy, the measurement at ambient conditions has to be interpreted even more carefully as the different experimental conditions might have a larger influence on the results. Nevertheless, the results are in accordance with the measurements at high pressure.

Interpretation of the results of the 1s2p RXES measurements is more challenging, as no complete pressure series was acquired but only one measurement at a pressure in each stability region of the cubic and rhombohedral structure. Nevertheless, certain differences between the spectra can be detected that reflect the structural changes. The changes are in accordance with the reported changes by Boulard et al.[117] for both, the maximum position and the post-edge feature at around 7144 eV. In contrast, changes in the pre-edge region are more delicate, but still reflect the further splitting of the electronic states due to the distortion, especially in the CIE-cuts. For a full analysis of the impact of the structural

changes on the electronic states, a more detailed pressure series has to be performed with an improved incident energy resolution, for example by using a Si(311) monochromator.

All in all, the (R)XES measurements of pressurized FeO up to 75 GPa with analysis of complementary spectroscopic features leads to consistent results for all measurements and shows a noticeable influence on the electronic structure due to the reported cubic to rhombohedral distortion between 16 GPa and 23 GPa.[43,44,137,138] The comparison between FeO and Fe_2O_3 underlines the larger impact of a change in the crystal structure compared to an already distorted structure with a small further distortion.

9 Summary and outlook

In the framework of this thesis, the electronic structure of iron in three iron-bearing sample systems was investigated via XES and RXES measurements at pressure and temperature conditions relevant for the Earth's lower mantle. All samples are influencing the chemical composition of the Earth's mantle and the knowledge of their electronic structure helps to understand the complex chemistry of the deep Earth. Furthermore, the experimental setup using a von Hámos spectrometer in combination with an area detector was substantially improved during the course of these studies and provides unique high-quality spectroscopy data on comparably short time scales in the challenging sample environment of DACs.

The first study of geologically relevant sample systems was the determination of the iron's spin state in the recently discovered sp^3-carbonates, $Fe_4C_3O_{12}$ and $Fe_4C_4O_{13}$,[22,40,41] and revealing their formation path. This study is based on four samples that all provide unique information with results that are consistent towards each other. The iron in both sp^3-carbonates is in HS state for all iron sites under high pressure conditions, which is in line with predictions in the literature.[22,94] Additionally, the *in situ* laser-heated measurements verified at least $Fe_4C_3O_{12}$ in HS state at high temperature, although XRD and optical Raman measurements were not feasible under *in situ* conditions due to the already highly complex experimental setup. Hence, the characterization via XRD and optical Raman imaging was performed after temperature quenching. Moreover, a formation path could be derived starting from $FeCO_3$ via $Fe_4C_3O_{12}$ into $Fe_4C_4O_{13}$ formation, which is in accordance with the suggested formation path in the literature.[22] Furthermore, the newly found low-wavenumber Raman bands could be connected to the synthesis of $Fe_4C_4O_{13}$ and the DFT calculations by Prof. Björn Winkler imply that they are a direct result of $Fe_4C_4O_{13}$ formation. As both sp^3-carbonates are in HS state, they might be a possible donor of iron to FP and SP on exchange of magnesium or aluminum and may influence the iron partitioning in those phases, at least in the vicinity of subducted slabs.
In the future, the investigation of the spin state at higher pressure conditions can examine if the carbonates are in HS state for the complete lower mantle or if a spin transition is occurring in greater depths. A possible LS state would turn the effect around and iron could be incorporated in the sp^3-carbonates. Moreover, further studies can be conducted to test if the stability region of these sp^3-carbonates can be extended to lower pressure if oxides are present before the heating process, as shown by Spahr et al.[95] for Sr-bearing sp^3-carbonates. Another interesting but extremely challenging investigation would be the direct measurement of the carbon K-edge in the sp^3-carbonates, which was not verified experimentally up to this point. However, this would require measurements under high pressure conditions and only XRS would be capable to conduct such measurements due to the low energy of the carbon K-edge. XRS is in itself a challenging measurement technique that is further complicated by the fact that the carbon in the sample with a thickness of $\sim$10 µm is pressurized between at least 1 mm of carbon of the diamonds (in case of MDs on both sides). Nevertheless, in principle such an experiment should be feasible due to the imaging properties of the XRS measurement technique.[32,33,143]

In the second study, the changes of the electronic structure of α-Fe_2O_3 and its emerging phases under cold compression, i.e., ζ-Fe_2O_3 and Θ-Fe_2O_3, were investigated via (non-resonant) $K\beta_{1,3}$ and VTC XES as well as 1s2p RXES. The spin-state analysis via $K\beta_{1,3}$ XES clearly verifies a two-step spin transition with the first step around 50 GPa and the second step between 64 GPa and 75 GPa, although the second transition might not be completed at 75 GPa. This verifies the results of Bykova et al.[21] and Greenberg et al.[42] and is contradictory to the results of Sanson et al.,[25] who report a complete spin transition around 55 GPa and question the existence of the ζ-phase. The results here via IAD analysis appear as if in the first transition more than 50% of the iron is changing from a HS into a LS state. However, this might be the result of either a non-accurate transformation of the IAD value to a spin value or the symmetry decrease on the HS site from an octahedral to a trigonal-prismatic coordination, as seen similarly for FeO.[47]
In the VTC emission region, the transition from the α- to the ζ-phase is clearly visible by the COG shift of the $K\beta_{2,5}$-line to lower emission energies. Furthermore, starting at 42 GPa, the intensity of the Kβ"-line is significantly increasing with pressure, attributed to the decreasing Fe-O distance in the respective iron sites. The transition from the ζ- into the Θ-phase was not visible in the VTC emission, which might be either due to the low amount of measurements in the respective pressure regions or the subtlety of changes between these two phases.
The 1s2p RXES measurements show an increase of the crystal field splitting up to around 1.8 eV at the spin transition in the spectra derived from the CEE-cuts and around 2.0 eV in the spectra derived from the CIE-cuts, which demonstrates the influence of the additional electron in the valence orbitals and the effect of electron-electron interactions. At higher pressures, the spectra from the CEE-cuts shift to lower incident energies due to the transition into the ζ- and Θ-phase, in accordance with the spectra reported by Sanson et al.[25] and Boulard et al.[117] Simultaneously, the spectra show a change in the L-edge like transitions from a constant energy transfer of the $^5T_{2g}$ and ^5E_g states in the α-phase to a linear dispersion with the incident energy in the ζ- and Θ-phase. This supports the finding of Greenberg et al.[42] of a delocalization of the electronic states, first on one half and second on all of the electrons due to the phase transitions, although a definitive conclusion on this is not possible, as the energy dispersion with the incident energy is only an indicator of a delocalized state. Furthermore, the distinction of the ζ- and Θ-phase is challenging, as the Θ-phase was measured during a different beamtime and by using a different monochromator for the incident energy. Hence, the energy scales of the different measurements may differ. Nevertheless, especially in the spectra derived from the CEE-cuts there is a noticeable difference between the spectra in the ζ- and Θ-phase.
All in all, the results support the findings of Bykova et al.[21] and Greenberg et al.[42] and contradict the findings of Sanson et al.[25] In the future, a more detailed pressure dependent study could help to better determine the phase boundaries of the different phases, especially in case of the ζ- to Θ-Fe_2O_3 transition. Furthermore, the combination with a laser-heating setup could provide interesting insights into this sample system at conditions more relevant to the Earth's lower mantle.

The third study deals with the changes of the electronic structure of FeO under cold compression and investigates the influence of a structural distortion without a dedicated spin transition on the electronic structure.
XES shows small changes in the $K\beta_{1,3}$ line shape as well as the VTC region occurring in the pressure range where a cubic to rhombohedral transition of the crystal structure was reported.[43,44] This results in an IAD value change of around 20% of the maximum value, determined by the difference between a $FeCO_3$ reference in LS state and the spectra

measured at pressures lower than the distortion pressure. It further shows, that the scale to translate the IAD value to a spin value change (ΔS) is similar between FeO and $FeCO_3$ as HS reference when $FeCO_3$ is used as LS reference, as in the study of Fe_2O_3. When increasing pressure after the initial distortion, the line-shape changes correlate to the angle difference between the cubic crystal symmetry and the rhombohedral symmetry, i.e., the deviation from 90°, reported by Jacobsen et al.,[44] although the angle at the highest pressure was only extrapolated from the values of the lower pressures. In comparison with Fe_2O_3, that also undergoes a small distortion with pressure,[101] the effect on the line shape in FeO is higher than in Fe_2O_3, which can be assigned to a higher degree of distortion occurring in FeO as the deviation in the respective angles in Fe_2O_3 is small compared to FeO.
In terms of VTC spectroscopy, the results show slight but consistent changes and the distortion is clearly detectable in the K$\beta_{2,5}$ peak shape and position. Furthermore, the decreasing Fe-O distance correlates to the integrated Kβ" peak intensity.
The 1s2p RXES results are more challenging to analyze, as the rhombohedral symmetry complicates the detectable electronic states that are already difficult to separate in the cubic phase. Nevertheless, the influence of the distortion is clearly visible in the spectra. This study demonstrates that is not sufficient to draw conclusions by only using the IAD value of a spectrum and its reference. If only focusing on the IAD value change, a possible (false) conclusion could be a structural transition that results in different iron sites of which 20% incorporate iron in the LS state. Hence, further information have to be gathered for a consistent interpretation of structural and electronic transitions. In future studies, it might be interesting to explore if the K$\beta_{1,3}$ line-shape changes are reversible with temperature, as the rhombohedral phase changes back to the cubic phase, if heated to certain temperatures.[144] Also, the investigation of a sample composition that is closer to existing composition in the Earth's mantle would be interesting, i.e. $(Mg_{x-1},Fe_x)O$. It has been shown, that the pressure of the spin transition is depending on the amount of magnesium.[123] Thus, the effect of distortion and spin transition could be separated at lower pressures. Furthermore, a more detailed RXES study with a higher energy resolution would be favorable to better understand the influence of the distortion on the electronic states of FeO. Additionally, a more diversified study of well characterized materials that undergo structural changes without a dedicated spin transition could improve the understanding of structural properties on the K$\beta_{1,3}$ line shape and RXES maps and help to interpret data of materials that are less well characterized.

Additionally, the changes and improvements of the measurement geometry in 70° horizontal scattering angle were elaborated. With the previous scattering geometry, a K$\beta_{1,3}$-XES measurement lasts around 1 hour for spectra with an SNR of 100, which was determined as the lower limit of detection for consistent spin-state results in this thesis. Hence, a maximum of 3 samples could be measured via spin-state imaging within 24 hours, with a grid of only 3 x 3 steps. Furthermore, this only applies for samples with a high amount of iron. A deviation from the optimal measurement conditions leads to spectra with lower SNRs and for meaningful results the measurement times of the spectra have to be increased. As an example, a change from $FeCO_3$ to $(Mg_{0.67}Fe_{0.33})CO_3$ would triple the data acquisition time and only one map could be measured within 24 hours. The same applies for measurements at the rim of the sample. Moreover, measurements of the VTC region were not feasible on resonable timescales. In contrast, the new geometry reduces the data acquisition time for spin-state determination via K$\beta_{1,3}$-XES from around 1 hour to several seconds and allows for new opportunities such as *in situ* laser-heated spin-state imaging and measurements of samples with a lower amount of iron. Additionally, measurement of high-quality VTC spectra can be conducted in less than one hour for

samples with a high amount of iron, which can also be decreased to minutes by binning of adjacent detector pixels.
The combination of the new measurement geometry with an MD on the upstream side also allows for high-quality RXES measurements at high pressure, which was not possible up to this point. A measurement of 1s2p RXES is now possible in about 1 hour with an incident energy resolution of 1 eV. Higher energy resolutions require longer measurement times. Furthermore, the measurement of 1s3p RXES maps is still challenging due to the high background caused by inelastic scattering of the diamond. A change of the geometry in a way to position the von Hámos spectrometer on the same height as the beam with a simultaneous rotation of the cell to measure the Kβ emission in 90° horizontal scattering angle would significantly decrease the background on the detector. Additionally, such an orientation in combination with a second von Hámos spectrometer and detector could allow for measurements on both horizontal openings of the cell and a simultaneous measurement of 1s2p and 1s3p RXES maps could be possible. In this way, the von Hámos spectrometer that analyzes the Kα emission would be positioned at 50° horizontal scattering angle on the opposite side of the von Hámos spectrometer that analyzes the Kβ emission. However, such a setup would be significantly more complicated than the existing one and the time to set up and calibrate all components would increase substantially.
Another major improvement for future studies would be the combination of simultaneous XES and XRD imaging. However, this would require several changes of the setup and lead to deterioration of the data quality or prolonged measurement times.
First, XRD measurements usually require high incident energies of at least 20 keV, which on the one hand decrease the absorption of the incident beam by the upstream diamond and hence, leads to a higher flux of photons on the sample, but on the other hand also decreases the absorption of the beam by the sample and results in a decreased emission. In case of samples that incorporate a heavy element different to iron, higher incident energies can also lead to further emission lines in the spectra, that do not originate from the iron. For example, measurement of a sample containing iron and arsen with an incident energy above 12 kev leads to arsen K-alpha emission on a detector position in the vicinity of the Kβ' peak. Unfortunately, such a mixing of emission lines cannot be countered with a special selection of ROIs to analyze, as both emissions originate from the same sample position.
Second, an XRD measurement in the current setup requires an MD or BA on the downstream side to take advantage of the enlarged opening angle on this side. However, this means that the ST is positioned on the upstream side. While in case of non-resonant XES, a rotation of an MD/ST setup decreases the incident flux on the sample by a factor of ~ 3.2 at 10.4 keV, which might be tolerable in context of the extendet information gain of the experiment, the incident flux in an RXES measurment is decreased by a factor of ~ 40 and the experiment is no longer possible on reasonable time scales.[20]
Third, an XRD measurement *in situ* during laser heating is not feasible in the current setup, at least for double-sided laser heating, as the optics of the laser heating system on the downstream side are too close to the sample and block a large part of the view of an XRD detector on the sample. Hence, the laser heating setup would have to be changed substantially for the gain of a small view of the detector on the sample, or the setup has to be used only on one side with the downside of lower temperatures and a higher temperature gradient.[18]
A possibility to combine XES and RXES measurements with XRD measurements, at least without heating, would be to perform them sequentially rather than simultaneously, i.e., rotation of the cell by 180° in between measurements and change of the incident energy

in the meantime. However, this requires an exact positioning of the sample along the beam's pathway to guarantee the calibration of the sample towards the detector used for XRD, which is more sensitive to deviations in this dimension than the detector used for (R)XES. Furthermore, this will add another layer of complexity to an already complicated experiment and will require a longer time to set up. Thus, both extensions of the setup have to be evaluated carefully if the additional information gain is more valuable than the (R)XES measurements that could be performed in the meantime.
In conclusion, the setup in the new scattering geometry provides spin-state results within seconds, high-quality VTC spectra within minutes and 1s2p RXES maps in less than one hour, offering unique opportunities for spectroscopic measurements at extreme pressure and temperature conditions and will contribute to a deeper understanding of the interior of the Earth and other terrestrial planets.

A Appendix Chapter 6

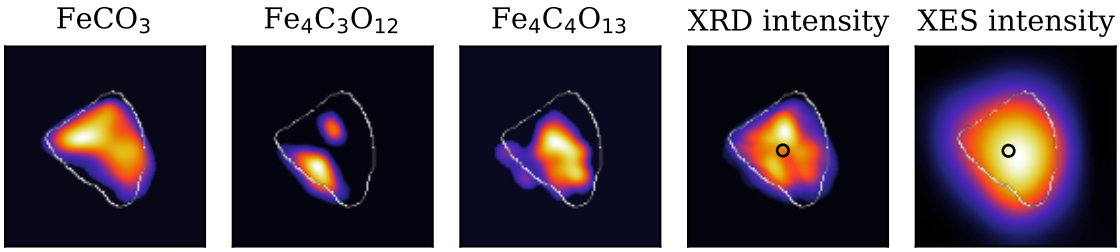

Figure A.1: Spatial distribution of $FeCO_3$, $Fe_4C_3O_{12}$ and $Fe_4C_4O_{13}$, determined by XRD imaging. Furthermore, the sum of the three phases is shown (XRD intensity) along with the intensity map, determined by XES imaging (XES intensity). The black circles represent the COG positions of the intensities of the XRD and XES imaging results. All plots contain the outline of the sample in white.

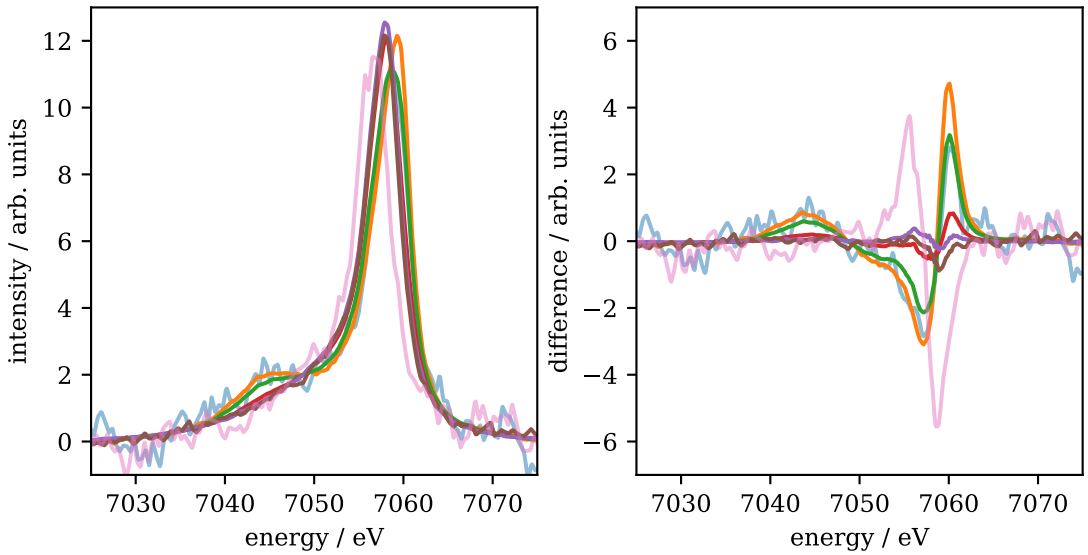

Figure A.2: XES spectra shown in Fig. 6.7, shifted to the same COG (left) along with the difference to the LS reference (right). The color code is matching and spectra with an SNR < 100 are shaded.

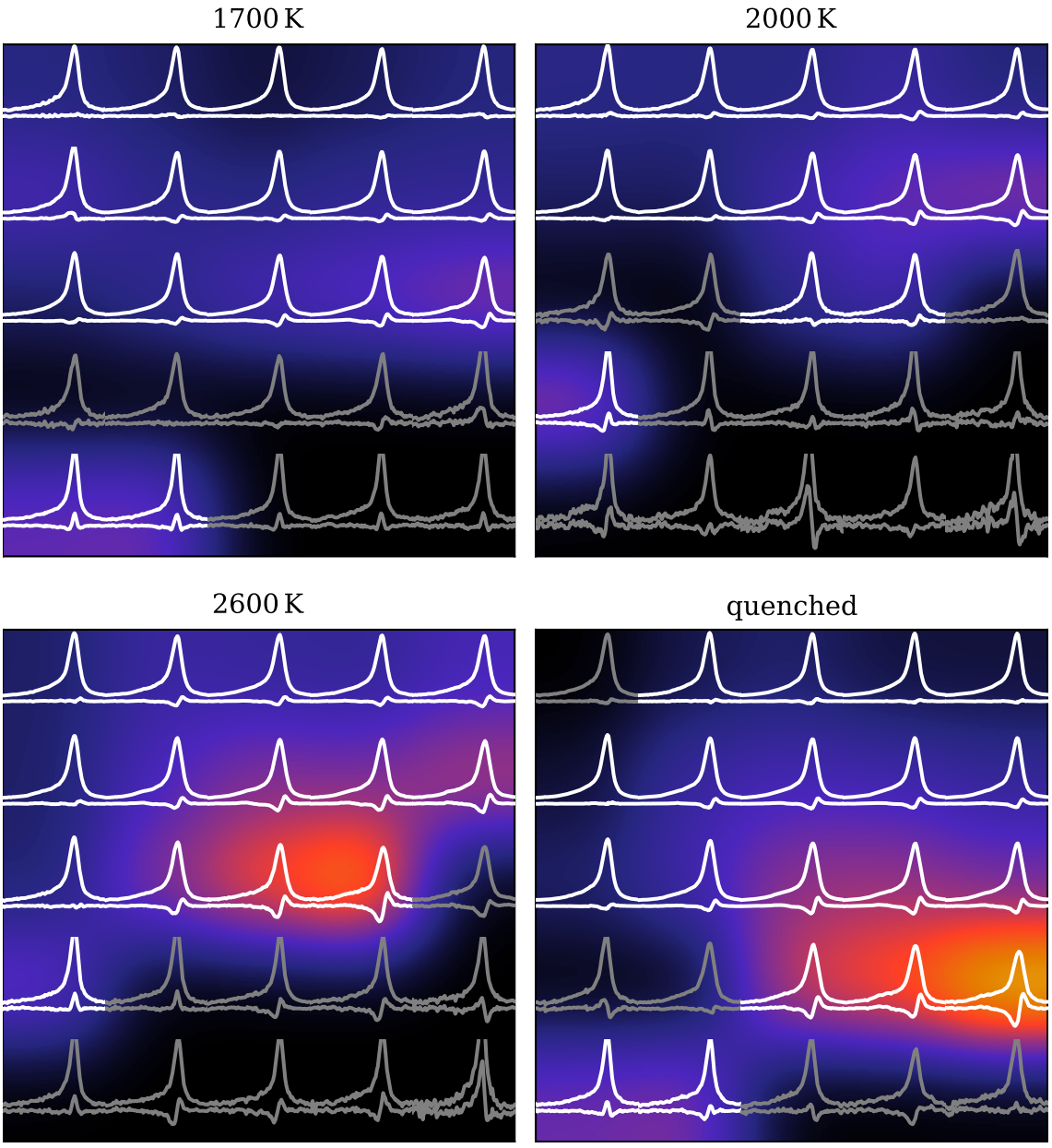

Figure A.3: Representation of all K$\beta_{1,3}$ spectra measured *in situ* during spin-state imaging or after temperature quenching (quenched) at the position of measurement, along with the spin-state map analyzed via IAD. All spectra are normalized to the same area and each spectrum is represented on the same y-scale. Below each spectrum is the difference to the LS reference. Spectra with an SNR < 100 are shown in gray and their spin state is not analyzed but set to 0. The color code corresponds to Fig. 6.11 b).

B Appendix Chapter 7

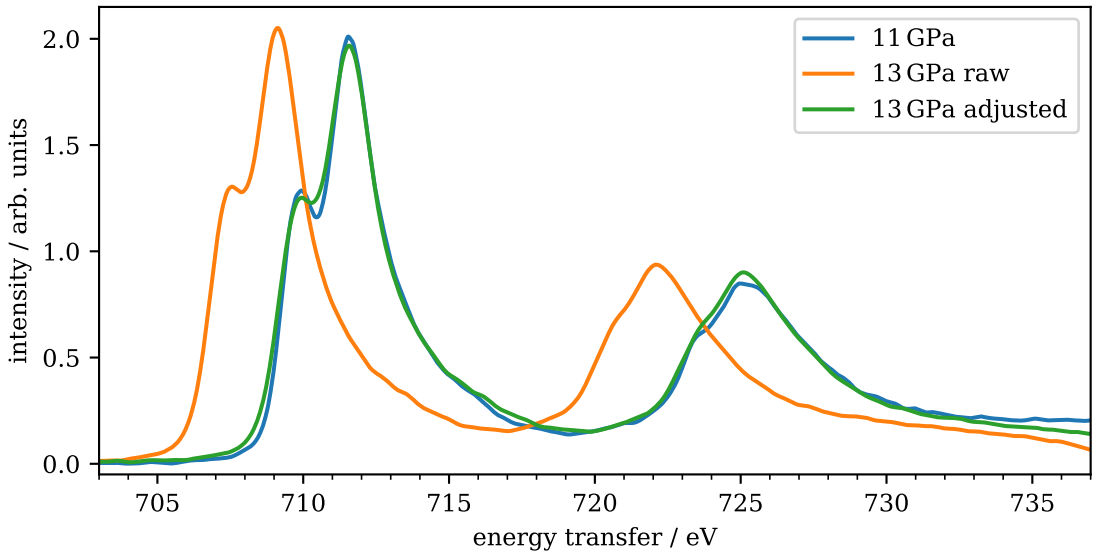

Figure B.1: Visualization of the adjustment of the 13 GPa spectrum, measured with the Si(111) monochromator regarding its CIE-cuts. The spectrum measured at 11 GPa functions as the reference.

Table B.1: List of all measurements and the experimental conditions for each cell loaded with α-Fe_2O_3 and argon as pressure transmitting medium. The error of the pressure is estimated with $\pm 5\%$. RXES spectra of cell 1 were measured using the Si(111) monochromator and cells 2 and 3 were measured using the Si(311) monochromator.

cell 1 (Si(111))			cell 2 (Si(311))			cell 3 (Si(311))		
p / GPa	XES	RXES	p / GPa	XES	RXES	p / GPa	XES	RXES
13	✓	✓	11	✓	✓	35	✓	✓
30	✓	-	14	✓	-	37	✓	-
42	✓	-	18	✓	-	42	✓	-
50	✓	-				46	-	✓
56	✓	-				50	✓	✓
75	✓	✓				57	✓	✓
						59	✓	-
						64	✓	✓

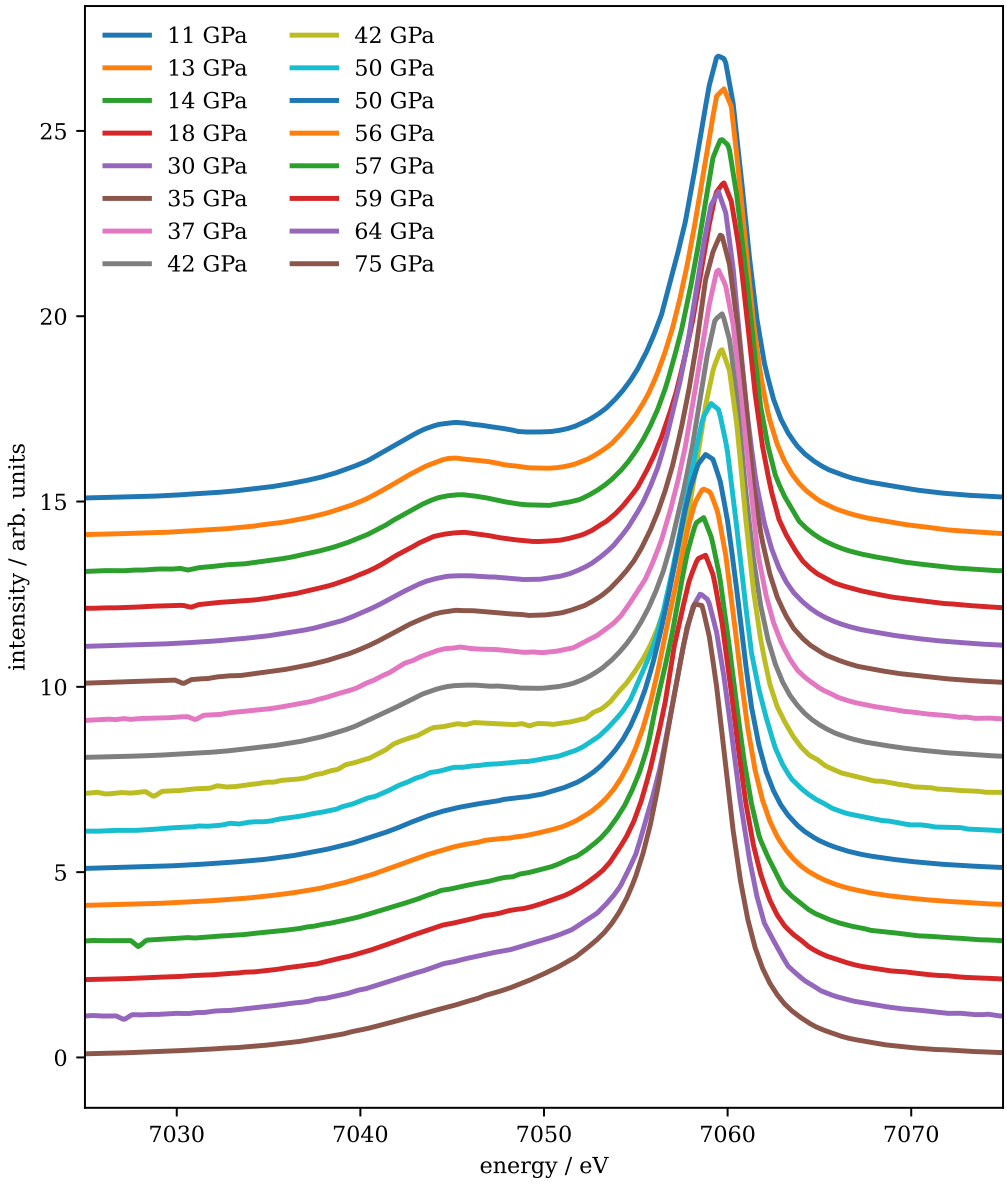

Figure B.2: a) $K\beta_{1,3}$ emission of Fe_2O_3 for all pressures, set-off in intensity for clarity. The pressure is increasing from up to down. The small dip in some spectra at about 7030 ev is due to a dead pixel in the detector panel.

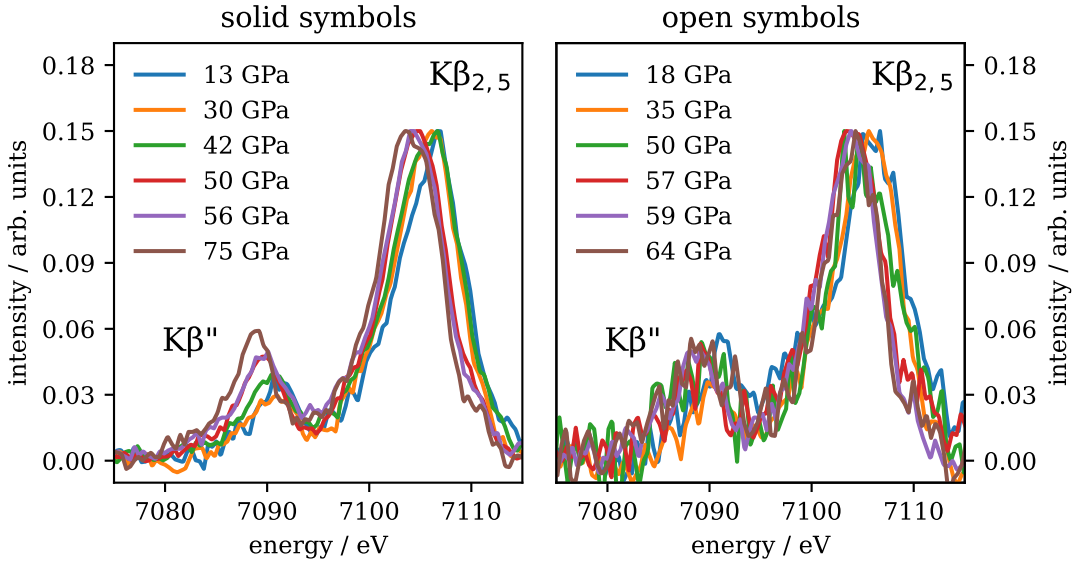

Figure B.3: All analyzed VTC spectra of Fe_2O_3 for different pressures and phases, scaled to the same maximum value. The spectra are split for the solid (a) and open symbols (b), corresponding to Fig. 7.3 (modified after[46]).

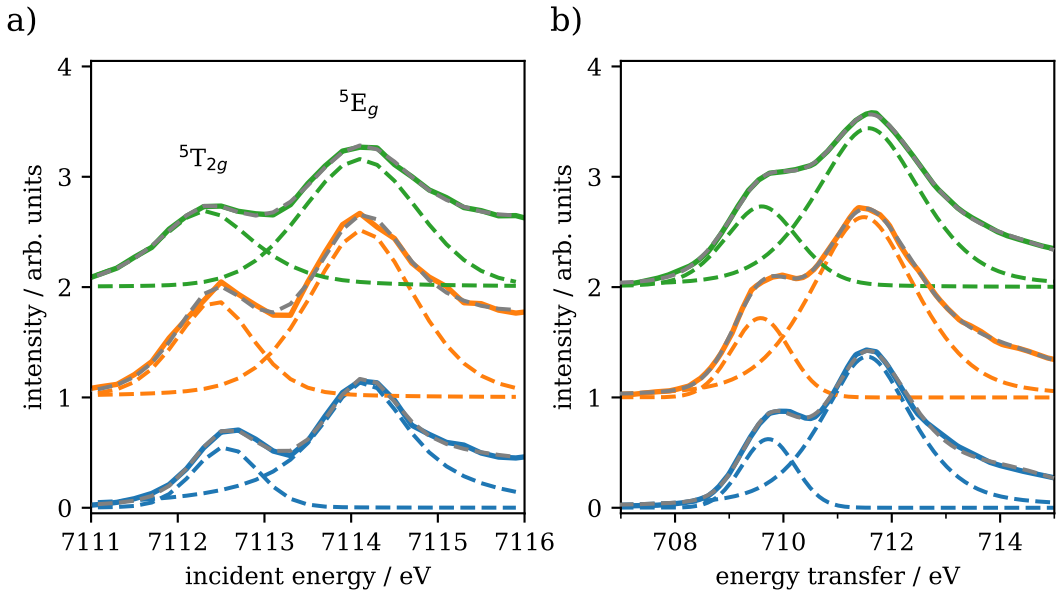

Figure B.4: Fit results for CEE- (a) and CIE-cuts (b), corresponding to Table. 7.1. The colored dashed lines correspond to the $^5T_{2g}$ and ^5E_g transitions, whereas the gray dashed lines are the total fit results.

C Appendix Chapter 8

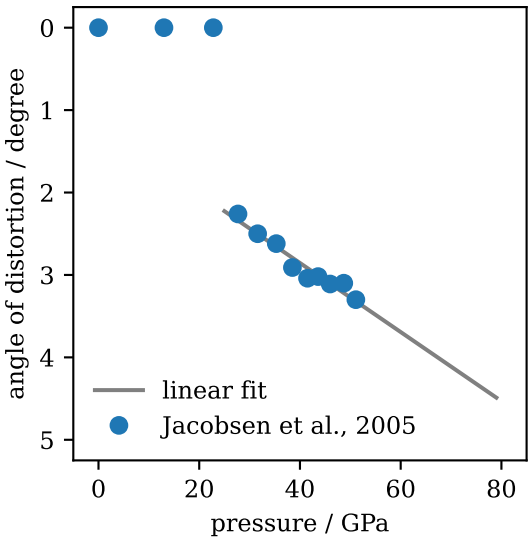

Figure C.1: Angle of distortion of FeO under pressure extracted from the unit cell parameters by Jacobsen et al.[44] along with a linear fit through all angles above 23 GPa for extrapolation to higher pressures. The angle of distortion is defined as the deviation from 90° for all O-Fe-O angles.

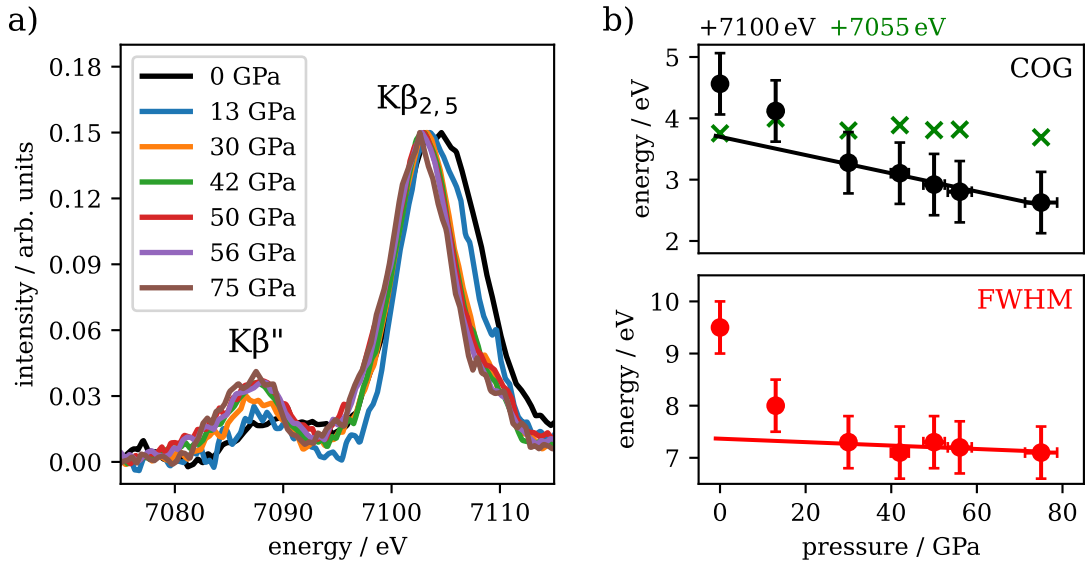

Figure C.2: Background subtracted VTC spectra of FeO for different pressures, scaled to the same maximum of the $K\beta_{2,5}$ emission for comparison. b) (top) COG position of the $K\beta_{2,5}$ (black) compared to the Kβ main line position (green). (bottom) FWHM of the $K\beta_{2,5}$ emission.

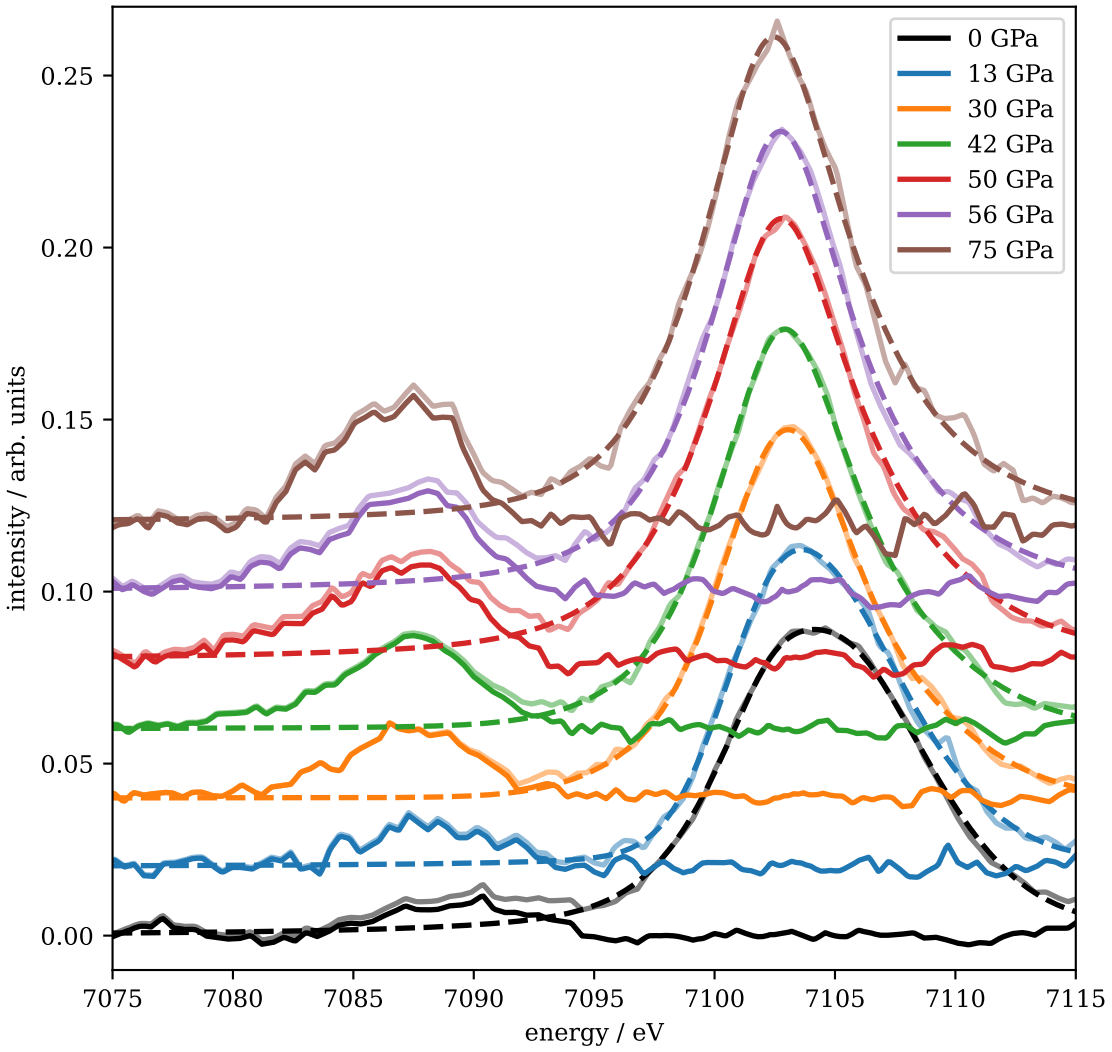

Figure C.3: Pressure dependent VTC spectra of FeO after K$\beta_{1,3}$-tail subtraction as shaded lines. The dashed lines represent the fit result of the K$\beta_{2,5}$ peak using two Pseudo-Voigt profiles and the solid lines show the VTC spectra after subtraction of the K$\beta_{2,5}$ peak to analyze the Kβ" emission. All spectra are offset in intensity for clarity.

Bibliography

1. Dziewonski, A. M. & Anderson, D. L. Preliminary reference Earth model. *Physics of the Earth and Planetary Interiors* **25,** 297–356 (1981).
2. Stixrude, L., Wasserman, E. & Cohen, R. E. Composition and temperature of Earth's inner core. *Journal of Geophysical Research: Solid Earth* **102,** 24729–24739 (1997).
3. Bunge, H.-P., Ricard, Y. & Matas, J. Non-adiabaticity in mantle convection. *Geophysical Research Letters* **28,** 879–882 (2001).
4. Hernlund, J. W., Thomas, C. & Tackley, P. J. A doubling of the post-perovskite phase boundary and structure of the Earth's lowermost mantle. *Nature* **434,** 882–886 (2005).
5. Ono, S. & Oganov, A. R. In situ observations of phase transition between perovskite and $CaIrO_3$-type phase in $MgSiO_3$ and pyrolitic mantle composition. *Earth and Planetary Science Letters* **236,** 914–932 (2005).
6. Matas, J., Bass, J., Ricard, Y., Mattern, E. & Bukowinski, M. S. T. On the bulk composition of the lower mantle: predictions and limitations from generalized inversion of radial seismic profiles. *Geophysical Journal International* **170,** 764–780 (2007).
7. Katsura, T., Yoneda, A., Yamazaki, D., Yoshino, T. & Ito, E. Adiabatic temperature profile in the mantle. *Physics of the Earth and Planetary Interiors* **183,** 212–218 (2010).
8. Katsura, T. A Revised Adiabatic Temperature Profile for the Mantle. *Journal of Geophysical Research: Solid Earth* **127,** e2021JB023562 (2022).
9. Frost, D. J. & McCammon, C. A. The Redox State of Earth's Mantle. *Annual Review of Earth and Planetary Sciences* **36,** 389–420 (2008).
10. *Deep Carbon: Past to Present* (eds Orcutt, B. N., Daniel, I. & Dasgupta, R.) (Cambridge University Press, 2019).
11. Murakami, M., Hirose, K., Sata, N. & Ohishi, Y. Post-perovskite phase transition and mineral chemistry in the pyrolitic lowermost mantle. *Geophysical Research Letters* **32,** L03304 (2005).
12. Irifune, T., Shinmei, T., McCammon, C. A., Miyajima, N., Rubie, D. C. & Frost, D. J. Iron Partitioning and Density Changes of Pyrolite in Earth's Lower Mantle. *Science* **327,** 193–195 (2010).
13. Sinmyo, R. & Hirose, K. Iron partitioning in pyrolitic lower mantle. *Physics and Chemistry of Minerals* **40,** 107–113 (2013).
14. Prescher, C., Langenhorst, F., Dubrovinsky, L. S., Prakapenka, V. B. & Miyajima, N. The effect of Fe spin crossovers on its partitioning behavior and oxidation state in a pyrolitic Earth's lower mantle system. *Earth and Planetary Science Letters* **399,** 86–91 (2014).

15. Piet, H., Badro, J., Nabiei, F., Dennenwaldt, T., Shim, S.-H., Cantoni, M., Hébert, C. & Gillet, P. Spin and valence dependence of iron partitioning in Earth's deep mantle. *Proceedings of the National Academy of Sciences* **113,** 11127–11130 (2016).

16. Shim, S.-H., Grocholski, B., Ye, Y., Alp, E. E., Xu, S., Morgan, D., Meng, Y. & Prakapenka, V. B. Stability of ferrous-iron-rich bridgmanite under reducing midmantle conditions. *Proceedings of the National Academy of Sciences* **114,** 6468–6473 (2017).

17. O'Bannon III., E. F., Jenei, Z., Cynn, H., Lipp, M. J. & Jeffries, J. R. Contributed Review: Culet diameter and the achievable pressure of a diamond anvil cell: Implications for the upper pressure limit of a diamond anvil cell. *Review of Scientific Instruments* **89,** 111501 (2018).

18. Anzellini, S. & Boccato, S. A practical review of the laser-heated diamond anvil cell for university laboratories and synchrotron applications. *Crystals* **10,** 459 (2020).

19. Kaa, J. M., Sternemann, C., Appel, K., Cerantola, V., Preston, T. R., Albers, C., Elbers, M., Libon, L., Makita, M., Pelka, A., Petitgirard, S., Plückthun, C., Roddatis, V., Sahle, C. J., Spiekermann, G., Schmidt, C., Schreiber, A., Sakrowski, R., Tolan, M., Wilke, M., Zastrau, U. & Konôpková, Z. Structural and electron spin state changes in an x-ray heated iron carbonate system at the Earth's lower mantle pressures. *Physical Review Research* **4,** 033042 (2022).

20. Henke, B., Gullikson, E. & Davis, J. X-Ray Interactions: Photoabsorption, Scattering, Transmission, and Reflection at E = 50-30,000 eV, Z = 1-92. *Atomic Data and Nuclear Data Tables* **54,** 181–342 (1993).

21. Bykova, E., Dubrovinsky, L., Dubrovinskaia, N., Bykov, M., McCammon, C., Ovsyannikov, S. V., Liermann, H. P., Kupenko, I., Chumakov, A. I., Rüffer, R., Hanfland, M. & Prakapenka, V. Structural complexity of simple Fe_2O_3 at high pressures and temperatures. *Nature Communications* **7,** 10661 (2016).

22. Cerantola, V., Bykova, E., Kupenko, I., Merlini, M., Ismailova, L., McCammon, C., Bykov, M., Chumakov, A. I., Petitgirard, S., Kantor, I., Svitlyk, V., Jacobs, J., Hanfland, M., Mezouar, M., Prescher, C., Rüffer, R., Prakapenka, V. B. & Dubrovinsky, L. Stability of iron-bearing carbonates in the deep Earth's interior. *Nature Communications* **8,** 15960 (2017).

23. Albers, C., Sakrowski, R., Libon, L., Spiekermann, G., Winkler, B., Schmidt, C., Bayarjargal, L., Cerantola, V., Chariton, S., Giordano, N., Gretarsson, H., Kaa, J., Liermann, H.-P., Sundermann, M., Thiering, N., Tolan, M., Wilke, M. & Sternemann, C. Fe^{3+}-hosting carbon phases in the deep Earth. *Physical Review B* **105,** 085155 (2022).

24. Wilke, M., Farges, F., Petit, P.-E., Brown, G. E. & Martin, F. Oxidation state and coordination of Fe in minerals: An Fe K-XANES spectroscopic study. *American Mineralogist* **86,** 714–730 (2001).

25. Sanson, A., Kantor, I., Cerantola, V., Irifune, T., Carnera, A. & Pascarelli, S. Local structure and spin transition in Fe_2O_3 hematite at high pressure. *Physical Review B* **94,** 014112 (2016).

26. Cerantola, V., Wilke, M., Kantor, I., Ismailova, L., Kupenko, I., McCammon, C., Pascarelli, S. & Dubrovinsky, L. S. Experimental investigation of $FeCO_3$ (siderite) stability in Earth's lower mantle using XANES spectroscopy. *American Mineralogist* **104,** 1083–1091 (2019).

27. Krstulović, M., Rosa, A. D., Biedermann, N., Spiekermann, G., Irifune, T., Muñoz, M. & Wilke, M. Ge coordination in $NaAlGe_3O_8$ glass upon compression to 131 GPa. *Physical Review B* **101,** 214103 (2020).

28. Badro, J., Struzhkin, V. V., Shu, J., Hemley, R. J., Mao, H.-k., Kao, C.-c., Rueff, J.-P. & Shen, G. Magnetism in FeO at Megabar Pressures from X-Ray Emission Spectroscopy. *Physical Review Letters* **83,** 4101–4104 (1999).

29. Spiekermann, G., Harder, M., Gilmore, K., Zalden, P., Sahle, C. J., Petitgirard, S., Wilke, M., Biedermann, N., Weis, C., Morgenroth, W., Tse, J. S., Kulik, E., Nishiyama, N., Yavaş, H. & Sternemann, C. Persistent Octahedral Coordination in Amorphous GeO_2 Up to 100 GPa by Kβ" X-Ray Emission Spectroscopy. *Physical Review X* **9,** 011025 (2019).

30. Weis, C., Spiekermann, G., Sternemann, C., Harder, M., Vankó, G., Cerantola, V., Sahle, C. J., Forov, Y., Sakrowski, R., Kupenko, I., Petitgirard, S., Yavaş, H., Bressler, C., Gawelda, W., Tolan, M. & Wilke, M. Combining X-ray $K\beta_{1,3}$, valence-to-core, and X-ray Raman spectroscopy for studying Earth materials at high pressure and temperature: the case of siderite. *Journal of Analytical Atomic Spectrometry* **34,** 384–393 (2019).

31. Baker, M. L., Mara, M. W., Yan, J. J., Hodgson, K. O., Hedman, B. & Solomon, E. I. K- and L-edge X-ray absorption spectroscopy (XAS) and resonant inelastic X-ray scattering (RIXS) determination of differential orbital covalency (DOC) of transition metal sites. *Coordination Chemistry Reviews* **345,** 182–208 (2017).

32. Sahle, C. J., Rosa, A. D., Rossi, M., Cerantola, V., Spiekermann, G., Petitgirard, S., Jacobs, J., Huotari, S., Sala, M. M. & Mirone, A. Direct tomography imaging for inelastic X-ray scattering experiments at high pressure. *Journal of Synchrotron Radiation* **24,** 269–275 (2017).

33. Weis, C., Sternemann, C., Cerantola, V., Sahle, C. J., Spiekermann, G., Harder, M., Forov, Y., Kononov, A., R., S., Yavaş, H., Tolan, M. & Wilke, M. Pressure driven spin transition in siderite and magnesiosiderite single crystals. *Scientific Reports* **7,** 16526 (2017).

34. Lavina, B., Dera, P., Downs, R. T., Yang, W., Sinogeikin, S., Meng, Y., Shen, G. & Schiferl, D. Structure of siderite $FeCO_3$ to 56 GPa and hysteresis of its spin-pairing transition. *Physical Review B* **82,** 064110 (2010).

35. Lin, J.-F., Liu, J., Jacobs, C. & Prakapenka, V. B. Vibrational and elastic properties of ferromagnesite across the electronic spin-pairing transition of iron. *American Mineralogist* **97,** 583–591 (2012).

36. Farfan, G., Wang, S., Ma, H., Caracas, R. & Mao, W. L. Bonding and structural changes in siderite at high pressure. *American Mineralogist* **97,** 1421–1426 (2012).

37. Cerantola, V., McCammon, C., Kupenko, I., Kantor, I., Marini, C., Wilke, M., Ismailova, L., Solopova, N., Chumakov, A., Pascarelli, S. & Dubrovinsky, L. High-pressure spectroscopic study of siderite ($FeCO_3$) with a focus on spin crossover. *American Mineralogist* **100,** 2670–2681 (2015).

38. Müller, J., Speziale, S., Efthimiopoulos, I., Jahn, S. & Koch-Müller, M. Raman spectroscopy of siderite at high pressure: Evidence for a sharp spin transition. *American Mineralogist* **101,** 2638–2644 (2016).

39. Stekiel, M., Girard, A., Nguyen-Thanh, T., Bosak, A., Milman, V. & Winkler, B. Phonon-driven phase transitions in calcite, dolomite, and magnesite. *Physical Review B* **99,** 054101 (2019).

40. Boulard, E., Gloter, A., Corgne, A., Antonangeli, D., Auzende, A.-L., Perrillat, J.-P., Guyot, F. & Fiquet, G. New host for carbon in the deep Earth. *Proceedings of the National Academy of Sciences* **108,** 5184–5187 (2011).

41. Liu, J., Lin, J. F. & Prakapenka, V. B. High-Pressure Orthorhombic Ferromagnesite as a Potential Deep-Mantle Carbon Carrier. *Scientific Reports* **5,** 3–8 (2015).

42. Greenberg, E., Leonov, I., Layek, S., Konôpková, Z., Pasternak, M. P., Dubrovinsky, L., Jeanloz, R., Abrikosov, I. A. & Rozenberg, G. K. Pressure-Induced Site-Selective Mott Insulator-Metal Transition in Fe_2O_3. *Physical Review X* **8,** 031059 (2018).

43. Yagi, T., Suzuki, T. & Akimoto, S.-I. Static compression of wüstite ($Fe_{0.98}O$) to 120 GPa. *Journal of Geophysical Research: Solid Earth* **90,** 8784–8788 (1985).

44. Jacobsen, S. D., Lin, J.-F., Angel, R. J., Shen, G., Prakapenka, V. B., Dera, P., Mao, H.-K. & Hemley, R. J. SXD at Mbar pressures Synchrotron Radiation Single-crystal synchrotron X-ray diffraction study of wü stite and magnesiowüstite at lower-mantle pressures. *J. Synchrotron Rad* **12,** 577–583 (2005).

45. Vankó, G., Neisius, T., Molnár, G., Renz, F., Kárpáti, S., Shukla, A. & de Groot, F. M. F. Probing the 3d Spin Momentum with X-ray Emission Spectroscopy: The Case of Molecular-Spin Transitions. *The Journal of Physical Chemistry B* **110,** 11647–11653 (2006).

46. Albers, C., Sakrowski, R., Thiering, N., Libon, L., Spiekermann, G., Kaa, J. M., Gretarsson, H., Sundermann, M., Tolan, M., Wilke, M. & Sternemann, C. High-efficiency X-ray emission spectroscopy of cold-compressed Fe_2O_3 and laser-heated pressurized $FeCO_3$ using a von Hámos spectrometer. *Journal of Analytical Atomic Spectrometry* **38,** 1097–1107 (2023).

47. Albers, C., Thiering, N., Sakrowski, R., Gretarsson, H., Kaa, J., Sundermann, M., Tolan, M., Wilke, M. & Sternemann, C. Non-resonant and resonant X-ray emission at high pressure using a von Hámos setup: the case of FeO. *Journal of Physics: Conference Series* **2380,** 012128 (2022).

48. De Groot, F. & Kotani, A. *Core level spectroscopy of solids* 1st ed. (2008).

49. Kotani, A. & Shin, S. Resonant inelastic x-ray scattering spectra for electrons in solids. *Reviews of Modern Physics* **73,** 203–246 (2001).

50. Chemical dependence of interatomic X-ray transition energies and intensities – a study of Mn Kβ'' and K$\beta_{2,5}$ spectra. *Chemical Physics Letters* **302,** 119–124 (1999).

51. Lin, J.-F., Speziale, S., Mao, Z. & Marquardt, H. Effects of the electronic spin transitions of iron in lower mantle minerals: Implicantions for deep mantle geophysics and geochemistry. *Reviews of Geophysics* **51,** 244–275 (2013).

52. Westre, T. E., Kennepohl, P., DeWitt, J. G., Hedman, B., Hodgson, K. O. & Solomon, E. I. A Multiplet Analysis of Fe K-Edge 1s → 3d Pre-Edge Features of Iron Complexes. *Journal of the American Chemical Society* **119,** 6297–6314 (1997).

53. Li, J., Struzhkin, V. V., Mao, H.-k., Shu, J., Hemley, R. J., Fei, Y., Mysen, B., Dera, P., Prakapenka, V. & Shen, G. Electronic spin state of iron in lower mantle perovskite. *Proceedings of the National Academy of Sciences* **101,** 14027–14030 (2004).

54. Li, L., Brodholt, J. P., Stackhouse, S., Weidner, D. J., Alfredsson, M. & Price, G. D. Electronic spin state of ferric iron in Al-bearing perovskite in the lower mantle. *Geophysical Research Letters* **32,** L17307 (2005).

55. Li, J., Sturhahn, W., Jackson, J. M., Struzhkin, V. V., Lin, J. F., Zhao, J., Mao, H. K. & Shen, G. Pressure effect on the electronic structure of iron in $(Mg,Fe)(Si,Al)O_3$ perovskite: A combined synchrotron Mössbauer and X-ray emission spectroscopy study up to 100 GPa. *Physics and Chemistry of Minerals* **33,** 575–585 (2006).

56. McCammon, C., Glazyrin, K., Kantor, A., Kantor, I., Kupenko, I., Narygina, O., Potapkin, V., Prescher, C., Sinmyo, R., Chumakov, A., Rüffer, R., Sergueev, I., Smirnov, G. & Dubrovinsky, L. Iron spin state in silicate perovskite at conditions of the Earth's deep interior. *High Pressure Research* **33,** 663–672 (2013).

57. Boehler, R. New diamond cell for single-crystal x-ray diffraction. *Review of Scientific Instruments* **77,** 115103 (2006).

58. Kantor, I., Prakapenka, V., Kantor, A., Dera, P., Kurnosov, A., Sinogeikin, S., Dubrovinskaia, N. & Dubrovinsky, L. BX90: A new diamond anvil cell design for X-ray diffraction and optical measurements. *Review of Scientific Instruments* **83,** 125102 (2012).

59. Petitgirard, S., Spiekermann, G., Weis, C., Sahle, C., Sternemann, C. & Wilke, M. Miniature diamond anvils for X-ray Raman scattering spectroscopy experiments at high pressure. *Journal of Synchrotron Radiation* **24,** 276–282 (2017).

60. Li, B., Ji, C., Yang, W., Wang, J., Yang, K., Xu, R., Liu, W., Cai, Z., Chen, J. & Mao, H.-k. Diamond anvil cell behavior up to 4 Mbar. *Proceedings of the National Academy of Sciences* **115,** 1713–1717 (2018).

61. Dubrovinsky, L., Dubrovinskaia, N., Prakapenka, V. B. & Abakumov, A. M. Implementation of micro-ball nanodiamond anvils for high-pressure studies above 6 Mbar. *Nature Communications* **3,** 1163 (2012).

62. Sakai, T., Yagi, T., Ohfuji, H., Irifune, T., Ohishi, Y., Hirao, N., Suzuki, Y., Kuroda, Y., Asakawa, T. & Kanemura, T. High-pressure generation using double stage micro-paired diamond anvils shaped by focused ion beam. *Review of Scientific Instruments* **86,** 033905 (2015).

63. Dubrovinsky, L., Dubrovinskaia, N., Bykova, E., Bykov, M., Prakapenka, V., Prescher, C., Glazyrin, K., Liermann, H. P., Ekholm, M., Feng, Q., Pourovskii, L. V., Katsnelson, M. I., Wills, J. M. & Abrikosov, I. A. The most incompressible metal osmium at static pressures above 750 gigapascals. *Nature* **525,** 226–229 (2015).

64. Lobanov, S. S., Prakapenka, V. B., Prescher, C., Konôpková, Z., Liermann, H.-P., Crispin, K. L., Zhang, C. & Goncharov, A. F. Pressure, stress, and strain distribution in the double-stage diamond anvil cell. *Journal of Applied Physics* **118,** 035905 (2015).

65. Dewaele, A., Loubeyre, P., Occelli, F., Marie, O. & Mezouar, M. Toroidal diamond anvil cell for detailed measurements under extreme static pressures. *Nature Communications* **9,** 2913 (2018).

66. Angel, R. J., Bujak, M., Zhao, J., Gatta, G. D. & Jacobsen, S. D. Effective hydrostatic limits of pressure media for high-pressure crystallographic studies. *Journal of Applied Crystallography* **40,** 26–32 (2007).

67. Dewaele, A. & Loubeyre, P. Pressurizing conditions in helium-pressure-transmitting medium. *High Pressure Research* **27,** 419–429 (2007).

68. Klotz, S., Chervin, J.-C., Munsch, P. & Marchand, G. L. Hydrostatic limits of 11 pressure transmitting media. *Journal of Physics D: Applied Physics* **42,** 075413 (2009).

69. Mills, R. L., Liebenberg, D. H., Bronson, J. C. & Schmidt, L. C. Procedure for loading diamond cells with high-pressure gas. *Review of Scientific Instruments* **51,** 891–895 (2008).

70. Fei, Y., Ricolleau, A., Frank, M., Mibe, K., Shen, G. & Prakapenka, V. Toward an internally consistent pressure scale. *Proceedings of the National Academy of Sciences* **104,** 9182–9186 (2007).

71. Hanfland, M. & Syassen, K. A Raman study of diamond anvils under stress. *Journal of Applied Physics* **57,** 2752–2756 (1985).

72. Akahama, Y. & Kawamura, H. Pressure calibration of diamond anvil Raman gauge to 310GPa. *Journal of Applied Physics* **100,** 043516 (2006).

73. Nuclear resonant scattering at PETRA III: Brillant opportunities for nano - And extreme condition science. *Journal of Physics: Conference Series* **217,** 012008 (2010).

74. V. Hámos, L. Röntgenspektroskopie und Abbildung mittels gekrümmter Kristallreflektoren. I. Geometrisch-optische Betrachtungen. *Annalen der Physik* **409,** 716–724 (1933).

75. Lafuerza, S., Carlantuono, A., Retegan, M. & Glatzel, P. Chemical Sensitivity of Kβ and Kα X-ray Emission from a Systematic Investigation of Iron Compounds. *Inorganic Chemistry* **59,** 12518–12535 (2020).

76. Kotani, A. Theory of resonant X-ray emission spectra in strongly correlated electron systems. *Journal of Electron Spectroscopy and Related Phenomena* **110-111,** 197–212 (2000).

77. Idé, T. & Kotani, A. Interplay between Raman and Fluorescence-Like Components in Resonant X-ray Emission Spectra of Degenerate d^0 and d^1 Systems. *Journal of the Physical Society of Japan* **69,** 1895 (2000).

78. Rueff, J.-P., Journel, L., Petit, P.-E. & Farges, F. Fe K pre-edges as revealed by resonant x-ray emission. *Physical Review B* **69,** 235107 (2004).

79. Vankó, G., de Groot, F. M. F., Huotari, S., Cava, R. J., Lorenz, T. & Reuther, M. Intersite 4p-3d hybridization in cobalt oxides: a resonant x-ray emission spectroscopy study. *arXiv* **0802.2744** (2008).

80. Glatzel, P., Mirone, A., Eeckhout, S. G., Sikora, M. & Giuli, G. Orbital hybridization and spin polarization in the resonant $1s$ photoexcitations of $\alpha{-}Fe_2O_3$. *Physical Review B* **77,** 115133 (2008).

81. Fukao, Y., Widiyantoro, S. & Obayashi, M. Stagnant slabs in the upper and lower mantle transition region. *Reviews of Geophysics* **39,** 291–323 (2001).

82. Walter, M. J., Kohn, S. C., Araujo, D., Bulanova, G. P., Smith, C. B., Gaillou, E., Wang, J., Steele, A. & Shirey, S. B. Deep mantle cycling of oceanic crust: Evidence from diamonds and their mineral inclusions. *Science* **334,** 54–57 (2011).

83. Liu, J., Lin, J. F., Mao, Z. & Prakapenka, V. B. Thermal equation of state and spin transition of magnesiosiderite at high pressure and temperature. *American Mineralogist* **99,** 84–93 (2014).

84. Spiekermann, G., Kupenko, I., Petitgirard, S., Harder, M., Nyrow, A., Weis, C., Albers, C., Biedermann, N., Libon, L., Sahle, C. J., Cerantola, V., Glazyrin, K., Konôpková, Z., Sinmyo, R., Morgenroth, W., Sergueev, I., Yavaş, H., Dubrovinsky, L., Tolan, M., Sternemann, C. & Wilke, M. A portable on-axis laser-heating system for near-90° X-ray spectroscopy: application to ferropericlase and iron silicide. *Journal of Synchrotron Radiation* **27,** 414–424 (2020).

85. Bayarjargal, L., Fruhner, C.-J., Schrodt, N. & Winkler, B. $CaCO_3$ phase diagram studied with Raman spectroscopy at pressures up to 50 GPa and high temperatures and DFT modeling. *Physics of the Earth and Planetary Interiors* **281,** 31–45 (2018).

86. *T-Rax* <`http://www.clemensprescher.com/programs/t-rax`> (2020).

87. Larkin, P. *Infrared and Raman Spectroscopy* (Elsevier, 2011).

88. Jayaraman, A. & Shamka, S. Role of Raman spectroscopy in high pressure research. *Current Science* **74,** 308–316 (1998).

89. Goncharov, A. F. Raman Spectroscopy at High Pressures. *International Journal of Spectroscopy* **2012,** 617528 (2012).

90. Rividi, N., van Zuilen, M., Philippot, P., Ménez, B., Godard, G. & Poidatz, E. Calibration of Carbonate Composition Using Micro-Raman Analysis: Application to Planetary Surface Exploration. *Astrobiology* **10,** 293–309 (2010).

91. Zhao, C., Xu, L., Gui, W. & Liu, J. Phase stability and vibrational properties of iron-bearing carbonates at high pressure. *Minerals* **10,** 1142 (2020).

92. Boulard, E., Guyot, F. & Fiquet, G. The influence on Fe content on Raman spectra and unit cell parameters of magnesite-siderite solid solutions. *Physics and Chemistry of Minerals* **39,** 239–246 (2012).

93. Kopitzki, K. & Herzog, P. *Einführung in die Festkörperphysik* (Springer Berlin Heidelberg, 2017).

94. Li, Z. & Stackhouse, S. Iron-rich carbonates stabilized by magnetic entropy at lower mantle conditions. *Earth and Planetary Science Letters* **531,** 115959 (2020).

95. Spahr, D., Binck, J., Bayarjargal, L., Luchitskaia, R., Morgenroth, W., Comboni, D., Milman, V. & Winkler, B. Tetrahedrally Coordinated sp^3 -Hybridized Carbon in Sr_2CO_4 Orthocarbonate at Ambient Conditions. *Inorganic Chemistry* **60,** 5419–5422 (2021).

96. Dobson, D. P. & Brodholt, J. P. Subducted banded iron formations as a source of ultralow-velocity zones at the core–mantle boundary. *Nature* **434,** 371–374 (2005).

97. Kupenko, I., Aprilis, G., Vasiukov, D. M., McCammon, C., Chariton, S., Cerantola, V., Kantor, I., Chumakov, A. I., Rüffer, R., Dubrovinsky, L. & Sanchez-Valle, C. Magnetism in cold subducting slabs at mantle transition zone depths. *Nature* **570,** 102–106 (2019).

98. Olsen, J. S., Cousins, C. S., Gerward, L., Jhans, H. & Sheldon, B. J. A study of the crystal structure of Fe_2O_3 in the pressure range up to 65 gpa using synchrotron radiation. *Physica Scripta* **43,** 327–330 (1991).

99. Pasternak, M. P., Rozenberg, G. K., Machavariani, G. Y., Naaman, O., Taylor, R. D. & Jeanloz, R. Breakdown of the Mott-Hubbard State in Fe_2O_3: A First-Order Insulator-Metal Transition with Collapse of Magnetism at 50 GPa. *Physical Review Letters* **82,** 4663–4666 (1999).

100. Badro, J., Fiquet, G., Struzhkin, V. V., Somayazulu, M., Mao, H.-k., Shen, G. & Le Bihan, T. Nature of the High-Pressure Transition in Fe_2O_3 Hematite. *Physical Review Letters* **89,** 205504 (2002).

101. Rozenberg, G. K., Dubrovinsky, L. S., Pasternak, M. P., Naaman, O., Le Bihan, T. & Ahuja, R. High-pressure structural studies of hematite Fe_2O_3. *Physical Review B* **65,** 064112 (2002).

102. Liu, H., Caldwell, A., Benedetti, L. R., Panero, W. & Jeanloz, R. Static compression of α-Fe_2O_3: linear incompressibility of lattice parameters and high-pressure transformations. *Physics and Chemistry of Minerals* **30,** 582–588 (2003).

103. Ono, S., Kikegawa, T. & Ohishi, Y. High-pressure phase transition of hematite, Fe_2O_3. *Journal of Physics and Chemistry of Solids* **65,** 1527–1530 (2004).

104. Yamaoka, H., Oura, M., Taguchi, M., Morikawa, T., Takahiro, K., Terai, A., Kawatsura, K., M. Vlaicu, A., Ito, Y. & Mukoyama, T. Kβ Resonant X-ray Emission Spectroscopy for Fe, Fe_2O_3 and Fe_3O_4. *Journal of the Physical Society of Japan* **73,** 3182–3191 (2004).

105. Kozhevnikov, A. V., Lukoyanov, A. V., Anisimov, V. I. & Korotin, M. A. Transition of iron ions from high-spin to low-spin state and pressure-induced insulator-metal transition in hematite Fe_2O_3. *Journal of Experimental and Theoretical Physics* **105,** 1035–1042 (2007).

106. Shim, S.-H., Bengtson, A., Morgan, D., Sturhahn, W., Catalli, K., Zhao, J., Lerche, M. & Prakapenka, V. Electronic and magnetic structures of the postperovskite-type Fe_2O_3 and implications for planetary magnetic records and deep interiors. *Proceedings of the National Academy of Sciences* **106,** 5508–5512 (2009).

107. Ito, E., Fukui, H., Katsura, T., Yamazaki, D., Yoshino, T., Aizawa, Y. I., Kubo, A., Yokoshi, S., Kawabe, K., Zhai, S., Shatzkiy, A., Okube, M., Nozawa, A. & Funakoshi, K. I. Determination of high-pressure Phase equilibria of Fe_2O_3 using the Kawai-type apparatus equipped with sintered diamond anvils. *American Mineralogist* **94,** 205–209 (2009).

108. Dubrovinsky, L., Boffa-Ballaran, T., Glazyrin, K., Kurnosov, A., Frost, D., Merlini, M., Hanfland, M., Prakapenka, V. B., Schouwink, P., Pippinger, T. & Dubrovinskaia, N. Single-crystal X-ray diffraction at megabar pressures and temperatures of thousands of degrees. *High Pressure Research* **30,** 620–633 (2010).

109. Bykova, E., Bykov, M., Prakapenka, V., Konôpková, Z., Liermann, H.-P., Dubrovinskaia, N. & Dubrovinsky, L. Novel high pressure monoclinic Fe_2O_3 polymorph revealed by single-crystal synchrotron X-ray diffraction studies. *High Pressure Research* **33,** 534–545 (2013).

110. Tuček, J., Machala, L., Ono, S., Namai, A., Yoshikiyo, M., Imoto, K., Tokoro, H., Ohkoshi, S. I. & Zbořil, R. Zeta-Fe_2O_3 – A new stable polymorph in iron(III) oxide family. *Scientific Reports* **5,** 15091 (2015).

111. Nowakowski, M., Czapla-Masztafiak, J., Szlachetko, J. & Kwiatek, W. M. Electronic structure of Fe, α-Fe_2O_3 and $Fe(NO_3)_3{\times}9\ H_2O$ determined using RXES. *Chemical Physics* **493,** 49–55 (2017).

112. Müller, J., Efthimiopoulos, I., Jahn, S. & Koch-Müller, M. Effect of temperature on the pressure-induced spin transition in siderite and iron-bearing magnesite: a Raman spectroscopy study. *European Journal of Mineralogy* **29,** 785–793 (2017).

113. Maslen, E. N., Streltsov, V. A., Streltsova, N. R., Ishizawa, N. & Satow, Y. Synchrotron X-ray study of the electron density in α-Al_2O_3. *Acta Crystallographica Section B* **49,** 973–980 (1993).

114. Caliebe, W. *Inelastic X-Ray Scattering with High Energy Resolution* PhD thesis (Christian-Albrechts Universit zu Kiel, 1997).

115. Dräger, G., Frahm, R., Materlik, G. & Brümmer, O. On the Multipole Character of the X-Ray Transitions in the Pre-Edge Structure of Fe K Absorption Spectra. An Experimental Study. *physica status solidi (b)* **146,** 287–294 (1988).

116. Al Samarai, M., Ulises Delgado-Jaime, M., Ishii, H., Hiraoka, N., Tsuei, K.-D., Rueff, J.-P., Lassale-Kaiser, B., Weckhuysen, B. M. & de Groot, F. M. 1s3p Resonant Inelastic X-ray Scattering of Cobalt Oxides and Sulfides. **120,** 24063–24069 (2016).

117. Boulard, E., Harmand, M., Guyot, F., Lelong, G., Morard, G., Cabaret, D., Boccato, S., Rosa, A. D., Briggs, R., Pascarelli, S. & Fiquet, G. Ferrous Iron Under Oxygen-Rich Conditions in the Deep Mantle. *Geophysical Research Letters* **46,** 1348–1356 (2019).

118. Glatzel, P., Sikora, M. & Fernández-García, M. Resonant X-ray spectroscopy to study K absorption pre-edges in 3d transition metal compounds. *European Physical Journal: Special Topics* **169,** 207–214 (2009).

119. Murakami, M., Hirose, K., Kawamura, K., Sata, N. & Ohishi, Y. Post-perovskite phase transition in $MgSiO_3$. *Science* **304,** 855–858 (2004).

120. Goncharov, A. F., Struzhkin, V. V. & Jacobsen, S. D. Reduced radiative conductivity of low-spin (Mg,Fe)O in the lower mantle. *Science* **312,** 1205–1208 (2006).

121. Keppler, H., Kantor, I. & Dubrovinsky, L. S. Optical absorption spectra of ferropericlase to 84 GPa. *American Mineralogist* **92,** 433–436 (2007).

122. Schifferle, L. & Lobanov, S. S. Evolution of Chemical Bonding and Spin-Pairing Energy in Ferropericlase across Its Spin Transition. *ACS Earth and Space Chemistry* **6,** 788–799 (2022).

123. Speziale, S., Milner, A., Lee, V. E., Clark, S. M., Pasternak, M. P. & Jeanloz, R. Iron spin transition in Earth's mantle. *Proceedings of the National Academy of Sciences* **102,** 17918–17922 (2005).

124. Gavriliuk, A. G., Lin, J. F., Lyubutin, I. S. & Struzhkin, V. V. Optimization of the conditions of synchrotron Mössbauer experiment for studying electronic transitions at high pressures by the example of (Mg, Fe)O magnesiowustite. *JETP Letters* **84,** 161–166 (2006).

125. Kantor, I. Y., Dubrovinsky, L. S. & McCammon, C. A. Spin crossover in (Mg, Fe)O: A Mössbauer effect study with an alternative interpretation of x-ray emission spectroscopy data. *Physical Review B* **73,** 100101 (2006).

126. Lin, J.-F., Gavriliuk, A. G., Struzhkin, V. V., Jacobsen, S. D., Sturhahn, W., Hu, M. Y., Chow, P. & Yoo, C.-S. Pressure-induced electronic spin transition of iron in magnesiowustite-(Mg, Fe)O. *Physical Review B* **73,** 113107 (2006).

127. Lyubutin, I. S., Gavriliuk, A. G., Frolov, K. V., Lin, J. F. & Troyan, I. A. High-spin-low-spin transition in magnesiowüstite $(Mg_{0.75},Fe_{0.25})O$ at high pressures under hydrostatic conditions. *JETP Letters* **90,** 617–622 (2010).

128. Solomatova, N. V., Jackson, J. M., Sturhahn, W., Wicks, J. K., Zhao, J., Toellner, T. S., Kalkan, B. & Steinhardt, W. M. Equation of state and spin crossover of (Mg,Fe)O at high pressure, with implications for explaining topographic relief at the core-mantle boundary. *American Mineralogist* **101,** 1084–1093 (2016).

129. Hamada, M., Kamada, S., Ohtani, E., Sakamaki, T., Mitsui, T., Masuda, R., Hirao, N., Ohishi, Y. & Akasaka, M. Synchrotron Mössbauer spectroscopic and x-ray diffraction study of ferropericlase in the high-pressure range of the lower mantle region. *Physical Review B* **103,** 174108 (2021).

130. Badro, J., Fiquet, G., Guyot, F., Rueff, J.-P., Struzhkin, V. V., Vankó, G. & Monaco, G. Iron Partitioning in Earth's Mantle: Toward a Deep Lower Mantle Discontinuity. *Science* **300,** 789–791 (2003).

131. Lin, J. F., Struzhkin, V. V., Jacobsen, S. D., Hu, M. Y., Chow, P., Kung, J., Liu, H., Mao, H.-K. & Hemley, R. J. Spin transition of iron in magnesiowüstite in the Earth's lower mantle. *Nature* **436,** 377–380 (2005).

132. Lin, J.-F., Vankó, G., Jacobsen, S. D., Iota, V., Struzhkin, V. V., Prakapenka, V. B., Kuznetsov, A. & Yoo, C.-S. Spin Transition Zone in Earth's Lower Mantle. *Science* **317,** 1740–1743 (2007).

133. Lin, J.-F., Mao, Z., Jarrige, I., Xiao, Y., Chow, P., Okuchi, T., Hiraoka, N. & Jacobsen, S. D. Resonant X-ray emission study of the lower-mantle ferropericlase at high pressures. *American Mineralogist* **95,** 1125–1131 (2010).

134. Ozawa, H., Hirose, K., Ohta, K., Ishii, H., Hiraoka, N., Ohishi, Y. & Seto, Y. Spin crossover, structural change, and metallization in NiAs-type FeO at high pressure. *Physical Review B* **84,** 134417 (2011).

135. Hamada, M., Kamada, S., Ohtani, E., Mitsui, T., Masuda, R., Sakamaki, T., Suzuki, N., Maeda, F. & Akasaka, M. Magnetic and spin transitions in wüstite: A synchrotron Mössbauer spectroscopic study. *Physical Review B* **93,** 155165 (2016).

136. Pasternak, M. P., Taylor, R. D., Jeanloz, R., Li, X., Nguyen, J. H. & McCammon, C. A. High Pressure Collapse of Magnetism in $Fe_{0.94}O$: Mössbauer Spectroscopy Beyond 100 GPa. *Physical Review Letters* **79,** 5046–5049 (1997).

137. Fei, Y. & Mao, H.-k. In Situ Determination of the NiAs Phase of FeO at High Pressure and Temperature. *Science* **266,** 1678–1680 (1994).

138. Mao, H.-k., Shu, J., Fei, Y., Hu, J. & Hemley, R. J. The wüstite enigma. *Physics of the Earth and Planetary Interiors* **96,** 135–145 (1996).

139. Fischer, R. A., Campbell, A. J., Shofner, G. A., Lord, O. T., Dera, P. & Prakapenka, V. B. Equation of state and phase diagram of FeO. *Earth and Planetary Science Letters* **304,** 496–502 (2011).

140. Kalinko, A., Caliebe, W. A., Schoch, R. & Bauer, M. A von Hamos-type hard X-ray spectrometer at the PETRA III beamline P64. *Journal of Synchrotron Radiation* **27,** 31–36 (2020).

141. Karpishin, T. B., Stack, T. D. P. & Raymond, K. N. Octahedral vs Trigonal Prismatic Geometry in a Series of Catechol Macrobicyclic Ligand-Metal Complexes. *American Chemical Society* **115,** 182–192 (1993).

142. Schouwink, P., Dubrovinsky, L., Glazyrin, K., Merlini, M., Hanfland, M., Pippinger, T. & Miletich, R. High-pressure structural behavior of α-Fe_2O_3 studied by single-crystal X-ray diffraction and synchrotron radiation up to 25 GPa. *American Mineralogist* **96,** 1781–1786 (2011).

143. Sahle, C. J., Mirone, A., Niskanen, J., Inkinen, J., Krisch, M. & Huotari, S. Planning, performing and analyzing X-ray Raman scattering experiments. *Journal of Synchrotron Radiation* **22,** 400–409 (2015).

144. Fei, Y. Crystal chemistry of FeO at high pressure and temperature. *Mineral spectroscopy: a tribute to Roger Burns,* 243–254 (1996).

List of acronyms

BA	Boehler-Almax diamond
CEE	constant emission energy
CIE	constant incident energy
CMB	core-mantle boundary
COG	center of gravity
DAC	diamond anvil cell
DDSCS	double differential scattering cross section
DESY	Deutsches Elektronen-Synchrotron
DFT	density functional theory
EELS	electron energy loss spectroscopy
EOS	equation of state
EXAFS	extended x-ray absorption fine structure
FP	ferropericlase
FWHM	Full width at half maximun
GFZ	Deutsches GeoForschungsZentrum
HERFD	high-energy-resolution fluorescence-detected
HP	high pressure
HS	high spin
IAD	integral of absolute difference
IS	intermediate spin
LP	low pressure
LS	low spin
MD	mini diamond
ROI	region of interest
RXES	resonant X-ray emission spectroscopy
SI	supplementary information
SNR	signal-to-noise ratio
SP	silicate perovskite
ST	standard diamond
VTC	valence-to-core
XANES	X-ray absorption near-edge structure
XAS	X-ray absorption spectroscopy
XES	X-ray emission spectroscopy
XRD	X-ray diffraction

Publications and conference contributions

Publications as first author

- **C. Albers**, R. Sakrowski, N. Thiering, L. Libon, G. Spiekermann, J.M. Kaa, H. Gretarsson, M. Sundermann, M. Tolan, M. Wilke and C. Sternemann. "High-efficiency X-ray emission spectroscopy of cold-compressed Fe_2O_3 and laser-heated pressurized $FeCO_3$ using a von Hámos spectrometer" *Journal of Analytical Atomic Spectrometry* 38, 1097-1107 (2023)

- **C. Albers**, N. Thiering, R. Sakrowski, H. Gretarsson, J. Kaa, M. Sundermann, M. Tolan, M. Wilke, and C. Sternemann. "Non-resonant and resonant X-ray emission at high pressure using a von Hámos setup: the case of FeO" *Journal of Physics: Conference Series* 23808, 012128 (2022)

- **C. Albers**, R. Sakrowski, L. Libon, G. Spiekermann, B. Winkler, C. Schmidt, L. Bayarjargal, V. Cerantola, S. Chariton, N. Giordano, H. Gretarsson, J. Kaa, H.-P. Liermann, M. Sundermann, N. Thiering, M. Tolan, M. Wilke, and C. Sternemann. "Fe^{3+}-hosting carbon phases in the deep Earth" *Physical Review B* 105, 085155 (2022)

Publications as co-author

- J. M. Kaa, Z. Konôpková, T. R. Preston, V. Cerantola, C. J. Sahle, M. Förster, **C. Albers**, L. Libon, R. Sakrowski, L. Wollenweber, K. Buakor, A. Dwivedi, M. Mishchenko, M. Nakatsutsumi, C. Plückthun, J.-P. Schwinkendorf, G. Spiekermann, N. Thiering, S. Petitgirard, M. Tolan, M. Wilke, U. Zastrau, K. Appel and C. Sternemann "A von Hámos spectrometer for diamond anvil cell experiments at the High Energy Density Instrument of the European X-ray Free-Electron Laser" *Journal of Synchrotron Radiation* 30, 822-830 (2023)

- J.M. Kaa, C. Sternemann, K. Appel, V. Cerantola, T.R. Preston, **C. Albers**, M. Elbers, L. Libon, M. Makita, A. Pelka, S. Petitgirard, C. Plückthun, V. Roddatis, C.J. Sahle, G. Spiekermann, C. Schmidt, A. Schreiber, R. Sakrowski, M. Tolan, M. Wilke, U. Zastrau, and Z. Konôpková. "Structural and electron spin state changes in an x-ray heated iron carbonate system at the Earth's lower mantle pressures" *Physical Review Research* 4, 033042 (2022)

- M. Krstulović, A.D.Rosa, D. Ferreira Sanchez, L. Libon, **C. Albers**, M. Merkulova, D. Grolimund,T. Irifune, M.Wilke. "Effect of temperature on the densification of silicate melts to lower Earth's mantle conditions" *Physics of the Earth and Planetary Interiors* 323, 106823 (2022)

- G. Spiekermann, L. Libon, **C. Albers**, R. Sakrowski, S. Petitgirard, Ch.J. Sahle, M. Sundermann, H. Gretarsson, I. Sergueev, C. Sternemann, M. Wilke, and M. Murakami. "Reflective imaging, on-axis laser heating and radiospectrometry of samples in diamond anvil cells with a parabolic mirror" *High Pressure Research* 41, 142 (2021)
- G. Spiekermann, I. Kupenko, S. Petitgirard, M. Harder, A. Nyrow, C. Weis, **C. Albers**, N. Biedermann, L. Libon, C.J. Sahle, V. Cerantola, K. Glazyrin, Z. Konôpková, R. Sinmyo, W. Morgenroth, I. Sergueev, H. Yavaş, L. Dubrovinsky, M. Tolan, C. Sternemann and M. Wilke. "A portable on-axis laser-heating system for near-90° X-ray spectroscopy: application to ferropericlase and iron silicide" *Journal of Synchrotron Radiation* 27, 414 (2020)
- S. Dogan-Surmeier, F. Gruber, S. Bieder, P. Schlenz, M. Paulus, C. Albers, E. Schneider, N. Thiering, C. Maurer, M. Tolan "Towards in-line real-time characterization of roll-to-roll produced ZTO/Ag/ITO thin films by hyperspectral imaging" *Journal of Physics D: Applied Physics* 56, 3651102 (2023)
- G. Surmeier, S. Dogan-Surmeier, M. Paulus, **C. Albers**, J. Latarius, C. Sternemann, E. Schneider, M. Tolan, J. Nase "The interaction of viral fusion peptides with lipid membranes" *Biophysical Journal* 121, 3811 (2022)
- J. Bolle, S.P. Bierwirth, M. Požar, A. Perera, M. Paulus, P. Münzner, **C. Albers**, S. Dogan, M. Elbers, R. Sakrowski, G. Surmeier, R. Böhmer, M. Tolan, and C. Sternemann "Isomeric effects in structure formation and dielectric dynamics of different octanols" *Physical Chemistry Chemical Physics* 23, 24211 (2021)
- M. Elbers, C. Schmidt, C. Sternemann, C.J. Sahle, S. Jahn, **C. Albers**, R. Sakrowski, H. Gretarsson, M. Sundermann, M. Tolan, and M. Wilke "Ion association in hydrothermal aqueous NaCl solutions: implications for the microscopic structure of supercritical water" *Physical Chemistry Chemical Physics* 23, 14845 (2021)
- Y. Forov, M. Paulus, S. Dogan, P. Salmen, C. Weis, T. Gahlmann, A. Behrendt, **C. Albers**, M. Elbers, W. Schnettger, S. Egger, E. Zwar, H. Rehage, I. Kiesel, T. Riedl, and M. Tolan "The adsorption behavior of lysozyme at titanium oxide-water interfaces" *Langmuir* 34, 5403 (2018)

Conference contributions as presenting author

- DPG - Spring conference (Deutsche Physikalische Gesellschaft e.V., Germany) - "Formation and electronic structure of tetracarbonates under extreme conditions" (04/2019) - poster
- 57th European High Pressure Research Group Meeting on High Pressure Science and Technology (09/2019, Prag) - "Formation and electronic structure of tetracarbonate-sunder extreme conditions" poster
- 5th YES Congress 2019 (Young Earth Scientists Network) - "A portable setup to establish extreme conditions for the study of tetracarbonates – first results on the electronic structure" (09/2019) - talk
- Desy Users' meeting 2020 "Formation and electronic structure of tetracarbonates under extreme conditions" (01/2020) - poster
- XAFS 2021 "X-ray emission scanning imaging setup to study electronic structure of iron bearing compounds in situ at conditions of the Earth's mantle" (07/2021) - poster
- DPG - Virtual conference (Deutsche Physikalische Gesellschaft e.V., Germany) - "X-ray emission scanning imaging setup to study electronic structure of iron bearing compounds in-situ at conditions of the Earth's mantle" (09/2021) - poster
- Delta seminar "Iron's spin state in tetracarbonates under conditions of the deep Earth - Eisen-Spinzustand in Tetrakarbonaten unter Bedingungen des tiefen Erdmantels" - talk
- SRI 2021 "X-ray emission scanning imaging setup to study electronic structure of iron-bearing compounds in situ at conditions of the Earth's mantle" (03/2022) - talk
- Desy Users' meeting 2022 "Setup to study electronic structure of iron compounds in situ at conditions of the Earth's mantle" (01/2022) - poster
- EGU 2022 "X-ray emission scanning imaging setup to study electronic structure of iron-bearing compounds in situ at conditions of the Earth's mantle" (04/2022) - talk
- CarboPaT - Wehrheim "Electronic structure and formation of carbonates at condition sof the Earth'slowermantle: Project 3" (10/2018) - talk
- CarboPaT - Kall(Köln) "Formation and electronic structure of tetracarbonates Project 3: status update" (03/2019)- talk
- CarboPaT - Wehrheim "Formation of tetracarbonates - first information on the electronic structure" (10/2019) - talk
- CarboPaT - Wehrheim "The electronic structure of iron-bearing carbonates with tetrahedral coordination under high p/T conditions" (07/2022) - talk

Acknowledgement

Diese Dissertation wäre nicht möglich gewesen ohne die großartige Unterstützung vieler Leute, bei denen ich mich nun ganz recht herzlich bedanken möchte.

Als erstes möchte ich Prof. Dr. Metin Tolan danken für die Möglichkeit meine Dissertation in seiner Arbeitsgruppe anfertigen zu dürfen und mir die Wahl gelassen zu haben mich für dieses Thema zu entscheiden, sowie Prof. Dr. Max Wilke für die Aufnahme in sein Projekt, die große Unterstützung bei Messzeiten, der Probenvorbereitung und die vielen Diskussionen.

Des Weiteren möchte ich mich bei der Deutsche Forschungsgemeinschaft für die Finanzierung des Projekts über die elektronische Struktur der sp^3-Karbonate im Rahmen der Forschungsgruppe FOR2125 (CarboPaT) unter der Fördernummer STE 1079/4-1 bedanken. Besonders auch für Finanzierung der zahlreichen CarboPaT-Meetings unter Leitung von Prof. Dr. Björn Winkler mit vielen fachlichen und nicht-so-fachlichen Gesprächen.

Ein ganz besonderer Dank geht an Dr. Christian Sternemann für die zahlreiche Unterstützung bei Messzeiten, dem Analysieren und Interpretieren der Daten sowie dem Korrekturlesen der Dissertation. Ich hätte mir keine bessere Betreuung wünschen können.

Ohne Proben kann man natürlich nichts messen. Daher danke ich Dr. Valerio Cerantola, Dr. Stella Chariton und Dr. Christian Plückthun für die Synthese und Bereitstellung der Proben.

Viele Messungen, die im Rahmen dieser Arbeit durchgeführt wurden, wären ohne Hilfe schlicht nicht möglich gewesen. Daher danke ich Dr. Christian Schmidt für die Unterstützung der Raman Messungen am GFZ und Dr. Lkhamsuren Bayarjargal für die Hilfe bei der Probenpräparation und der Laserheizung in Frankfurt. Außerdem geht ein großer Dank an Dr. Hlynur Gretarsson, Dr. Martin Sundermann, Conrad Hagemeister, Dr. Nico Giordano, Dr. Aleksandr Kalinko und Dr. Wolgang Caliebe für die Unterstützung während den Messzeiten und die generelle Pflege der Beamlines, sodass die Messzeiten (mehr oder weniger) reibungslos ablaufen konnten. Besonders hervorheben möchte ich an dieser Stelle Hlynur und Martin, die uns zu jeder Tages- und Nachtzeit mit Rat und Tat zur Seite standen. Des Weiteren möchte ich bei Prof. Dr. Björn Winkler für die Durchführung der DFT-Rechnungen bedanken.

Bedanken möchte ich mich auch für die Hilfe während der Messzeiten von Leuten der Arbeitsgruppe. Vielen Dank an Robin, Nicola und Johannes für die vielen, vielen Überstunden und die Gewissheit, dass das Experiment in eurer Verantwortung in guten Händen ist und ich beruhigt ein paar Stunden schlafen konnte. Nicht zu vergessen ist dabei der Beitrag den Dr. Georg Spiekermann und Dr. Lélia Libon geleistet haben durch ihre umfangreichen Bemühungen die Laserheizung immer weiter zu verbessern und mir somit nicht nur das Heizen in Potsdam aber auch die tollen Ergebnisse durch das Heizen an der Beamline ermöglichten. Georg hat mir darüber hinaus alles beigebracht was ich über Diamantstempelzellen weiß und dabei nie die Ruhe und seine positive Art verloren, auch wenn meine Laune nach vielen Fehlversuchen am Tiefpunkt war. Danke!

Egal wie schlecht meine Laune auch war, zurück in Dortmund hat das Chaosbüro (wie Mirko es so liebevoll taufte) es immer wieder geschafft mir ein Lächeln aufs Gesicht zu zaubern. Vielen Dank für die gute Stimmung und eure durchgeknallte Art an Susanne, Göran und Fatima. Als das Chaosbüro langsam durch das Homeoffice abgelöst wurde, sind an diese Stelle dann Susanne, Jenny und Nicola getreten und haben in täglichen online Kaffeerunden die Einsamkeit verschwinden lassen. Danke!

Außerdem danke ich dem gesamten Lehrstuhl E1a für die stets positive Stimmung und den guten Zsammenhalt in allerlei Situationen.

Ich möchte mich auch ganz herzlich bei meinem Physiklehrer Markus Schröder dafür bedanken, dass er mich ermutigt hat das Physikstudium zu beginnen und ich ihm schon vor über 11 Jahren versprechen musste ihm diese Dissertation zu schicken sobald sie fertig ist.

Ein großer Dank geht an meine Mutter Inge, die stets alles in ihrer Macht Stehende getan hat, um mich zu unterstützen und mir viel Selbstvertrauen gab meinen eigenen Weg zu bestreiten.

Zu guter Letzt möchte ich mich von ganzem Herzen bei meiner Freundin und baldigen Ehefrau Nicola bedanken für das unzählige Beruhigen, Bestärken und einfach da sein wenn ich dachte ich schaffe das Alles nicht. Vielen Dank!